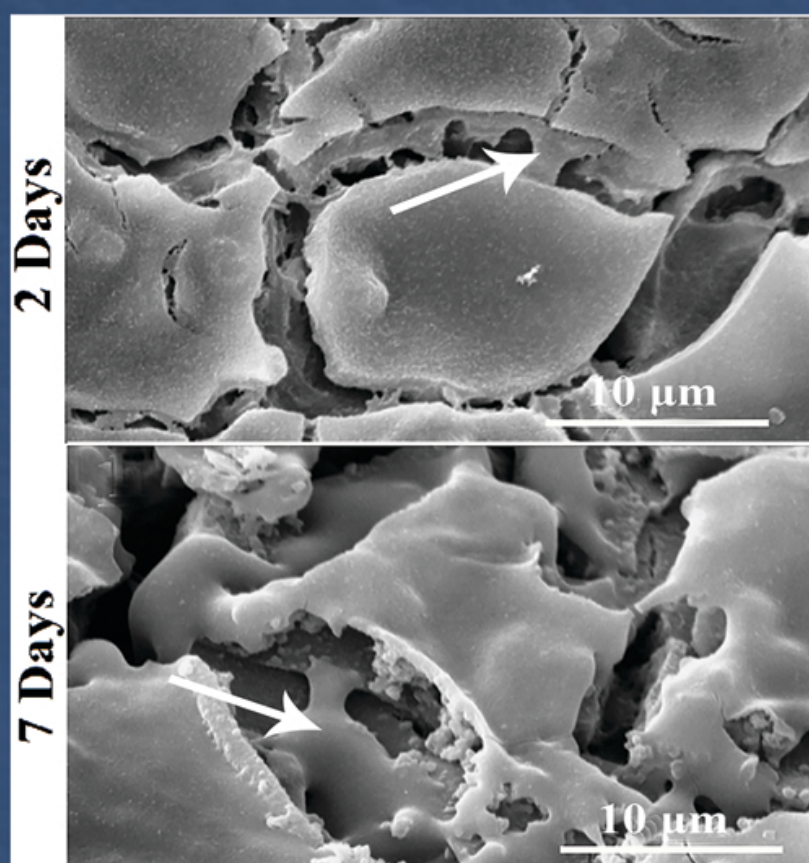


Advanced Ceramics Progress



Materials and Energy
Research Center



Iranian Ceramic Society

In The name of God

Advanced Ceramics Progress

DIRECTOR-IN-CHARGE

A. R. Khavandi

EDITOR-IN-CHIEF

M. R. Rahimipour

EXECUTIVE MANAGER

M. Razavi

EDITORIAL BOARD

- | | | | |
|-------|---|-------|--|
| A. R. | Aghaei, Materials and Energy Research Center | M. M. | Mohebi, Imam Khomeini University |
| P. | Alizadeh, Tarbiat Modares University | M. R. | Rahimipour, Materials and Energy Research Center |
| T. | Ebadzadeh, Materials and Energy Research Center | M. | Razavi, Materials and Energy Research Center |
| M. A. | Faghihi Sani, Sharif University of Technology | E. | Salahi, Materials and Energy Research Center |
| M. | Ghassemi Kakroudi, University of Tabriz | M. | Salehi, Isfahan University of Technology |
| A. R. | Khavandi, Iran University of Science and Technology | Ş. | Ţălu, Technical University of Cluj-Napoca |

EDITORIAL ADVISORY BOARD

F.S. Torknik

ENGLISH LANGUAGE EDITOR

M. Sabzevari

TECHNICAL STAFF

E. Pouladi, V. Hajabdolali, R. Chaluei

DISCLAIMER

The publication of articles in *Advanced Ceramics Progress* does not imply that the editorial board, editorial advisory board, reviewers or the publisher accept, approve or endorse the data and conclusions of authors.

Advanced Ceramics Progress (ISSN 2423-7477) (e-ISSN 2423-7485)

Web Site: www.acerp.ir, E-mail: office@acerp.ir

Tel: +98 (0) 26 36280040-7 ext.: 382, Fax: +98 (0) 26 36201888

Tel:+98 (0)21 88771626-7 ext.: 8931, Fax: +98 (0)21 88773352

Materials and Energy Research Center (MERC); Iranian Ceramic Society (ICERS)

CONTENTS

S. Ahmadi	Alkali-Activated Slag Cement and Concrete: A Review	1-9
S. Borhan M. R. Badr-Mohammadi S. Hesaraki J. Esmailzadeh	Fabrication and Preliminary Characterization of Tissue Engineering Scaffolds Based on Alumina/Bioactive Glass	10-19
V. Dalouji S. Goudarzi N. Rahimi A. R. Souri	Multi-Walled Carbon Nanotubes (MWCNTs) Synthesized on Ni-Cu NPs @ a-C: H Films: A Study of Cavity and Bearing Areas Percentage, ZX Topography, and the Width of the Surface Height Distribution with Different Ni Layers' Thickness	20-27
M. R. Akbarpour Arbatan F. S. Torknik	Modelling and Optimization of Densification and Hardness of Cu/SiC Nanocomposites based on Response Surface Methodology (RSM)	28-35
N. Nayeypashae E. Etemadi B. Mohammad Sadeghi S. H. Seyedin	Experimental and Numerical Study of the Thermo-Mechanical Behavior of Plasma-Sprayed Gadolinium and Yttria Zirconate-Based Thermal Barrier Coatings	36-51
F. S. Sayyedani M. H. Enayati M. R. Rahimpour	Microstructure and Mechanical Properties of Spark Plasma Sintered Amorphous AlPO ₄ Ceramics	52-58



Materials and Energy Research Center
MERC

Contents lists available at [ACERP](http://www.acerp.ir)

Advanced Ceramics Progress

Journal Homepage: www.acerp.ir



Review Article

Alkali-Activated Slag Cement and Concrete: A Review

S. Ahmadi *

^a Assistant Professor, Construction and Minerals Research Group, Technology and Engineering Research Center, Standard Research Institute, Karaj, Alborz, Iran

* Corresponding Author Email: s.ahmadi@standard.ac.ir (S. Ahmadi)

URL: https://www.acerp.ir/article_143604.html

ARTICLE INFO

Article History:

Received 21 November 2021
Received in revised form 05 January 2022
Accepted 22 January 2022

Keywords:

Alkali activated Slag
Alkaline Concrete
Ground Granulated Blast Furnace Slag
Mechanical Properties
Chemical Properties

ABSTRACT

Recently, Alkali-Activated Concrete (AAC) as an appropriate alternative to Portland Cement Concrete (PCC) has drawn considerable attention owing to its acceptable properties and less environmental impacts. The current study presents a review of previous researches on Alkali-Activated Slag Cement Concrete (AASCC). The following issues are also covered in this study: an introduction to AASCC and its constituents, environmental impacts, hydration reaction, hydration products, mechanical properties, high temperature resistance, attack resistance of acids and sulfates, water absorption, shrinkage, and its challenges in application. The results from different studies revealed a research gap to be filled. To be specific, several different parameters affect AASCC properties; however, given that its properties are still partially unexplored, more researches are needed to find out its best engineering properties.



<https://doi.org/10.30501/ACP.2022.316176.1076>

1. INTRODUCTION

Nowadays, Portland Cement (PC) is one of the most extensively used materials in construction. The usual consumption rate of PC is approximately one ton per person a year [1], and the demands for it are still increasing every year. Currently, the amount of PC production is more than three billion tons per year which, as predicted, may reach six billion tons in the next 40 years [2]. Figure 1 shows the increasing trend of PC production until 2014 [3].

PC production has some environmental impacts such as greenhouse gas emissions and air pollution. In addition, this industry is highly energy-consuming. In

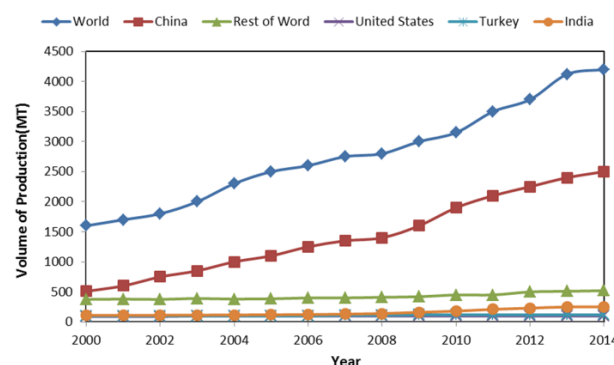


Figure 1. PC production per year for countries [3]

Please cite this article as: Ahmadi, S., "Alkali-Activated Slag Cement and Concrete: A Review", *Advanced Ceramics Progress*, Vol. 7, No. 4, (2021), 1-9. <https://doi.org/10.30501/ACP.2022.316176.1076>

2423-7485/© 2021 The Author(s). Published by MERC.

This is an open access article under the CC BY license (<https://creativecommons.org/licenses/by/4.0/>).



this regard, given the increasing demand for PC, it is recommended that PC be substituted with another type of cement, especially Alkali-Activated Slag Cement (AASC) owing to its superior properties [4].

Although AASCC has been frequently explored in many studies in recent years, it is an old technology. In 1908, Kühl confirmed the stabilization of the blast furnace slag powder with sodium hydroxide. In 1940, Pordon published more extensive researches on alkali-activated clinker-free cement. Two decades later, Glukhovskiy investigated the alkaline activation of different organic and inorganic aluminosilicates [5-7]. Industrial production of AASC first began in Ukraine in 1960-1964. It was obtained through activating the slag, a by-product in the production of iron, using alkaline materials. In this process, aluminosilicate monomers dissolve in the slag structure and produce a cementitious and adhesive composition. Use of this type of cement is economically affordable. In addition, compared to PC, it is characterized by more acceptable properties [8].

2. THE ENVIRONMENTAL IMPRESSION AASC

CO₂ emission from the PC industry is an important environmental issue to be concerned about. As shown in Figure 2, about 3 % of the world's greenhouse gases are generated by cement industries.

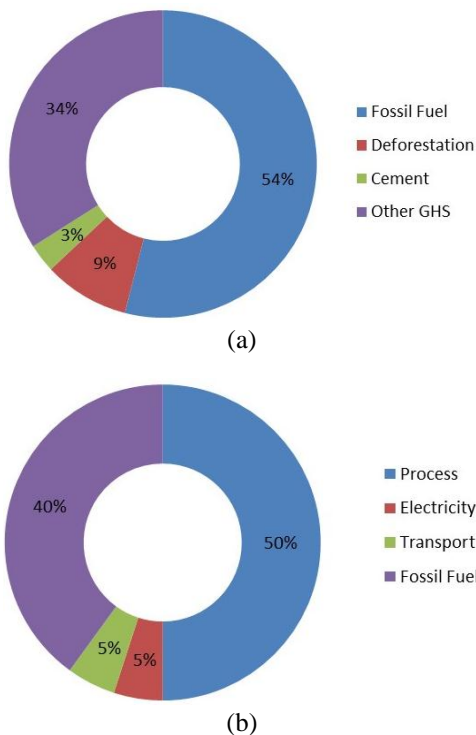


Figure 2. (a) Different sources of CO₂ gas emissions and (b) Contribution of pollutions of different parts of the cement production process

According to the reports, the cement industry alone can generate 7 % of CO₂ in the world [9]. The fabrication of one ton of PC releases approximately 0.7 to 1 ton of CO₂ gas into the atmosphere [10,11]. Between 1930 and 2013, cumulatively, cement industries contributed to about 43 % of CO₂ emissions [12].

The main advantage of AASC, compared to PC, is its notable effect on reducing the environmental pollutants. To be specific, the CO₂ emission in the AASC production is 50-80 % lower than that in the PC production [13,14], hence it can be regarded as an operative technology that can considerably reduce the CO₂ emissions. The key material in the AASC production is slag, which is actually a by-product of pig iron; therefore, the production of this type of cement also reduces the waste materials. According to the reports, the global warming potential in AASC production is 70 % lower than that in PC production [15].

3. INGREDIENTS OF AASC

3.1. Slag

In the production process of pig iron in the blast furnace, limestone reacts with Al₂O₃ and SiO₂ rich components in iron ore and coke and produces molten slag. If the molten slag cools rapidly below 800 °C, it becomes a suitable glass material to be used in the cement industry. Powdered slag is a material characterized by hydraulic properties only in the presence of an appropriate alkaline activator. AAS cement is a delayed hydraulic material. However, other hydraulic materials have this property when mixed with water [16]. Blast furnace slag with a C/S ratio between 0.2 to 2 and A/S ratio between 0.1 to 0.6 are commonly used in AASC production. A, S, and C are abbreviations of Al₂O₃, SiO₂, and CaO, respectively.

3.2. Alkaline Activators

Once the slag powder is mixed with water, the hydrated thin layers containing Ca⁺² and SiO₂ are formed on the external surface of the particles. At this point, the amount of pH reaches 10. This hydrated film on the surface of slag particles interrupts the hydration reaction; therefore, a suitable activator should be added to the mixture to have a continuous reaction. Alkaline activators increase the pH value of the liquid phase and prevent the formation of a protecting layer on the slag surface, thus preserving the solubility of the slag glassy phase. Alkaline activators break the bonds in the slag glass phase structure and increase the dissolution rate of the ionic components [17].

Sodium silicate in either powder or liquid forms, sodium hydroxide, and sodium carbonate are usually used as the activator. Sodium sulfate, potassium hydroxide, gypsum, sodium aluminate, and hydrated lime are also used in different studies. Activators are

added in small amounts of about 2-10 wt. % of the slag. Since the slag compositions differ depending on the raw materials and production process, the most appropriate activator should be selected. The type and amount of activators are both essential factors that affect the properties of AASC. For example, the results revealed that the pastes prepared by Na_2SiO_3 activator had shorter setting time than Na_2CO_3 and NaOH activators [18-22].

3.3. Chemical Admixtures

There are several types of superplasticizers including lignosulfonates, naphthalene, vinyl copolymer, melamine, and polycarboxylate derivatives. The chemical admixtures are absorbed into the cement particles. As a result, they create an electrostatic repulsion among the particles, thus preventing their agglomeration [23].

Shrinkage-reducing chemical admixtures such as polypropylene glycol derivatives reduce the surface tension of water in concrete pores. Consequently, the capillary tension in the pore structure and shrinkage decreases during the drying process. Chemical admixtures such as malic acid and sodium chloride are also used as retardants. The amount of admixtures in different types of cements is less than 5 wt. % [23,24].

4. MIMING PROTOCOL OF AASC

Several different mixing protocols were proposed in the literatures. Generally, slag is ground with gypsum. The amount of gypsum was reported to be 2-3 wt. % of the slag. The specific surface area of the slag was suggested to be between 250 and 700 m^2/kg . The water-to-binder ratio (W/b) in AASC is usually set between 0.3 and 0.5 [25]. Activators are either directly mixed with the slag or first dissolved in water and then mixed with it. The corrosive properties of the activators and high pH of the material should be considered in the mix of AASC. The slag-to-aggregate ratio is usually either 1:2 or 1:3 [19-25]. The admixtures are then directly added during mixing [23]. The common aggregates in PC concrete are used to produce AASCC. It should be noted that AASC is generally formed by casting.

5. HYDRATION REACTION MECHANISM AND PRODUCTS

The slag composition, activator type, and pH are the main parameters that control the hydration products of AASC.

Wang et al. [26] reported that the main hydration product was C-S-H with low C/S ratio and different crystallinity. In addition, the XRD analysis conducted by Puertas et al. confirmed the existence of hydrotalcite ($\text{Mg}_6\text{Al}_2\text{CO}_3(\text{OH})_{16}\cdot 4\text{H}_2\text{O}$), calcite (CaCO_3), and CSH as

hydration products in the slag activated with NaOH [27].

Hydration of slag is a multipart process includes initial degradation of slag and densification of hydration products. The hydration of slag initiate by ion exchange of H^+ in water for Ca^{+2} or Na^+ . Al-O-Si bonds hydrolyze and then the depolymerized slag network breakdown. So Si and Al release as $\text{Al}(\text{OH})_4^-$ and $(\text{H}_3\text{SiO}_4)^-$ and $(\text{H}_2\text{SiO}_4)^{2-}$ ions in water and finally precipitate on the surface of slag particles with increasing the concentration of them [28].

Krizan et al. found that the hydration reaction rate was correlated to the modulus of Na_2O and silica (M_s) in sodium silicate-activated slag. In summary, hydration reaction initiates with the degradation of Ca-O, Mg-O, Si-O-Si, Al-O-Al, and Al-O-Si bands in the slag and then, a Si-Al layer precipitates on the surface layer of the slag particles [29].

An investigation by Wang et al. confirmed that during the hydration of AAS, dissolution and precipitation were the predominate mechanisms in the initial stage of the reaction that continued with the solid-state mechanism. [26]. Mozgawa et al. concluded that Si^{+4} of the sorosilicate $[\text{Si}_2\text{O}_7]^{-6}$ units in the glassy phase were partially substituted by Al^{+3} during the AAS hydration. The ^{29}Si MAS-NMR spectra confirms this claim. According to the ^{27}Al MAS-NMR spectra, Al atoms can occupy tetrahedral and octahedral coordination in the hydration process determined by the activator type and factors of hydration process [30].

6. THE HEAT OF HYDRATION

The hydration heat in the AAS is usually about three times lower than that in the OPC [8,31], depending on type and dosage of the used activator. For example, Krizan et al. observed that the hydration heat of the AAS increased upon increasing the dose and modulus of sodium silicate [29]. It was also reported that using Lime and gypsum as the activator would increase the hydration heat more than that in the slag activated with lime only, mainly due to the formation of ettringite phase and its transformation to monosulfoaluminate phase. However, the hydration heat of OPC was higher than that of AAS [32]. As mentioned earlier, AASC hydration products have a lower Ca/Si ratio, hence they need less hydration energy than OPC [33].

7. PROPERTIES OF AASCC

7.1. Mechanical Properties of AASCC

The compressive strength of AASCC is its most significant mechanical property. Several parameters including the composition and specific surface area of the slag, type and amount of alkaline activator, water-to-slag ratio, and curing conditions of the concrete affect the

mechanical strength of AASC [34-42].

AASCC is characterized by high initial strength. The initial compressive strength of this concrete is 60 MPa, and its one-year strength can reach more than 100 MPa. The higher rate of hydration reactions at higher pHs, which is the cause of high strength in the first days of concrete preparation, and homogenous and dense interface between the paste and aggregate are the two vital factors that contribute to the high mechanical strength of AASCC [34].

AAS concrete is susceptible to curing conditions. Bakharev et al. [37] reported that the initial strength of the Room-Temperature (RT) cured samples are less than those cured at higher temperatures. However, the later strength of the RT cured samples is clearly higher than that of the others (Figure 3) resulting from the inhomogeneity of the matrix microstructure due to the higher hydration reaction rate than the diffusion rate at higher-temperature curing. In other words, the hydration products precipitated around the slag particles, make barriers to diffusion, and form an inhomogeneous microstructure [37].

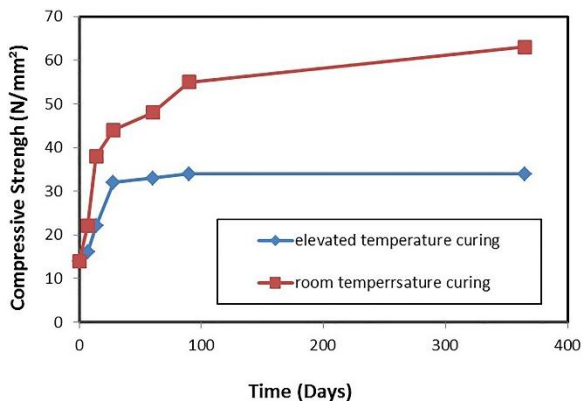


Figure 3. Compressive strength of AASC versus curing temperature. Lines are shown as guides for the eyes

Collins et al. [40] found that the compressive strength of AASC samples in a water bath increased up to 400 days, while the maximum strength of the sealed specimens was obtained in 91 days. In addition, the samples exposed to air were more susceptible to a decrease in their strength over time mainly due to the presence of microcracks in the matrix. Figure 4 shows the compressive strength changes in different curing conditions.

According to the literature, the effect of alkali activator on the strength of AASC has not been systematically investigated yet. Chi showed that the amount of Na_2O in the activator could affect the strength of AASC. In addition, the liquid sodium silicate was characterized by a higher initial strength than that of its powder counterpart [35,40].

In another research, replacing 20 % slag with the

recycled concrete fines improved the compressive strength of AAS concrete blocks up to about 13 % [43].

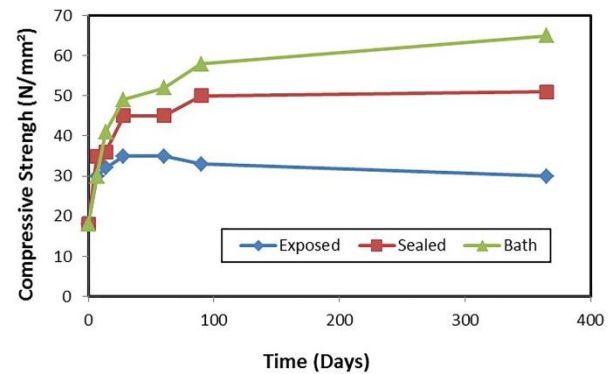


Figure 4. Compressive strength of AASC versus curing condition. Lines are shown as guides for the eyes

7.2. High-Temperature Resistance of AAC

Several physical and chemical mechanisms can decrease the strength of PC cement at high temperatures [44].

Variances in the coefficient of the thermal expansion between the aggregate and mortar cause an internal stress in the concrete and micro cracks. In addition, decomposition of calcium hydroxide ($\text{Ca}(\text{OH})_2$) in PC at temperatures above $400\text{ }^\circ\text{C}$ would decrease its strength. Moreover, scaling of OPCC at higher temperatures plays a key role in strength deterioration [45,46].

A number of studies have evaluated the performance of AASC at high temperature, considering the significance of this parameter in the concrete. The compressive strength of alkali-activated slag mortar at temperatures above $400\text{ }^\circ\text{C}$ is the same of that of PC mortar. In this case, dehydration of C-S-H gel is the main reason for strength reduction [47]. Approximately, 65-85 % loss in the strength of AAS mortars was reported at temperatures above $800\text{ }^\circ\text{C}$ [47-49].

Guerrieri et al. [50] observed that the decrease in the strength resulted from the differences in the thermal expansion coefficient of the aggregate and slag at high temperatures.

7.3. Chemical Properties of AASCC

7.3.1. Water Absorption and Chloride Diffusion

The permeability of concrete is assessed by water absorption which is lower in AASC than in PC thanks to the dense microstructure of AASC. Water absorption is directly associated to the chloride diffusion [51]. According to the findings, using porous recycled aggregates instead of natural aggregates in concrete would cause higher water absorption and chloride diffusion. Water absorption in AASCC also increases upon increasing the specific surface area of the recycled aggregates [52,53].

7.3.2. Sulphate and Acid Attack

Cement resistance against the sulfate and acid attacks is one of the significant aspects in the durability of different types of concrete that should be taken into consideration. Both properties of the pores and type of acid corrosion products affect the resistance of a concrete against acid corrosion.

As reported, AASCC exhibited higher resistance to sulphate attack than PC concrete after one-year exposure to 10 % sodium sulphate. Nevertheless, the strength decreased when the samples were exposed to 10 % magnesium sulfate in the same time period [51].

Numerous researches have been conducted on the resistance of AASC in acid environments. For instance, Mithum et al. [51] observed a considerable decrease in the mass of AASCC after 120 days of exposure to H_2SO_4 solution, which was attributed to a decrease in the concrete strength mainly due to the slag dissolution which created more paths for the acid to move along the AASC, hence further dissolution [53].

C. Shi et al. [54] also observed that the PC corrosion in acetic acid solution with pH = 5 after one year was much more than the AASC corrosion due to its more porous structure of the corrode layer. They concluded that acid resistance depended on hydration products and protective layer.

7.3.3. Carbon Diffusion

Carbonation of AAS concrete in CO_2 atmosphere or solution starts from its surface and gradually diffuses into the concrete. The carbonation rate is determined by the rate at which HCO_3^- and CO_2 diffuse into the concrete. This process follows Fick's law. In other words, the carbonation rate (increasing the depth of carbon with time) is proportional to the square root of time.

When the concrete is exposed to CO_2 , the C-S-H phase reacts to produce $CaCO_3$ and calcium-free C-S-H and aluminosilicate gel. Given that the amount of Ca in AASC is low, there are not enough $CaCO_3$ precipitations. In addition, the porosity of the substrate increases owing to the carbonate reaction. The entry of HCO_3^- and CO_2 into the interior increases and as a result, the reaction proceeds faster. Therefore, AASC is more susceptible to carbon diffusion than the ordinary PC [55].

7.4. Shrinkage of AASCC

Generally, AASCC is characterized by finer pores than OPCC, hence higher shrinkage of AASCC. According to the study conducted by Collins and Sanjayan [56], more meso pores in AASCC microstructure and higher capillary stress can cause higher shrinkage in alkali-activated cement pastes. Another research [32,57] confirmed this theory. However, the different composition of the reaction product (C-S-A-H and C-S-H) was the other cause of further shrinkage of AASCC [29].

Numerous studies have focused on reducing shrinkage

in the AASC. To this end, they employed several methods such as application of suitable admixtures [58], fibers [59,60], heat treatment [37], expanding admixture [61], and low-temperature preparation technology [62]. In general, the type and quantity of the activator, surface area of the slag, and curing condition are the factors affecting the shrinkage of AASC. T. Bakharev et al. [35] found that the highest shrinkage belonged to the sodium-silicate-activated sample.

According to the findings, the slag activated with NaOH and sodium silicate exhibited three to six times more shrinkage than that of PC [57]. Figure 5 illustrates the effect of different activators on the AASC drying shrinkage. As observed, the shrinkage attributed to sodium carbonate was less than/ similar to that of OPC mortar. Ye and Radlińska [63] made a comparison of the obtained results.

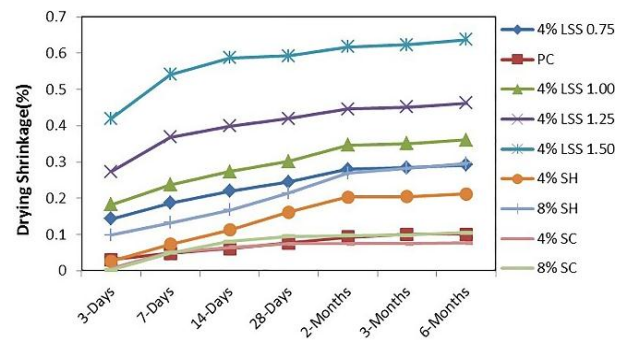


Figure 5. Effect of different activators on drying shrinkage of the slag

According to Figure 5, using 9 % Na_2SiO_3 and 10 % OPC simultaneously yields the desired shrinkage with OPC [64]. The slag activated with lime and gypsum exhibited lower shrinkage than that activated with lime only [32]. This dissimilarity is due to the difference in volume of smaller pore and nature of hydration products in the concrete.

8. CHALLENGES IN AASCC

Regardless of numerous advantages of AASC, its application is still quite challenging.

- **Slag Composition:**
The slag compositions differ depending on the raw materials and melting procedure. The variation in the slag compositions causes a different behavior of activation. In fact, one condition cannot be generalized to all slags. Therefore, it is suggested that a small-scale test be done for each slag to obtain the best activation mode.
- **Chemical Activators:**
The activators that are currently used for AASCC production are viscous, expensive, and corrosives.

In order to increase the application of this cement, safe and environmentally-friendly green activators characterized by the same mechanical properties of the chemical activators should be used. More researches on the efficiency of different green activators are also available.

- **Admixtures:**
To the best of the author's knowledge about PC, most of the admixtures are used in AASCC production. Given that AASC has different chemical and behavioral characteristics, development of admixtures that are specifically suitable for alkali activated slag gains significance. Therefore, the contradictory results observed in AASC will diminish, thus making it a good candidate to compete with PC.
- **Low workability and setting time:**
This restriction of alkali-activated cement depends on the type of activator. In fact, obtaining the desirable mechanical properties and suitable workability is made feasible only by using an appropriate activator.
- **High Shrinkage:**
Different studies proposed numerous methods to reduce the shrinkage of AASC. However, all of these methods reduce the shrinkage to some extent, and some of these methods affected other properties of the AASC that was uncalled for.
- **Lack of standard:**
There are a few standards related to AASC. However, the PC-related standards are currently used for AASC as well. This restriction prevents stockholders from accepting the AASC. Therefore, there is a need for developing appropriate rules and standards to improve the emerging market of AASC products.
- **Large-Scale Applications:**
Large-scale PC has been used for many years. However, not many applications have been reported for AASC. As a result, consumers doubt whether it is still the best option.

Although slag has been widely used in the preparation of alkali-activated concrete, its production becomes more difficult more than ever. Apparently, using slag in combination with other recycled materials can be promising. There are appreciated researches in this field. For Example, recycled concrete/brick powder may be a high value-added alternative [65-67].

9. APPLICATION OF AASC

In recent years, thorough information on the chemistry, slag and alkali activator reaction products, mechanical properties, and durability of AAS cement has been obtained. However, its application as a product has not been fully investigated yet. The quick setting of this type

of cement makes it a good candidate as a repair material with excellent durability. The excellent resistance of this cement against the diffusion of chlorides and freezing encourages its applications in cold climates and salty environments. Owing to its numerous advantages, AASC have wide applications in manufacturing products such as prefabricated cement blocks with different sizes, corrosion and heat resistant concretes, and mortars. In addition, this cement is innovatively used in the immobilization of radioactive waste and heavy metals [68-70].

10. CONCLUSION

The present study made an attempt to present a comprehensible overview of AASC. Compared to PC, AASC enjoys several advantages such as higher mechanical strength, lower hydration heat, higher resistance to chemical attacks, and carbon diffusion. However, it also has some drawbacks namely rapid setting and lower workability, higher shrinkage, and consequent cracking. According to the findings, different factors could affect the properties of AASC among which, water-to-slag ratio, mixing protocol, curing conditions (temperature and humidity), dosage and type of activator, different admixture, and slag composition are the most important ones that should be optimized according to the desired properties.

ACKNOWLEDGEMENTS

The author would like to express gratitude to the Standard Research institute for the support in the development of this study under project No.1404.

REFERENCES

1. Gholizadeh-Vayghan, A., Nofallah, M. H., Khaloo, A., "Technoeconomic Study of Alkali-Activated Slag Concrete with a Focus on Strength, CO₂ Emission, and Material Cost", *Journal of Materials in Civil Engineering*, Vol. 33, No. 7, (2021), 04021136. [https://doi.org/10.1061/\(ASCE\)MT.1943-5533.0003763](https://doi.org/10.1061/(ASCE)MT.1943-5533.0003763)
2. Nanayakkara, O., Gunasekara, C., Sandanayake, M., Law, D. W., Nguyen, K., Xia, J., Setunge, S., "Alkali activated slag concrete incorporating recycled aggregate concrete: Long term performance and sustainability aspect", *Construction and Building Materials*, Vol. 271, (2021), 121512. <https://doi.org/10.1016/j.conbuildmat.2020.121512>
3. Nidheesh, P. V., Kumar, M. S., "An overview of environmental sustainability in cement and steel production", *Journal of Cleaner Production*, Vol. 231, (2019), 856-871. <https://doi.org/10.1016/j.jclepro.2019.05.251>
4. Amer, I., Kohail, M., El-Feky, M. S., Rashad, A., Khalaf, M. A., "Evaluation of using cement In alkali-activated slag concrete", *International Journal of Scientific and Technology Research*, Vol. 9, No. 05, (2020), 245-248. <http://www.ijstr.org/final->

- print/may2020/Evaluation-Of-Using-Cement-In-Alkali-activated-Slag-Concrete.pdf
5. Perumal, P., Sreenivasan, H., Luukkonen, T., Kantola, A. M., Telkki, V. V., Kinnunen, P., Illikainen, M., "High strength one-part alkali-activated slag blends designed by particle packing optimization", *Construction and Building Materials*, Vol. 299, (2021), 124004. <https://doi.org/10.1016/j.conbuildmat.2021.124004>
 6. Thomas, R. J., Ye, H., Radlińska, A., Peethamparan, S., "Alkali-activated slag cement concrete: A closer look at a sustainable alternative to portland cement", *Concrete International*, Vol. 38, No. 1, (2016), 33-38. <https://www.researchgate.net/publication/291971035>
 7. Obonyo, E., Kamseu, E., Melo, U. C., Leonelli, C., "Advancing the use of secondary inputs in geopolymer binders for sustainable cementitious composites: A review", *Sustainability*, Vol. 3, No. 2, (2011), 410-423. <https://doi.org/10.3390/su3020410>
 8. Puertas, F., González-Fontebao, B., González-Taboada, I., Alonso, M. M., Torres-Carrasco, M., Rojo, G., Martínez-Abella, F., "Alkali-activated slag concrete: Fresh and hardened behavior", *Cement and Concrete Composites*, Vol. 85, (2018), 22-31. <https://doi.org/10.1016/j.cemconcomp.2017.10.003>
 9. Pal, A., "Developing low-clinker ternary blends for indian cement industry", *Journal of The Institution of Engineers (India): Series A*, Vol. 99, No. 3, (2018), 433-447. <https://doi.org/10.1007/s40030-018-0309-4>
 10. Josa, A., Aguado, A., Heino, A., Byars, E., Cardim, A., "Comparative analysis of available life cycle inventories of cement in the EU", *Cement and Concrete. Reserch*, Vol. 34, No. 8, (2004), 1313-1320. <https://doi.org/10.1016/j.cemconres.2003.12.020>
 11. Gartner, E., "Industrially interesting approaches to "low-CO₂" cements", *Cement and Concrete. Reserch*, Vol. 34, No. 9, (2004), 1489-1498. <https://doi.org/10.1016/j.cemconres.2004.01.021>
 12. Xi, F., Davis, S. J., Ciais, P., Crawford-Brown, D., Guan, D., Pade, C., Shi, T., Syddall, M., Lv, J., Ji, L., Bing, L., Wang, J., Wei, W., Yang, K. H., Lagerblad, B., Galan, I., Andrade, C., Zhang, Y., Liu, Z., "Substantial global carbon uptake by cement carbonation", *Nature Geoscience*, Vol. 9, (2016), 880-883. <https://doi.org/10.1038/ngeo2840>
 13. Duxson, P., Provis, J. L., Lukey, G. C., van Deventer, J. S. J., "The role of inorganic polymer technology in the development of 'green concrete'", *Cement and Concrete Research*, Vol. 37, No. 12, (2007), 1590-1597. <https://doi.org/10.1016/j.cemconres.2007.08.018>
 14. Provis, J. L., van Deventer, J. S. J., Eds., *Geopolymers: Structures, Processing, Properties and Industrial Applications*, Woodhead Publishing Limited, UK, (2009). https://toaz.info/docdownloadv2-geopolymers-structures-processing-properties-and-industrial-applications-pr_9d11a4e3fa8db9c2664fed3681ae9c3a
 15. Weil, M., Dombrowski, K., Buchwald, A., "10 - Life-cycle analysis of geopolymers", In *Geopolymers*, Woodhead Publishing, (2009), 194-210. <https://doi.org/10.1533/9781845696382.2.194>
 16. Mostafa, N. Y., El-Hemaly, S. A. S., Al-Wakeel, E. I., El-Korashy, S. A., Brown, P. W., "Characterization and evaluation of the hydraulic activity of water-cooled slag and air-cooled slag", *Cement and Concrete Research*, Vol. 31, No. 6, (2001), 899-904. [https://doi.org/10.1016/S0008-8846\(01\)00497-5](https://doi.org/10.1016/S0008-8846(01)00497-5)
 17. Odler, I., *Special Inorganic Cements*, CRC Press, London, (2003). <https://doi.org/10.1201/9781482271942>
 18. Brough, A. R., Atkinson, A., "Sodium silicate-based, alkali-activated slag mortars: Part I. Strength, hydration and microstructure", *Cement and Concrete Research*, Vol. 32, No. 6, (2002), 865-879. [https://doi.org/10.1016/S0008-8846\(02\)00717-2](https://doi.org/10.1016/S0008-8846(02)00717-2)
 19. Deir, E., Gebregziabihier, B. S., Peethamparan, S., "Influence of starting material on the early age hydration kinetics, microstructure and composition of binding gel in alkali activated binder systems", *Cement and Concrete Composites*, Vol. 48, (2014), 108-117. <https://doi.org/10.1016/j.cemconcomp.2013.11.010>
 20. Gebregziabihier, B. S., Thomas, R., Peethamparan, S., "Very early-age reaction kinetics and microstructural development in alkali-activated slag", *Cement and Concrete Composites*, Vol. 55, (2015), 91-102. <https://doi.org/10.1016/j.cemconcomp.2014.09.001>
 21. Thomas, R. J., Peethamparan, S., "Alkali-activated concrete: Engineering properties and stress-strain behavior", *Construction and Building Materials*, Vol. 93, (2015), 49-56. <https://doi.org/10.1016/j.conbuildmat.2015.04.039>
 22. Atiş, C. D., Bilim, C., Çelik, Ö., Karahan, O., "Influence of activator on the strength and drying shrinkage of alkali-activated slag mortar", *Construction and Building Materials*, Vol. 23, No. 1, (2009), 548-555. <https://doi.org/10.1016/j.conbuildmat.2007.10.011>
 23. Palacios, M., Puertas, F., "Effect of superplasticizer and shrinkage reducing admixture on alkali activated slag pastes and mortars", *Cement and Concrete Research*, Vol. 35, No. 7, (2005), 1358-1367. <https://doi.org/10.1016/j.cemconres.2004.10.014>
 24. Brough, A. R., Holloway, M., Sykes, J., Atkinson, A., "Sodium silicate-based alkali activated slag mortars: Part II. The retarding effect of additions of sodium chloride or malic acid", *Cement and Concrete Research*, Vol. 30, No. 9, (2000), 1375-1379. [https://doi.org/10.1016/S0008-8846\(00\)00356-2](https://doi.org/10.1016/S0008-8846(00)00356-2)
 25. Collins, F., Sanjayan, J. G., "Strength and shrinkage properties of alkali activated slag concrete containing porous coarse aggregate", *Cement and Concrete Research*, Vol. 29, No. 4, (1999), 607-610. [https://doi.org/10.1016/S0008-8846\(98\)00203-8](https://doi.org/10.1016/S0008-8846(98)00203-8)
 26. Wang, S. D., Scrivener, K. L., "Hydration products of alkali activated slag cement", *Cement and Concrete Research*, Vol. 25, No. 3, (1995), 561-571. [https://doi.org/10.1016/0008-8846\(95\)00045-E](https://doi.org/10.1016/0008-8846(95)00045-E)
 27. Puertas, F., Fernández-Jiménez, A., Blanco-Varela, M. T., "Pore solution in alkali-activated slag cement pastes. Relation to the composition and structure of calcium silicate hydrate", *Cement and Concrete Research*, Vol. 34, No. 1, (2004), 139-148. [https://doi.org/10.1016/S0008-8846\(03\)00254-0](https://doi.org/10.1016/S0008-8846(03)00254-0)
 28. Duxson, P., Provis, J. L., "Designing precursors for geopolymer cements", *Journal of American Ceramic Society*, Vol. 91, No. 12, (2008), 3864-3869. <https://doi.org/10.1111/j.1551-2916.2008.02787.x>
 29. Krizan, D., Zivanovic, B., "Effects of Dosage and Modulus of Water Glass on Early Hydration of Alkali-Slag Cements", *Cement and Concrete Research*, Vol. 32, No. 8, (2002), 1181-1188. [https://doi.org/10.1016/S0008-8846\(01\)00717-7](https://doi.org/10.1016/S0008-8846(01)00717-7)
 30. Mozgawa, W., Deja, J., "Spectroscopic studies of alkaline activated slag geopolymers", *Journal of Molecular Structure*, Vol. 924-926, (2009), 434-441. <https://doi.org/10.1016/j.molstruc.2008.12.026>
 31. Xuequan, W., Sheng, Y., Xiaodong, S., Mingshu, T., Liji, Y., "Alkali-activated slag cement based radioactive waste forms", *Cement and Concrete Research*, Vol. 21, No. 1, (1991), 16-20. [https://doi.org/10.1016/0008-8846\(91\)90026-E](https://doi.org/10.1016/0008-8846(91)90026-E)
 32. Neto, A. A. M., Cincotto, M. A., Repette, W., "Drying and autogenous shrinkage of pastes and mortars with activated slag cement", *Cement and Concrete Research*, Vol. 38, No. 4, (2008), 565-574. <https://doi.org/10.1016/j.cemconres.2007.11.002>
 33. Bai, Y., Collier, N. C., Milestone, N. B., Yang, C. H., "The potential for using slags activated with near neutral salts as immobilisation matrices for nuclear wastes containing reactive metals", *Journal of Nuclear Materials*, Vol. 413, No. 3, (2011), 183-192. <https://doi.org/10.1016/j.jnucmat.2011.04.011>
 34. Bernal, S. A., de Gutiérrez, R. M., Pedraza, A. L., Provis, J. L., Rodríguez, E. D., Delvasto, S., "Effect of binder content on the performance of alkali-activated slag Concretes", *Cement and Concrete Research*, Vol. 41, No. 1, (2011), 1-8. <https://doi.org/10.1016/j.cemconres.2010.08.017>
 35. Bakharev, T., Sanjayan, J. G., Cheng, Y. B., "Effect of admixtures on properties of alkali-activated slag concrete", *Cement and*

- Concrete Research*, Vol. 30, No. 9, (2000), 1367-1374. [https://doi.org/10.1016/S0008-8846\(00\)00349-5](https://doi.org/10.1016/S0008-8846(00)00349-5)
36. Okoye, F. N., Durgaprasad, J., Singh, N. B., "Mechanical properties of alkali activated flyash/Kaolin based geopolymer concrete", *Construction and Building Materials*, Vol. 98, (2015), 685-691. <https://doi.org/10.1016/j.conbuildmat.2015.08.009>
 37. Bakharev, T., Sanjayan, J. G., & Cheng, Y. B., "Effect of elevated temperature curing on properties of alkali-activated slag concrete", *Cement and Concrete Research*, Vol. 29, No. 10, (1999), 1619-1625. [https://doi.org/10.1016/S0008-8846\(99\)00143-X](https://doi.org/10.1016/S0008-8846(99)00143-X)
 38. Chi, M., "Effects of dosage of alkali-activated solution and curing conditions on the properties and durability of alkali-activated slag concrete", *Construction and Building Materials*, No. 35, (2012), 240-245. <https://doi.org/10.1016/j.conbuildmat.2012.04.005>
 39. Rashad, A. M., "Properties of alkali-activated fly ash concrete blended with slag", *Iranian Journal of Materials Science and Engineering*, Vol. 10, No. 1, (2013), 57-64. <http://ijmse.iust.ac.ir/article-1-522-en.pdf>
 40. Collins, F., Sanjayan, J. G., "Microcracking and strength development of alkali activated slag concrete", *Cement and Concrete Composites*, Vol. 23, No. 4-5, (2001), 345-352. [https://doi.org/10.1016/S0958-9465\(01\)00003-8](https://doi.org/10.1016/S0958-9465(01)00003-8)
 41. Nath, P., Sarker, P. K., "Effect of GGBFS on setting, workability and early strength Properties of fly ash geopolymer concrete cured in ambient condition", *Construction and Building Materials*, Vol. 66, (2014), 163-171. <https://doi.org/10.1016/j.conbuildmat.2014.05.080>
 42. Bakharev, T., "Geopolymeric materials prepared using Class F fly ash and elevated temperature curing", *Cement and Concrete Research*, Vol. 35, No. 6, (2005), 1224-1232. <https://doi.org/10.1016/j.cemconres.2004.06.031>
 43. Ren, P., Li, B., Yu, J. G., Ling, T. C., "Utilization of recycled concrete fines and powders to produce alkali-activated slag concrete blocks", *Journal of Cleaner Production*, Vol. 267, (2020), 122115. <https://doi.org/10.1016/j.jclepro.2020.122115>
 44. Lee, S., Lee, C., "Fire resistance of reinforced concrete bearing walls subjected to all-sided fire exposure", *Materials and Structures*, Vol. 46, No. 6, (2013), 943-957. <https://doi.org/10.1617/s11527-012-9945-8>
 45. Hertz, K. D., "Limits of spalling of fire-exposed concrete", *Fire Safety Journal*, Vol. 38, No. 2, (2003), 103-116. [https://doi.org/10.1016/S0379-7112\(02\)00051-6](https://doi.org/10.1016/S0379-7112(02)00051-6)
 46. Phan, L. T., Lawson, J. R., Davis, F. L., "Effects of elevated temperature exposure on heating characteristics, spalling, and residual properties of high performance concrete", *Materials and Structures*, Vol. 34, No. 2, (2001), 83-91. <https://doi.org/10.1007/BF02481556>
 47. Bernal, S. A., Rodríguez, E. D., Mejía de Gutiérrez, R., Provis, J. L., "Performance at high temperature of alkali-activated slag pastes produced with silica fume and rice husk ash based activators", *Materiales De Construcción*, Vol. 65, No. 318, (2015), e049. <http://doi.org/10.3989/mc.2015.03114>
 48. Zuda, L., Rovnanik, P., Bayer, P., Černý, R., "Thermal properties of alkali-activated slag subjected to high temperatures", *Journal of Building Physics*, Vol. 30, No. 4, (2007), 337-350. <https://doi.org/10.1177/1744259106075234>
 49. Zuda, L., Pavlík, Z., Rovnaniková, P., Bayer, P., Černý, R., "Properties of alkali activated aluminosilicate material after thermal load", *International Journal of Thermophysics*, Vol. 27, No. 4, (2006), 1250-1263. <https://doi.org/10.1007/s10765-006-0077-7>
 50. Guerrieri, M., Sanjayan, J. G., "Behavior of combined fly ash/slag-based geopolymers when exposed to high temperatures", *Fire and Materials: An International Journal*, Vol. 34, No. 4, (2010), 163-175. <https://doi.org/10.1002/fam.1014>
 51. Mithun, B. M., Narasimhan M. C., "Performance of alkali activated slag concrete mixes incorporating copper slag as fine aggregate", *Journal of Cleaner Production*, Vol. 112, (2016), 837-844. <https://doi.org/10.1016/j.jclepro.2015.06.026>
 52. Kathirvel, P., Kaliyaperumal, S. R. M., "Influence of recycled concrete aggregates on the flexural properties of reinforced alkali activated slag concrete", *Construction and Building Materials*, Vol. 102, (2016), 51-58. <https://doi.org/10.1016/j.conbuildmat.2015.10.148>
 53. Parthiban, K., Mohan, K. S. R., "Influence of recycled concrete aggregates on the engineering and durability properties of alkali activated slag concrete", *Construction and Building Materials*, Vol. 133, (2017), 65-72. <https://doi.org/10.1016/j.conbuildmat.2016.12.050>
 54. Shi, C., Stegemann, J. A., "Acid corrosion resistance of different cementing materials", *Cement and Concrete Research*, Vol. 30, No. 5, (2000), 803-808. [https://doi.org/10.1016/S0008-8846\(00\)00234-9](https://doi.org/10.1016/S0008-8846(00)00234-9)
 55. Bakharev, T., Sanjayan, J. G., Cheng, Y. B., "Resistance of alkali-activated slag concrete to carbonation", *Cement and Concrete Research*, Vol. 31, No. 9, (2001), 1277-1283. [https://doi.org/10.1016/S0008-8846\(01\)00574-9](https://doi.org/10.1016/S0008-8846(01)00574-9)
 56. Collins F., Sanjayan J. G., "Effect of pore size distribution on drying shrinking of alkali-activated slag concrete", *Cement and Concrete Research*, Vol. 30, No. 9, (2000), 1401-1406. [https://doi.org/10.1016/S0008-8846\(00\)00327-6](https://doi.org/10.1016/S0008-8846(00)00327-6)
 57. Atiş, C. D., Bilim, C., Çelik, Ö., Karahan, O., "Influence of activator on the strength and drying shrinkage of alkali-activated slag mortar", *Construction and Building Materials*, Vol. 23, No. 1, (2009), 548-555. <https://doi.org/10.1016/j.conbuildmat.2007.10.011>
 58. Lee, N. K., Lee, H. K., "Setting and mechanical properties of alkali-activated fly ash/slag concrete manufactured at room temperature", *Construction and Building Materials*, Vol. 47 (2013), 1201-1209. <https://doi.org/10.1016/j.conbuildmat.2013.05.107>
 59. Puertas, F., Torres-Carrasco, M., "Use of glass waste as an activator in the preparation of alkali-activated slag: Mechanical strength and paste characterization", *Cement and Concrete Research*, Vol. 57, (2014), 95-104. <https://doi.org/10.1016/j.cemconres.2013.12.005>
 60. Zhou, X., Zeng, Y., Chen, P., Jiao, Z., Zheng, W., "Mechanical properties of basalt and polypropylene fibre-reinforced alkali-activated slag concrete", *Construction and Building Materials*, Vol. 269, (2021), 121284. <https://doi.org/10.1016/j.conbuildmat.2020.121284>
 61. Yuan, X. H., Chen, W., Lu, Z. A., Chen, H., "Shrinkage compensation of alkali-activated slag concrete and microstructural analysis", *Construction and Building Materials*, Vol. 66, (2014), 422-428. <https://doi.org/10.1016/j.conbuildmat.2014.05.085>
 62. Xiang, J., He, Y., Liu, L., Zheng, H., Cui, X., "Exothermic behavior and drying shrinkage of alkali-activated slag concrete by low temperature-preparation method", *Construction and Building Materials*, Vol. 262, (2020), 120056. <https://doi.org/10.1016/j.conbuildmat.2020.120056>
 63. Ye, H., Radlińska, A., "Shrinkage mitigation strategies in alkali-activated slag", *Cement and Concrete Research*, Vol. 101, (2017), 131-143. <https://doi.org/10.1016/j.cemconres.2016.07.001>
 64. Fu-Sheng, W., Rui-Lian, S., Ying-Jing, C., "Study on modification of the high-strength slag cement material", *Cement and Concrete Research*, Vol. 35, No. 7, (2005), 1344-1348. <https://doi.org/10.1016/j.cemconres.2004.10.017>
 65. Duan, Z., Singh, A., Xiao, J., Hou, S., "Combined use of recycled powder and recycled coarse aggregate derived from construction and demolition waste in self-compacting concrete", *Construction and Building Materials*, Vol. 254, (2020), 119323. <https://doi.org/10.1016/j.conbuildmat.2020.119323>
 66. Liu, Q., Li, B., Xiao, J., Singh, A., "Utilization potential of aerated concrete block powder and clay brick powder from C&D waste", *Construction and Building Materials*, Vol. 238, (2020), 117721. <https://doi.org/10.1016/j.conbuildmat.2019.117721>
 67. Duan, Z., Hou, S., Xiao, J., Li, B., "Study on the essential properties of recycled powders from construction and demolition waste", *Journal of Cleaner Production*, Vol. 253, (2020),

119865. <https://doi.org/10.1016/j.jclepro.2019.119865>
68. Qian, G., Sun, D. D., Tay, J. H., "Characterization of mercury- and zinc-doped alkali activated slag matrix: part I. Mercury", *Cement and Concrete Research*, Vol. 33, No. 8, (2003), 1251–1256. [https://doi.org/10.1016/S0008-8846\(03\)00045-0](https://doi.org/10.1016/S0008-8846(03)00045-0)
69. Yunsheng, Z., Wei, S., Qianli, C., Lin, C., "Synthesis and heavy metal immobilization behaviors of slag based geopolymer", *Journal of hazardous materials*, Vol. 143, No. 1-2, (2007), 206-213. <https://doi.org/10.1016/j.jhazmat.2006.09.033>
70. Deja, J., "Immobilization of Cr⁺⁶, Cd⁺², Zn⁺² and Pb⁺² in alkali activated slag binders", *Cement and Concrete Research*, Vol. 32, No. 12, (2002), 1971-1979. [https://doi.org/10.1016/S0008-8846\(02\)00904-3](https://doi.org/10.1016/S0008-8846(02)00904-3)



Materials and Energy Research Center

MERC

Contents lists available at [ACERP](#)

Advanced Ceramics Progress

Journal Homepage: www.acerp.ir

Advanced Ceramics Progress

Original Research Article

Fabrication and Preliminary Characterization of Tissue Engineering Scaffolds Based on Alumina/Bioactive Glass

S. Borhan ^{a,*}, M. R. Badr-Mohammadi ^b, S. Hesaraki ^c, J. Esmailzadeh ^d^a Assistant Professor, Department of Materials, Chemical and Polymer Engineering, Imam Khomeini International University-Buin Zahra Higher Education Center of Engineering and Technology, Buin Zahra, Qazvin, Iran^b MSc, Department of Nanotechnology and Advanced Materials, Materials and Energy Research Center (MERC), Meshkindasht, Alborz, Iran^c Professor, Department of Nanotechnology and Advanced Materials, Materials and Energy Research Center (MERC), Meshkindasht, Alborz, Iran^d Assistant Professor, Department of Materials and Chemical Engineering, Esfarayen University of Technology, Esfarayen, North Khorasan, Iran* Corresponding Author Email: shkfborhan@bzte.ac.ir (S. Borhan)URL: https://www.acerp.ir/article_143925.html

ARTICLE INFO

ABSTRACT

Article History:

Received 06 January 2022

Received in revised form 26 January 2022

Accepted 29 January 2022

Keywords:

Alumina Scaffold
Bioactive Glass
Cell Culture
Coating
Porosity

Many researches have been conducted so far to improve the bioactivity and mechanical properties of bioceramic-based scaffolds in order to stimulate tissue attachment to the implant surface and create a stable bonding. In this research, Al₂O₃ scaffolds were prepared using different types of polyurethane foam through template replica method and then, they were sintered at 1650 °C. A sol of SiO₂-CaO-P₂O₅-MgO system Bioactive Glass (BG) was synthesized where the scaffolds were soaked and heat-treated at 800 °C based on thermo gravimetry analysis. X-ray diffraction confirmed the presence of silica in the structure of BG coating diffused in alumina scaffold that caused the formation of sillimanite phase. According to Scanning Electron Microscopy (SEM) analysis, all prepared scaffolds were highly porous, and the mean porosity percentage was approximately 85 %. The compressive strength and porosity percentage of the scaffolds nearly ranged between 0.35-1.75 MPa and 79-93 %, respectively. The sample with the best result of compressive strength was considered as the optimum alumina scaffold (OAS). In vitro acellular behavior of the samples was also evaluated followed by soaking them in the simulated body fluid, and the ball-like morphology including entangled needle-like crystals were observed on the surface of the sample. Moreover, cells were cultured in alumina scaffolds with and without BG coating and in the cell studies. According to the findings, both samples supported attachment and proliferation of osteoblasts. Therefore, Based on the scaffold porosity percentage which promotes cell attachment as well as the compressive strength which is close to that of the trabecular bone, it can be concluded that application of BG-coated alumina scaffold as a bone-healing material may be beneficial.

<https://doi.org/10.30501/ACP.2022.323414.1079>

1. INTRODUCTION

Bone tissue injuries significantly affect the lives of millions of people worldwide. Some common treatment methods such as autologous and allogeneic bone grafting

cannot produce the ideal therapeutic effect; to be specific, allograft bone transplantation may cause several side effects such as negligible osseointegration, immune rejection, and blood disease. To overcome these problems, Bone Tissue Engineering (BTE) was

Please cite this article as: Borhan, S., Badr-Mohammadi, M. R., Hesaraki, S., Esmailzadeh, J., "Fabrication and Preliminary Characterization of Tissue Engineering Scaffolds Based on Alumina/Bioactive Glass", *Advanced Ceramics Progress*, Vol. 7, No. 4, (2021), 10-19. <https://doi.org/10.30501/ACP.2022.323414.1079>

2423-7485/© 2021 The Author(s). Published by MERC.

This is an open access article under the CC BY license (<https://creativecommons.org/licenses/by/4.0/>).

introduced to promote the already available techniques for lost bone regeneration using a combination of cells, growth factors, and biomaterials, maintain the stable state of tissue, and enhance/replace the function of target tissues. This approach enjoys several advantages such as high flexibility, low risk of infection, and great biocompatibility [1-3].

Tissue Engineering (TE) is currently used as a considerable successful technique in a wide variety of fields to repair and reconstruct tissues and organs such as bone, skin, cartilage, liver, bladder, ligament, nerves, cardiac valves, etc. This is the main reason why TE is still an interesting subject of many investigations. The overall objective of TE scaffolds is to provide the cells with a temporary matrix to generate new tissues of favorable shapes and dimensions. Of note, given that the scaffold should be characterized by suitable physical, mechanical, and biological properties, one of the challenges in TE is construction of a porous biodegradable scaffold. Moreover, it should possess individual and particular morphology and microstructure [4,5].

A number of different scaffolds (organic and inorganic or hybrid of them) have been fabricated so far among which, bioceramic scaffolds are amazingly appreciated owing to their unique properties such as biocompatibility and biodegradability. However, along with these appropriate characteristics, they also have some mechanical properties. In this regard, many studies have been conducted to overcome this weakness [6,7].

Alumina scaffolds are extensively used owing to their high biocompatibility, excellent wear resistance, and hardness; however, they are inert in body. Therefore, the combination of Alumina scaffolds with a bioactive material would result in a better biocompatibility and maintenance. Kim et al. evaluated Tricalcium Phosphate (TCP) coated and non-coated alumina scaffolds. TCP-coated scaffolds exhibit favorable bone tissue ingrowth [8]. Naga et al. conducted a study on the bioactivity of the porous alumina scaffolds coated with calcium pyrophosphate. Histological analysis revealed that the produced scaffold can be used as the bone substitute [9]. In another research, porous alumina matrix was dipped into bioglass/hydroxyapatite ceramic slurry and then sintered. The evaluation confirmed the higher cell interaction of the coated porous alumina than that of non-coated alumina scaffolds [10].

The main objective of the current research is to prepare an alumina scaffold to obtain good mechanical properties and coat it by a ternary system of bioactive glass (BG) to obtain suitable bioactivity. Alumina is a bioinert ceramic with fantastic mechanical strength, yet it is not bioactive [11]. In contrast to alumina, BG is a kind of bioceramic with the ability to bond with host tissues through formation of a calcium phosphate layer at their interface to live tissues. However, it has a considerable drawback, i.e., low mechanical strength [12]. It seems that the

alumina coated with BG produces a bioactive scaffold with proper mechanical properties.

2. MATERIALS AND METHODS

2.1. Preparation of Specimens

Alumina scaffolds were made using polyurethane foams. First, alumina (Martoxid® MR70, Albemarle, Germany), distilled water, and polyvinyl alcohol (PVA, 363138 Aldrich, Germany), as the binder, were mixed together and milled for 24 h to achieve a homogenous slurry. Then, the foam samples of $1 \times 1 \times 1$ cm³ in dimension were immersed in the slurry of alumina to smear all sides of the foams. Next, the foams were taken out from the suspension and squeezed to remove the excessive slurry. In this step, three types of polyurethane were used (30, 45, and 60 Pores Per Inch (PPI)). The foams were then dried at 70 °C and sintered with a certain heat-treatment program. Samples were then heated to 300 °C with the rate of 1 °C/min and remained at 300 °C for one hour to remove polymeric substrate. Finally, they were heated to 1650 °C at a rate of 5 °C/min and then sintered and stabilized at this temperature for three hours [11].

BG based on 64 SiO₂, 26 CaO, 5 MgO, and 5 P₂O₅ (% mol) system was synthesized based on water-based sol-gel process. In this process, 13.33 g of Tetraethyl Orthosilicate (TEOS, 800625 Merck, Germany) was poured into 30 mL of 0.1 M Nitric Acid (HNO₃, 1004562500 Merck, Germany) solution and stirred for one hour at room temperature to complete acid hydrolysis. The following compounds were added in sequence, giving 45 min to each reagent to react completely: 0.91 g triethylphosphate (TEP: 821141 Merck, Germany), 6.14 g of calcium nitrate tetrahydrate (Ca(NO₃)₂·4H₂O, 102123 Merck, Germany), and 1.28 g of magnesium nitrate hexahydrate (Mg(NO₃)₂·6H₂O, Merck 107871, Germany). After the final addition, the mixture was stirred for an hour to obtain a transparent sol. Now, it is ready to be used for coating on alumina scaffolds.

In this stage, the sintered scaffolds were soaked in the BG sol for a few seconds. This procedure was repeated three times to obtain appropriate coatings. At the end, the coated samples were dried at 70 °C for 24 h. The sintering temperature was 800 °C in accordance with the Thermo-Gravimetric Analysis (TGA) of BG. The resultant scaffolds were heat-treated at this temperature for two hours to obtain the proper chemical bonding between the glass and alumina.

2.2. TGA and DTA Analyses

The thermal behavior of BG was studied through Differential Thermal Analysis (DTA) and Thermo Gravimetry (TG) analysis. For this purpose, the obtained sol was poured into a cylindrical teflon container and kept sealed for 10 days at room temperature until the

occurrence of the polycondensation reaction. The formed gel was dried at 70 °C for 3 days and then at 120 °C for 2 days. The dried gel was analyzed using PL-STA 1600-England apparatus under the air atmosphere and heated from room temperature to 1200 °C with the heating rate of 10 °C/min.

2.3. X-Ray Diffraction Analysis

Phase analysis of the scaffolds was carried out using a Philips PW3710 diffractometer. This apparatus worked with the voltage of 40 kV, current of 30 mA, and applied Cu-K α radiation (1.54 Å). The required data were collected in the range of $10^\circ \leq 2\theta \leq 80^\circ$ at the scan speed of 2 °/min.

2.4. Morphology Observations

The morphologies of the pores and pore walls in the scaffolds were observed using Scanning Electron Microscopy (SEM) (Stereoscan S360-Cambridge, UK), functioning at the acceleration voltage of 15 kV. First, samples were coated with a thin layer of Au using the sputtering instrument. The elemental image analysis of the scaffolds was determined by Energy Dispersive Spectroscopy (EDS) that was directly connected to SEM. According to previous similar studies [13-15], the pore size was measured by Image J software, and the mean porosity diameter was defined as the pore size of scaffolds.

2.5. Porosity Percentage Measurement of Scaffolds

To measure the porosity percentage of the scaffolds, they were well-milled by agate mortar. The true density of the sintered powder was calculated based on the standard ASTM D 2320-87 through pycnometer method. The amounts of mass and volume were also calculated to measure the bulk density of the sintered samples.

2.6. Mechanical Test

The mechanical properties of the samples were measured based on compressive strength test. The cylindrical samples were fabricated (15 mm in diameter and 20 mm in height), and the compressive strength of the samples was evaluated through universal testing device (STM 20, SANTAM Ltd, Iran) equipped with a 100 N load cell at the cross head speed of 1 mm/min. The following equations were used for calculating Young's modulus (E) (1) and ultimate compressive stress (σ) (2):

$$E = \frac{KL}{A} \quad (1)$$

$$\sigma = \frac{F}{A} \quad (2)$$

where K is the stiffness, L the length of sample, F the ultimate load, and A the average of surface area obtained from Eq. (3):

$$A = \frac{\pi}{2} \times \frac{1}{4} \times (d_1^2 - d_2^2) \quad (3)$$

where d_1 and d_2 are the diameters of the cylindrical specimens. The slope of the stress-strain curve at the fracture point is the value of K. The test was repeated three times for each sample.

2.7. Evaluation of in Vitro Acellular Behavior

The in vitro surface activity of the scaffolds was evaluated after soaking them in Simulated Body Fluid (SBF) at the solid-to-liquid ratio (S/L) of 1 g/100 mL and then, they were kept at 37 °C for several periods up to 28 days. The SBF solution was prepared based on the procedure suggested by Kokubo et al. [16] by dissolving NaCl 8.035 g/L, KCl 0.225 g/L, K₂HPO₄·3H₂O 0.231 g/L, MgCl₂·6H₂O 0.311 g/L, CaCl₂ 0.292 g/L, NaHCO₃ 0.355 g/L, and Na₂SO₃ 0.072 g/L into distilled water, buffered at pH=7.25 with 6.118 g/L tris-hydroxymethyl aminomethane and 1 N HCl solution at 37 °C. The SBF solution was selected due to its highly supersaturated characteristic in terms of apatite. According to Oyane and Takadama [17,18], SBF is the best solution to evaluating the apatite-formation ability in biomaterials. The microstructure and surface morphology of the samples were observed using SEM after soaking them in the SBF solution for 14 and 28 days.

2.8. Procedure of Cell Culture and MTT Assay

Osteoblast-like cells of human (SaOS-2) were cultured in Dulbecco Modified Eagle Medium (DMEM; Gibco-BRL, Life Technologies, Grand Island, NY) supplemented with 15 % fetal bovine serum (FBS) (Dainippon Pharmaceutical, Osaka, Japan) in a 5 % CO₂ atmosphere at 37 °C. The scaffolds (with dimensions of 0.5×0.5×0.5 cm³) were sterilized using 70 % ethanol, and the cells were seeded over them at 2×10⁴ cells/well [19]. Similarly, discs with similar dimensions were prepared from the culture dish (polystyrene) and used as the control group. The sample/cell constructs were placed into 24-well culture plates and left in an incubator for three hours to allow cell attachment. Next, 3 mL of culture medium was added into each well, and the cell/specimen constructs were cultured in a humidified incubator at 37 °C with 95 % air and 5 % CO₂ for 2 and 7 days. The medium was changed every 3 days.

SEM was employed to monitor the morphology of the attached cells. For this purpose, followed by cell fixation, the specimens were dehydrated in ethanol solutions for about 20 min. They were then dried in the air, coated with gold, and analyzed by SEM.

The cell proliferation in contact with the samples was measured by using water soluble enzyme substrate 3-(4,5-dimethylthiazol-2-yl)-2,5-diphenyl tetrazolium bromide (MTT, Sigma, Germany), which turned into a purple water insoluble product formazan accumulated in

the cytoplasm of viable cells. In this regard, at the end of each period, the medium was removed, and 2 mL of MTT solution was added to each well. Followed by incubation at 37 °C for four hours in a fully humidified atmosphere (5 % CO₂/95 % air), MTT was taken up by active cells and reduced to insoluble purple formazan granules in mitochondria. Subsequently, the medium was thrown away, the precipitated formazan was dissolved in dimethyl sulfoxide (DMSO, Sigma, Germany) (150 mL/well), and the optical density of the solution was measured using a microplate spectrophotometer (BIOTEK Elx 800, Highland park, USA) at 570 nm. Cell number was determined using a linear correlation between the absorbance and cell concentration.

2.9. Statistical Analysis

Data were calculated by Microsoft Excel 2019 software, the results of which were reported as the mean ± standard deviation of at least three experiments. The significance among the mean values was determined using standard software program (SPSS GmbH, Munich, Germany) such that the probability values less than 0.05 ($P \leq 0.05$) were considered significant.

3. RESULTS AND DISCUSSION

The DTA and TG analyses of the BG were carried out to acquire the exact sintering temperature, as shown in Figure 1. The first endothermic peak initiated at 120 °C corresponds to the release of physically adsorbed water. According to the TGA diagram, it was removed between 50 °C and 150 °C (No. 1). There is an exothermic peak at 320 °C which can be attributed to the release of structural water that leads to weight loss between 150 °C and 400 °C (No. 2). Two other endothermic peaks (No. 3 and 4), started at 550 °C, are associated with the removal of silanol and nitrate groups that are usually eliminated in the thermal stabilization process [20]. Approximately 10 % of the total weight loss occurred by removal of all nitrates at 600 °C. Finally, the crystallization process of CaSiO₃ (β -wollastonite) and cristobalite (SiO₂) was completed around 970 °C (No. 6) [20], which was found to occur at higher temperatures in similar glasses [21,22].

Negligible weight loss was observed above 700 °C, indicating that the residuals were removed before 700 °C [4], hence this temperature was found to be proper for stabilization of the glass structure. Of note, the glass transition temperature of the dried gel occurred at about 800 °C (No. 5). Controlling the sintering temperature is a fundamental factor that affects apatite formation. As reported, the heat treatment of the bioglass as a coating affected bioactivity. According to the studies, an imperfect apatite layer was formed on the bioglass. In fact, crystallisation decreased the bioactivity of the bioglass that was coated on the porous alumina scaffold and prepared by slip casting [23].

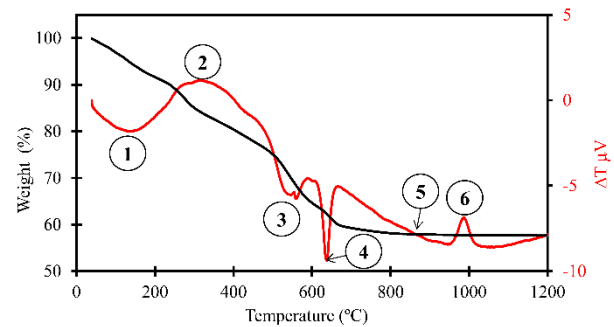


Figure 1. DTA (red line) and TG (black line) analyses of the BG

Figure 2 illustrates the XRD patterns of the sintered alumina at 1700 °C, stabilized BG at 800 °C, and coated scaffold. No diffraction peak was observed in the XRD pattern of BG, and the sample was almost amorphous due to its internal disorder. In this respect, 800 °C was selected as the suitable temperature for BG stabilization. According to the pattern of the coated alumina scaffold, the corundum phase (JCPDS Card No 46-1212) at pure alumina scaffold was converted to sillimanite (a composition of Al₂O₃-SiO₂) with JCPDS Card No 22-0018 partially followed by sintering at 800 °C, indicating that the silica in the structure of BG was diffused in alumina scaffold, hence formation of the sillimanite phase.

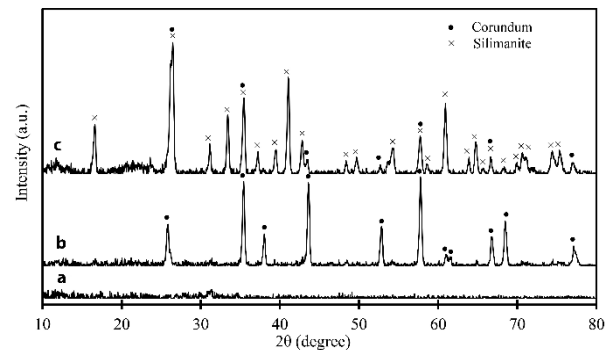


Figure 2. X-Ray diffraction patterns of a) BG stabilized at 800 °C, b) Sintered alumina at 1650 °C, and c) BG coated Al-scaffold

Figure 3 shows the micrograph of the sintered scaffolds prepared by different polyurethane foams. As expected, all prepared scaffolds through replica method were highly porous so that the size of pores and their walls increased by decreasing PPI. The mean size of the pores and their walls were estimated using Image J software and SEM images. The given data in Table 1 show that the average pore size of the scaffold prepared by 30 PPI foam is 1133 μm which decrease to 376 μm in the sample prepared by 60 PPI foam. The results of the calculated porosity percentage from Equation 1 are also given in

Table 1. The prepared sample with 60 PPI foam had the highest porosity percentage. On the contrary, the porous alumina-based ceramics fabricated by Polymethylmethacrylate (PMMA) microspheres had the mean pore size of about 22.6 μm and open porosity percentage of 62 %. In other words, they had smaller pore size and less porosity percentage than those of the scaffolds prepared by foam replica, hence higher mechanical strength can be expected [24].

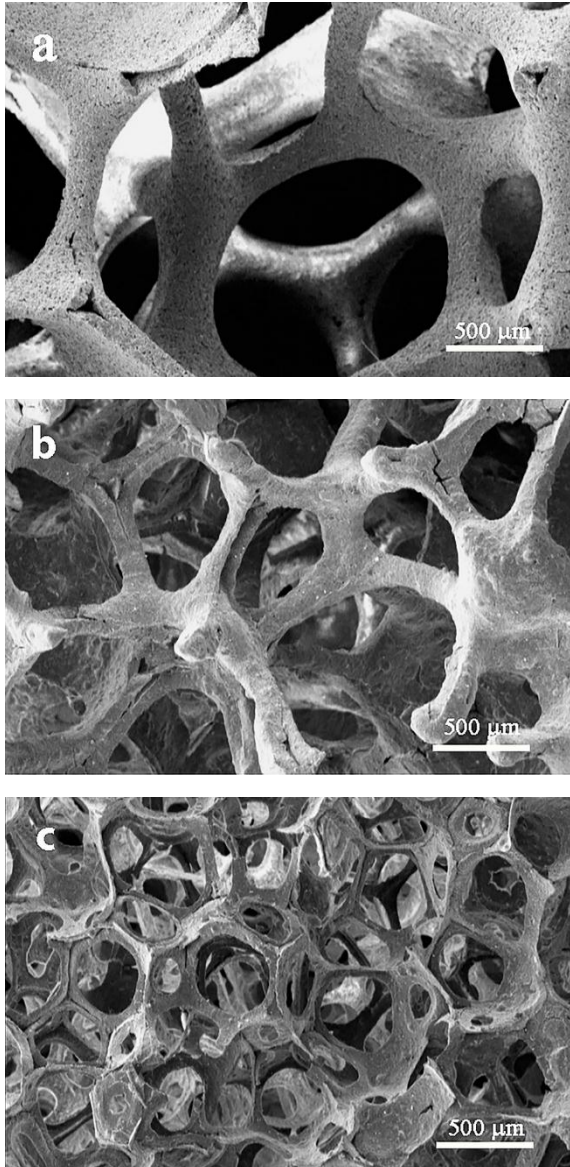


Figure 3. SEM images of scaffolds prepared by a) 30 PPI, b) 45 PPI, and c) 60 PPI polyurethane foams

Table 1 presents the results of the mechanical strength of the scaffolds. According to this table, the compressive strength decreased upon increasing the porosity percentage of the scaffolds. The compressive strength of

the scaffold prepared by 30 PPI foam was 1.75 MPa which was higher than that of the other samples. The compressive strength of the trabecular bone was between 0.22 MPa and 10.44 MPa, and the mean value was about 3.9 MPa [25-28]. Therefore, this scaffold can be recommended to be used for tissue repair of the trabecular bone. In addition, the porosity diameter of the scaffold prepared through template replica method was considerably high, hence useful for TE applications [22]. Moreover, the scaffold possesses interconnected porosities. Pore connectivity plays an important role in the penetration into the scaffold [29].

TABLE 1. The Characteristics of porosity and mechanical properties of prepared scaffolds with different polyurethane foams

Types of polyurethane foams	30 PPI	45 PPI	60 PPI
Diameter of Pore (μm)	1133 \pm 50	550 \pm 24	376 \pm 13
Diameter of pore's wall (μm)	275 \pm 24	185 \pm 18	79 \pm 11
Calculated porosity (%)	79.5 \pm 0.5	85.05 \pm 0.03	93.41 \pm 0.65
Compressive strength (MPa)	1.75 \pm 0.5	0.51 \pm 0.2	0.35 \pm 0.1

Therefore, the synthesized sample through foam PPI No.: 30 can be regarded as the Optimum Alumina Scaffold (OAS). The composition of OAS is exactly the same as that of other samples (BG coated alumina); they only differ in the applied foam.

To measure the thickness of BG coating, SEM observation at different magnifications was used. As observed in Figure 4, the coating thickness is nearly 1.5 μm , and it is tightly attached to the alumina scaffold. To obtain a strong coating, the thermal expansion coefficients of both substrate and coating layer must be matched. Otherwise, the created thermal stresses between the substrate and coating would cause cracks. In this study, the thermal expansion coefficient of BG was measured based the rule of mixtures as $4.92 \times 10^{-6} \text{ }^\circ\text{C}^{-1}$. The thermal expansion coefficient of alumina was also $9.47 \times 10^{-6} \text{ }^\circ\text{C}^{-1}$. Due to the smaller coefficient value of the BG, the stresses in the coating would be compressive, thus forming a good bonding between the BG and alumina substrate. Figure 4 presents the EDS analysis of the substrate and coating of OAS. All of the constituent elements of the BG were identifiable in the the coating layer. The elements of Al and Si were also found in the substrate. The presence of Si in the substrate confirmed that the sol was infiltrated into the scaffold structure which in turn led to the formation of a new phase of $\text{Al}_2\text{O}_3\text{-SiO}_2$ in accordance with the XRD results.

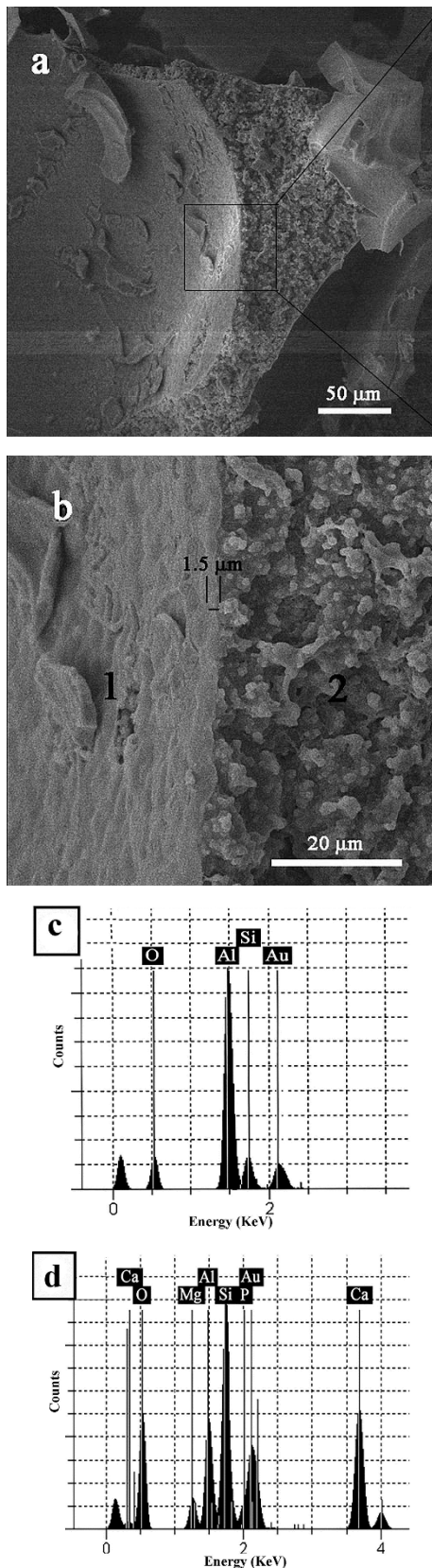


Figure 4. SEM of the BG coated alumina scaffold at different magnifications a) 400 X, b) 2000 X, and EDS analysis of c) the coating (point 1) and d) the substrate (point 2) of the scaffold

Figure 5 illustrates the BG-coated OASs after 14 and 28 days of immersion in SBF solution. As seen, the hydroxyapatite layer with a spherical morphology was precipitated after 14 days. Obviously, a ball-like morphology containing the entangled crystals was observed on the surface of the sample after 28 days. This kind of apatite morphology is formed through the dissolution-precipitation mechanism. According to other researches [30], changes in the surface chemistry and topography in vitro were controlled by the solubility of the different phases. The reaction between the phosphate ions of SBF and released calcium ions by the material cause the nucleation of a calcium-deficient hydroxyapatite layer. These surfaces were formed after 28 days due to the abovementioned mechanism [31]. The elemental image analyses of the surface are illustrated in the corner of Figure 5. The presence of Ca and P peaks determines the formation of a calcium phosphate layer.

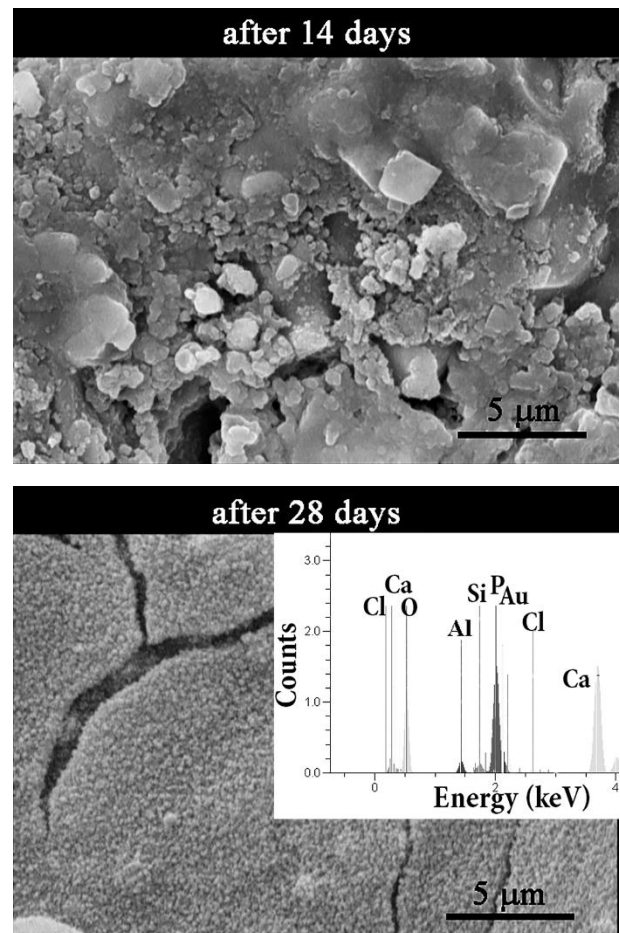


Figure 5. SEM observation of the BG coated alumina scaffold after 14 and 28 days of soaking in SBF solution. (in the corner: EDS analysis of the surface)

Figure 6 shows the SEM micrographs of alumina scaffolds and BG-coated OASs after 2 and 7 days of

osteoblastic cell culture in different magnifications. SEM is a beneficial method to detecting the morphology and distribution of cells on the surface of scaffolds [32]. According to this figure, Alumina did not adversely

affect cell proliferation, and cells were properly attached and spread on the surface due to the compatibility and proper topography of the samples in terms of cell growth. The cells are marked with white arrows in Figure 6.

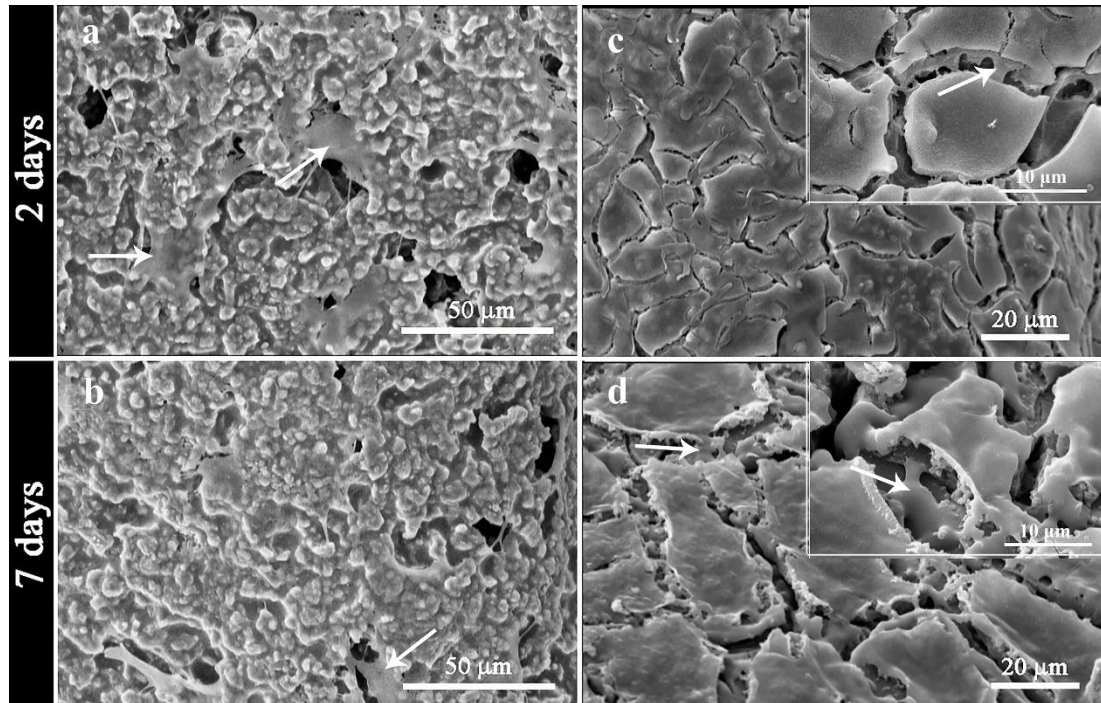


Figure 6. SEM micrographs of alumina scaffolds a) after 2 days, b) after 7 days, BG coated alumina scaffolds c) after 2 days and d) after 7 days of osteoblastic cell culture (at the corner of image, higher magnification is observed where white arrows indicate spread cells)

The obtained results were in good agreement with those from another research carried out by Bose and et al. [33]. Apparently, after 7 days, the cells covered a larger area of the scaffold surface. In case the matrix is inappropriate or toxic, the cells would be less extended over the surface [34].

The cytotoxicity study on the specimens was conducted using the MTT colorimetric method to confirm the microscopic observations. Figure 7 shows the proliferation of the osteoblasts on different specimens. The results of the studies at 2 and 7 days revealed that the number of cells on the surfaces of aluminum and BG-coated aluminum scaffolds increased significantly with time. The differences in the cell numbers between days 2 and 7 are statistically significant ($P \leq 0.05$); therefore, after cell attachment, proliferation begins on all samples. On days 2 and 7, the numbers of cells proliferated on aluminum and BG-coated aluminum scaffolds were compared, and it was found that the differences between the average values were not statistically important. However, the number of cells on polystyrene was extremely lower than that of aluminum

and BG-coated aluminum scaffolds with no cytotoxicity of the samples.

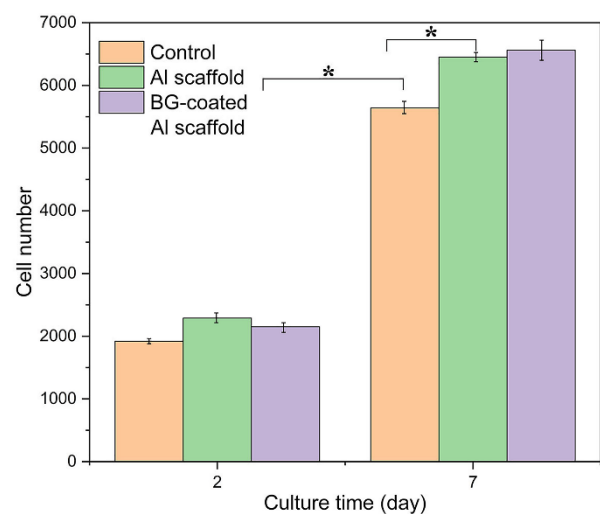


Figure 7. Proliferation of osteoblasts on Al scaffold, BG-coated Al scaffold, and control sample measured by MTT assay ($*P \leq 0.05$)

The scaffold material provides a substrate for cell attachment, proliferation, and differentiation [35]. In order to obtain a scaffold for bone regeneration in this study, both alumina and BG-coated based scaffolds were prepared. The surface topography of the biomaterial affected cellular responses in vitro preferably, hence bioactive materials should interact with cells to motivate cell ingrowth [36]. Cell attachment is the primary stage of the interaction between the cells and biomaterial [37]. The surface of the biomaterials affects the morphology of cells that define biocompatibility [38]. The SEM results of cell morphology revealed that cell cover on the surface of COAS was better than that of OAS. In other words, cellular responses to biomaterials depends not only on the surface morphology but on the chemical composition of the biomaterial [39], which plays a fundamental role in determining interaction between the cells and materials by changing the quantity of the released ions from the biomaterial [40]. In this study, a sol-gel derived bioactive glasses containing SiO₂, CaO, and P₂O₅ was selected as the coating. SiO₂ is a network former in the glass structure. Moreover, Si-OH groups produced from the exchange process of Ca²⁺ ions (from glass) with H₃O⁺ (from solution) are susceptible sites for calcium phosphate nucleation [41,42]. At the same time, Si ions released from the glass composition into the medium can accelerate cell functions [43,44]. P₂O₅ is also used to encourage nucleation of calcium phosphate phase on the glass surfaces [45].

4. CONCLUSIONS

The following conclusions can be derived from this study:

- Alumina was transformed to sillimanite phase when coating the alumina scaffold with BG as a result of the diffusion of silicon into the scaffold as well as the reaction of alumina with silicon.
- The mechanical strength decreased upon increasing the porosity percentage of the scaffolds.
- According to the SEM observation, the spherical hydroxyapatite particles were formed well on the surface of BG-coated alumina scaffold after different time intervals of being soaked in SBF solution.
- According to the preliminary in vitro test data, both alumina and BG-coated scaffolds were not toxic after processing, and they provided favorite sites for cell attachment and proliferation for SaOS-2 cells.
- The bioactivity properties of the BG-coated alumina scaffold were significant since they exhibited acceptable cell attachment and cell growth. The results of experiments confirmed the application of the prepared scaffold in bone regeneration field.

ACKNOWLEDGEMENTS

The authors wish to acknowledge Imam Khomeini International University-Buin Zahra Higher Education Center of Engineering and Technology and Materials and Energy Research Center (MERC) for the all supports.

REFERENCES

1. Ramay, H. R., Zhang, M., "Biphasic calcium phosphate nanocomposite porous scaffolds for load-bearing bone tissue engineering", *Biomaterials*, Vol. 25, No. 21, (2004), 5171-5180. <https://doi.org/10.1016/j.biomaterials.2003.12.023>
2. Zhu, G., Zhang, T., Chen, M., Yao, K., Huang, X., Zhang, B., Li, Y., Liu, J., Wang, Y., Zhao, Z., "Bone physiological microenvironment and healing mechanism: basis for future bone-tissue engineering scaffolds", *Bioactive Materials*, Vol. 6, No. 11, (2021), 4110-4140. <https://doi.org/10.1016/j.bioactmat.2021.03.043>
3. Alonzo, M., Primo, F. A., Kumar, S. A., Mudloff, J. A., Dominguez, E., Fregoso, G., Ortiz, N., Weiss, W. M., Joddar, B., "Bone tissue engineering techniques, advances, and scaffolds for treatment of bone defects", *Current Opinion in Biomedical Engineering*, Vol. 17, (2021), 100248. <https://doi.org/10.1016/j.cobme.2020.100248>
4. Tsang, V. L., Bhatia, S. N., "Three-dimensional tissue fabrication", *Advanced Drug Delivery Reviews*, Vol. 56, No. 11, (2004), 1635-1647. <https://doi.org/10.1016/j.addr.2004.05.001>
5. Bohner, M., Van Lenthe, G. H., Grünenfelder, S., Hirsiger, W., Evison, R., Müller, R., "Synthesis and characterization of porous β -Tricalcium phosphate blocks", *Biomaterials*, Vol. 26, No. 31, (2005), 6099-6105. <https://doi.org/10.1016/j.biomaterials.2005.03.026>
6. Zhang, J., Wu, L., Jing, D., Ding, J., "A comparative study of porous scaffolds with cubic and spherical macropores", *Polymer*, Vol. 46, No. 13, (2005), 4979-4985. <https://doi.org/10.1016/j.polymer.2005.02.120>
7. Sokolsky-Papkov, M., Agashi, K., Olaye, A., Shakesheff, K., Domb, A. J., "Polymer carriers for drug delivery in tissue engineering", *Advanced Drug Delivery Reviews*, Vol. 59, No. 4-5, (2007), 187-206. <https://doi.org/10.1016/j.addr.2007.04.001>
8. Kim, Y. H., Anirban, J. M., Song, H. Y., Seo, H. S., Lee, B. T., "In vitro and In vivo evaluations of 3D porous TCP-coated and non-coated alumina scaffolds", *Journal of Biomaterials Applications*, Vol. 25, No. 6, (2011), 539-558. <https://doi.org/10.1177/0885328209356945>
9. Naga, S. M., Awaad, M., El-Maghraby, H. F., El-Kady, A. M., "Biological performance of calcium pyrophosphate-coated porous alumina scaffolds", *International Journal of Applied Ceramic Technology*, Vol. 11, No. 1, (2014), 1-11. <https://doi.org/10.1111/ijac.12076>
10. Camilo, C. C., Fortulan, C. A., Ikegami, R. A., Santos, A. R., Purquerio, B. de M., "Manufacturing of porous alumina scaffolds with bio-glass and HAp coating: Mechanical and In vitro evaluation", In Prado M., Zavaglia, C. (eds.), *Key Engineering Materials*, Trans Tech Publications Ltd., Switzerland, Vol. 396-398, (2009), 679-682. <https://doi.org/10.4028/www.scientific.net/KEM.396-398.679>
11. Jun, Y. K., Kim, W. H., W., Kweon, O. K., Hong, S. H., "The fabrication and biochemical evaluation of alumina reinforced calcium phosphate porous implants", *Biomaterials*, Vol. 24, No. 21, (2003), 3731-3739. [https://doi.org/10.1016/S0142-9612\(03\)00248-5](https://doi.org/10.1016/S0142-9612(03)00248-5)
12. González, P., Serra, J., Liste, S., Chiussi, S., León, B., Pérez-Amor, M., Martínez-Fernández, J., de Arellano-López, A. R., Varela-Feria, F. M., "New biomorphic SiC ceramics coated with bioactive glass for biomedical applications", *Biomaterials*, Vol.

- 24, No. 24, (2003), 4827-4832. [https://doi.org/10.1016/S0142-9612\(03\)00405-8](https://doi.org/10.1016/S0142-9612(03)00405-8)
13. Tonda-Turo, C., Gentile, P., Saracino, S., Chiono, V., Nandagiri, V. K., Muzio, G., Canuto, R. A., Ciardelli, G., "Comparative analysis of gelatin scaffolds crosslinked by genipin and silane coupling agent", *International Journal of Biological Macromolecules*, Vol. 49, No. 4, (2011), 700-706. <https://doi.org/10.1016/j.ijbiomac.2011.07.002>
 14. Nadeem, D., Kiamehr, M., Yang, X., Su, B., "Fabrication and in vitro evaluation of a spongelike bioactive-glass/gelatin composite scaffold for bone tissue engineering", *Material Science and Engineering: C*, Vol. 33, No. 5, (2013), 2669-2678. <https://doi.org/10.1016/j.msec.2013.02.021>
 15. Barabadi, Z., Azami, M., Sharifi, E., Karimi, R., Lotfibakhshaiesh, N., Roozafzoon, R., Joghataei, M. T., Ai, J., "Fabrication of hydrogel based nanocomposite scaffold containing bioactive glass nanoparticles for myocardial tissue engineering", *Materials Science and Engineering: C*, Vol. 69, (2016), 1137-1146. <https://doi.org/10.1016/j.msec.2016.08.012>
 16. Kokubo, T., Kushitani, H., Sakka, S., Kitsugi, T., Yamamuro, T., "Solutions able to reproduce in vivo surface-structure changes in bioactive glass-ceramic A-W³⁺", *Journal of Biomedical Material Research*, Vol. 24, No. 6, (1990), 721-734. <https://doi.org/10.1002/jbm.820240607>
 17. Oyane, A., Kim, H. M., Furuya, T., Kokubo, T., Miyazaki, T., Nakamura, T., "Preparation and assessment of revised simulated body fluid", *Journal of Biomedical Materials Research Part A: An Official Journal of The Society for Biomaterials, The Japanese Society for Biomaterials, and The Australian Society for Biomaterials and The Korean Society for Biomaterials*, Vol. 65, No. 2, (2003), 188-195. <https://doi.org/10.1002/jbm.a.10482>
 18. Takadama, H., Hashimoto, M., Mizuno, M., Kokubo, T., "Round-robin test of SBF for In vitro measurement of apatite-forming ability of synthetic materials", *Phosphorus Research Bulletin*, Vol. 17, (2004), 119-125. https://doi.org/10.3363/prb1992.17.0_119
 19. Khorami, M., Hesarak, S., Behnamghader, A., Nazarian, H., Shahrabi, S., "In vitro bioactivity and biocompatibility of lithium substituted 45S5 bioglass", *Material Science and Engineering: C*, Vol. 31, No. 7, (2011), 1584-1592. <https://doi.org/10.1016/j.msec.2011.07.011>
 20. Saravanapavan, P., Jones, J. R., Pryce, R. S., Hench, L. L., "Bioactivity of gel-glass powders in the CaO-SiO₂ system: A comparison with ternary (CaO-P₂O₅-SiO₂) and quaternary glasses (SiO₂-CaO-P₂O₅-Na₂O)", *Journal of Biomedical Materials Research Part A: An Official Journal of The Society for Biomaterials, The Japanese Society for Biomaterials, and The Australian Society for Biomaterials and The Korean Society for Biomaterials*, Vol. 66, No. 1, (2003), 110-119. <https://doi.org/10.1002/jbm.a.10532>
 21. Jones, J. R., Ehrenfried, L. M., Hench, L. L., "Optimising bioactive glass scaffolds for bone tissue engineering", *Biomaterials*, Vol. 27, No. 7, (2006), 964-973. <https://doi.org/10.1016/j.biomaterials.2005.07.017>
 22. Greenspan, D. C., Zhong, J. P., LaTorre, G. P., "Effect of surface area to volume ratio on in vitro surface reactions of bioactive glass particulates", In Andersson, O. H., Happonen, R. P., Yli-Urpo, A. (eds.), Proceedings of the 7th International Symposium on Ceramics in Medicine, *Bioceramics*, Oxford, London: Butterworth-Heinemann, Vol. 7, (1994), 55-60. <https://doi.org/10.1016/B978-0-08-042144-5.50012-1>
 23. Komlev, V. S., Barinov, S. M., "Porous hydroxyapatite ceramics of bimodal pore size distribution", *Journal of Materials Science: Materials in Medicine*, Vol. 13, No. 3, (2002), 295-299. <https://doi.org/10.1023/A:1014015002331>
 24. Kamitani, K., Hyodo, T., Shimizu, Y., Egashira, M., "Fabrication of highly porous alumina-based ceramics with connected spaces by employing PMMA microspheres as a template", *Advanced in Materials Science Engineering*, Vol. 2009, (2009), 601850. <https://doi.org/10.1155/2009/601850>
 25. Misch, C. E., Qu, Z., Bidez, M. W., "Mechanical Properties of Trabecular Bone in the Human Mandible: Implications for Dental Implant Treatment Planning and Surgical Placement", *Journal of Oral and Maxillofacial Surgery*, Vol. 57, No. 6, (1999), 700-706. [https://doi.org/10.1016/S0278-2391\(99\)90437-8](https://doi.org/10.1016/S0278-2391(99)90437-8)
 26. Baptista, R., Guedes, M., "Morphological and mechanical characterization of 3D printed PLA scaffolds with controlled porosity for trabecular bone tissue replacement", *Materials Science and Engineering: C*, Vol. 118, (2021), 111528. <https://doi.org/10.1016/j.msec.2020.111528>
 27. Burgers, T. A., Mason, J., Niebur, G., Ploeg, H. L., "Compressive properties of trabecular bone in the distal femur", *Journal of Biomechanics*, Vol. 41, No. 5, (2008), 1077-1085. <https://doi.org/10.1016/j.jbiomech.2007.11.018>
 28. Wu, D., Spanou, A., Diez-Escudero, A., Persson, C., "3D-printed PLA/HA composite structures as synthetic trabecular bone: A feasibility study using fused deposition modeling", *Journal of the Mechanical Behavior of Biomedical Materials*, Vol. 103, (2020), 103608. <https://doi.org/10.1016/j.jmbbm.2019.103608>
 29. Karageorgiou, V., Kaplan, D., "Porosity of 3D biomaterial scaffolds and osteogenesis", *Biomaterials*, Vol. 26, No. 27, (2005), 5474-5491. <https://doi.org/10.1016/j.biomaterials.2005.02.002>
 30. Sainz, M. A., Pena, P., Serena, S., Caballero, A., "Influence of design on bioactivity of novel CaSiO₃-CaMg(SiO₃)₂ bioceramics: In vitro simulated body fluid test and thermodynamic simulation", *Acta Biomaterialia*, Vol. 6, No. 7, (2010), 2797-2807. <https://doi.org/10.1016/j.actbio.2010.01.003>
 31. Rhee, S. H., "Effect of calcium salt content in the poly(E-caprolactone)/silica nanocomposite on the nucleation and growth behavior of apatite layer", *Journal of Biomedical Materials Research Part A: An Official Journal of The Society for Biomaterials, The Japanese Society for Biomaterials, and The Australian Society for Biomaterials and The Korean Society for Biomaterials*, Vol. 67, No. 4, (2003), 1131-1138. <https://doi.org/10.1002/jbm.a.20054>
 32. Teixeira, S., Ferraz, M. P., Monteiro, F. J., "Biocompatibility of highly macroporous ceramic scaffolds: cell adhesion and morphology studies", *Journal of Materials Science: Materials in Medicine*, Vol. 19, No. 2, (2008), 855-859. <https://doi.org/10.1007/s10856-007-3005-x>
 33. Bose, S., Darsell, J., Hosick, H. L., Yang, L., Sarkar, D. K., Bandyopadhyay, A., "Processing and characterization of porous alumina scaffolds", *Journal of Materials Science: Materials in Medicine*, Vol. 13, No. 1, (2002), 23-28. <https://doi.org/10.1023/A:1013622216071>
 34. Gutiérrez-Prieto, S. J., Perdomo-Lara, S. J., Diaz-Peraza, J. M., Sequeda-Castañeda, L. G., "Analysis of in vitro osteoblast culture on scaffolds for future bone regeneration purposes in dentistry", *Advances in Pharmacological Sciences*, Vol. 2019, (2019), 5420752. <https://doi.org/10.1155/2019/5420752>
 35. Reddi, A. H., "Symbiosis of Biotechnology and Biomaterials: Applications in Tissue Engineering of Bone and Cartilage", *Journal of Cellular Biochemistry*, Vol. 56, No. 2, (1994), 192-195. <https://doi.org/10.1002/jcb.240560213>
 36. Chen, Q. Z., Efthymiou, A., Salih, V., Boccaccini, A. R., "Bioglass®-derived glass-ceramic scaffolds: study of cell proliferation and scaffold degradation in vitro", *Journal of Biomedical Materials Research Part A: An Official Journal of The Society for Biomaterials, The Japanese Society for Biomaterials, and The Australian Society for Biomaterials and The Korean Society for Biomaterials*, Vol. 84, No. 4, (2008), 1049-1060. <https://doi.org/10.1002/jbm.a.31512>
 37. Low, S. P., Williams, K. A., Canham, L. T., Voelcker, N. H., "Evaluation of mammalian cell adhesion on surface modified porous silicon", *Biomaterials*, Vol. 27, No. 26, (2006), 4538-4546. <https://doi.org/10.1016/j.biomaterials.2006.04.015>
 38. Lee, J., Kang, B. S., Hicks, B., Chancellor Jr., T. F., Chu, B. H., Wang, H. T., "The control of cell adhesion and viability by zinc oxide nanorods", *Biomaterials*, Vol. 29, No. 27, (2008), 3743-3749. <https://doi.org/10.1016/j.biomaterials.2008.05.029>

39. Chou, S. Y., Cheng, C. M., LeDuc, P. R., "Composite polymer systems with control of local substrate elasticity and their effect on cytoskeletal and morphological characteristics of adherent cells", *Biomaterials*, Vol. 30, No. 18, (2009), 3136-3142. <https://doi.org/10.1016/j.biomaterials.2009.02.037>
40. Wu, C., Ramaswamy, Y., Zhu, Y. F., Zheng, R., Appleyard, R., Howard, A., Zreiqat, H., "The effect of mesoporous bioactive glass on the physiochemical, biological and drug-release properties of poly (DL-lactide-co-glycolide) films", *Biomaterials*, Vol. 30, No. 12, (2009), 2199-2208. <https://doi.org/10.1016/j.biomaterials.2009.01.029>
41. Seeman, E., Devogelaer, J. P., Lorenc, R., Spector, T., Brixen, K., Balogh, A., Stucki, G., Reginster, J. Y., "Strontium ranelate reduces the risk of vertebral fractures in patients with osteopenia", *Journal of Bone and Mineral Research*, Vol. 23, No. 3, (2008), 433-438. <https://doi.org/10.1359/jbmr.071105>
42. Panzavolta, S., Torricelli, P., Sturba, L., Bracci, B., Giardino, R., Bigi, A., "Setting properties and in vitro bioactivity of strontium-enriched gelatin-calcium phosphate bone cements", *Journal of Biomedical Materials Research Part A: An Official Journal of The Society for Biomaterials, The Japanese Society for Biomaterials, and The Australian Society for Biomaterials and the Korean Society for Biomaterials*, Vol. 84, No. 4, (2008), 965-972. <https://doi.org/10.1002/jbm.a.31412>
43. Pietak, A. M., Reid, J. W., Stott, M. J., Sayer, M., "Silicon substitution in the calcium phosphate bioceramics", *Biomaterials*, Vol. 28, No. 28, (2007), 4023-4032. <https://doi.org/10.1016/j.biomaterials.2007.05.003>
44. Phan, P. V., Grzanna, M., Chu, J., Polotsky, A., El-Ghannam, A., Van Heerden, D., Hungerford, D. S., Frondoza, C. G., "The effect of silica-containing calcium-phosphate particles on human osteoblasts In vitro", *Journal of Biomedical Materials Research Part A: An Official Journal of The Society for Biomaterials, The Japanese Society for Biomaterials, and The Australian Society for Biomaterials and the Korean Society for Biomaterials*, Vol. 67, No. 3, (2003), 1001-1008. <https://doi.org/10.1002/jbm.a.10162>
45. Buehler, J., Chappuis, P., Saffar, J. L., Tsouderos, Y., Vignery, A., "Strontium ranelate inhibits bone resorption while maintaining bone formation in alveolar bone in monkeys (*Macaca fascicularis*)", *Bone*, Vol. 29, No. 2, (2001), 176-179. [https://doi.org/10.1016/S8756-3282\(01\)00484-7](https://doi.org/10.1016/S8756-3282(01)00484-7)



Materials and Energy Research Center

MERC

Contents lists available at [ACERP](#)

Advanced Ceramics Progress

Journal Homepage: www.acerp.ir

Advanced Ceramics Progress

Original Research Article

Multi-Walled Carbon Nanotubes (MWCNTs) Synthesized on Ni-Cu NPs @ a-C: H Films: A Study of Cavity and Bearing Areas Percentage, ZX Topography, and the Width of the Surface Height Distribution with Different Ni Layers' Thickness

V. Dalouji ^{a,*}, S. Goudarzi ^b, N. Rahimi ^b, A. R. Souri ^c^a Associate Professor, Department of Physics, Faculty of Science, Malayer University, Malayer, Hamadan, Iran^b PhD Student, Department of Physics, Faculty of Science, Malayer University, Malayer, Hamadan, Iran^c Assistant Professor, Department of Materials Engineering, Faculty of Engineering, Malayer University, Malayer, Hamadan, Iran* Corresponding Author Email: dalouji@yahoo.com (V. Dolouji)URL: https://www.acerp.ir/article_144166.html

ARTICLE INFO

ABSTRACT

Article History:

Received 13 December 2021

Received in revised form 15 January 2022

Accepted 01 February 2022

Keywords:

Topography
Bearing Area
Nanotubes Lateral Size
Fractal Dimensions
Optical Density

Topological characterizations and optical density of the synthesized hydrogenated amorphous carbon Cu-Ni NPs @ a-C: H nanotubes (CNTs) with different surface morphology were studied in this report. Films deposited with Ni layer thickness of 5 nm have a maximum value of optical density especially, in the high energy range. Steps between 1800 to 2000 KeV in the Rutherford backscattering (RBS) spectra correspond to the presence of Cu and Ni elements. The thicknesses of films were measured by using SIMN-RA software. Films deposited with Ni layer thickness of 15 nm have a maximum value of the lateral size of nanotubes in about 19.7 nm. The grown CNTs of films deposited with Ni layer thickness 15 nm Ni, has a maximum value of diameter in about 16.2 nm. The diagram of bearing area proportion height shows the percentage of cavities and single-layers. The cavity coverage of films was less than 5 % and the layer content of films was about 90 %.

<https://doi.org/10.30501/ACP.2022.318678.1077>

1. INTRODUCTION

The study of physical properties of metallic nanoparticles in dielectric host medium has been the subject of extensive research due to their unique applications in many areas such as nonlinear optical switching, immunoassay labeling, and Raman spectroscopy enhancement [1,2]. Especially copper-

nickel nanoparticles have received significant attention due to their potential applications in optical magnetic recording, spintronics, data storage devices, and used as giant magnetic resistance (GMR) [3]. Cu-Ni nanoparticles have been also used as catalysts for the synthesis of dimethyl carbonate and carbon nanotubes [4-6]. Multilayers with a thickness of two layers less than 100 nm that are inaccessible in bulk have very

Please cite this article as: Dalouji, V., Goudarzi, S., Rahimi, N., Souri, A. R., "Multi-Walled Carbon Nanotubes (MWCNTs) Synthesized on Ni-Cu NPs @ a-C: H Films: A Study of Cavity and Bearing Areas Percentage, ZX Topography, and the Width of the Surface Height Distribution with Different Ni Layers' Thickness", *Advanced Ceramics Progress*, Vol. 7, No. 4, (2021), 20-26. <https://doi.org/10.30501/ACP.2022.318678.1077>

2423-7485/© 2021 The Author(s). Published by MERC.

This is an open access article under the CC BY license (<https://creativecommons.org/licenses/by/4.0/>).

interesting properties due to their magnetic properties and improvement of their mechanical properties [7]. Although the study of the surface structure and interface at the atomic scale of such layers is a very difficult task in surface science the results which are obtained from these studies are very important. Plasma arc evaporation [8] and sol-gel methods [9] were used to make copper-nickel alloy nanoparticles. Amorphous carbon metals have many applications as coatings in optical, electronic, mechanical, and biomedical applications [6-9]. Since the discovery of carbon nanotubes, there has been a great deal of interest in synthesizing the growth of directed nanotubes [10]. The reason for the interest in nanotubes is due to their excellent physical properties such as high mechanical strength, high dimensional ratio, and good thermal conductivity [11,12]. In recent years, there have been extensive publications to prove the growth of both random and homogeneous nanotubes [13-16]. However, for applications where nanotubes act as electrical conductors, the growth of directional carbon nanotubes is preferred. Normally, nanotubes grow in a manner such as chemical vapor deposition (CVD) on metal catalyst particles or islands located on top of a semiconductor or insulating substrate. However, for many of the predicted programs, it is best to grow the nanotubes directly on a conventional copper-like substrate to provide good power. Since copper itself is not a suitable catalyst for the growth of carbon nanotubes, the technique discussed here uses nickel-transfer metal as a catalyst in copper substrates. Esconjauregu et al. have reported that among metals Ni, Fe, Co, and their alloys act as the best catalyst for direct growth of carbon nanotubes [17-19]. Nickel was selected as a catalyst due to its superior properties for achieving directional carbon nanotube growth [20-23]. CNT growth is difficult on bulk copper unless it is in the form of nanoparticles or several layers of metal catalysts are stored in it. In this work, the effect of different Ni layers' thickness was studied on optical density, surface topography, and the fractal dimensions of films.

2. EXPERIMENTAL DETAILS

More details of the sputtering deposition process were given in references [3-5]. The scheme of co-deposition by RF-Sputtering and RPECVD techniques is shown in Figure 1. Cu-Ni NPs @ a-C: H with different thicknesses of Ni overlayer is provided by a capacitance coupled radio frequency plasma enhanced chemical vapor deposition (RF-PECVD) system with a 13.56 MHz power supply. The reactor is composed of two electrodes with different area sizes. The electrode smaller was Cu and Ni targets at the first and the second stages of deposition. Another electrode was placed in

the body of the stainless-steel chamber. All deposition was performed at room temperature on this electrode over the glass and silicon substrates. The chamber was vacuumed to a base pressure of 10^{-5} mbar before to the deposition then the pressure was increased to ambient pressure by acetylene gas. The RF power 200 W and initial gas pressure were at different pressures from 0.01 mbar to 0.05 mbar. The copper deposition time was 20 minutes. After the deposition of copper, the electrode was changed to Ni, and sputtering was done for 2 min with RF power of 250 W and acetylene initial pressure of 0.025 mbar. To obtain chemical compounds and the thickness of the prepared thin films, the RBS spectra were obtained using a helium ion beam with energy of about 2 MeV. The thickness of the films and the atomic content of the films were obtained from RBS data by SIMN-RA software simulation and the thicknesses of films were kept constant and were measured from RBS spectra. In order to study the surface topography of the thin films and the average nanotube's size atomic force microscopy (AFM) analysis in the noncontact mode was used. By using of a double beam UV-Vis spectrometer, the optical densities of films were measured. The Thermal Chemical Vapor Deposition (TCVD) system includes a furnace, a quartz tube of 60 cm length and 40 mm inner diameter, a temperature controller with a thermocouple. The LP gas (LPG) with a flow of 80 sccm and at 825 °C was applied to the reactor. The composition of PLG was measured by a gas chromatograph (Hewlett Packard, Palo Alto, CA, USA) and it was a mixture of C3 (54 %), C4 (45 %), and C5 (1 %).

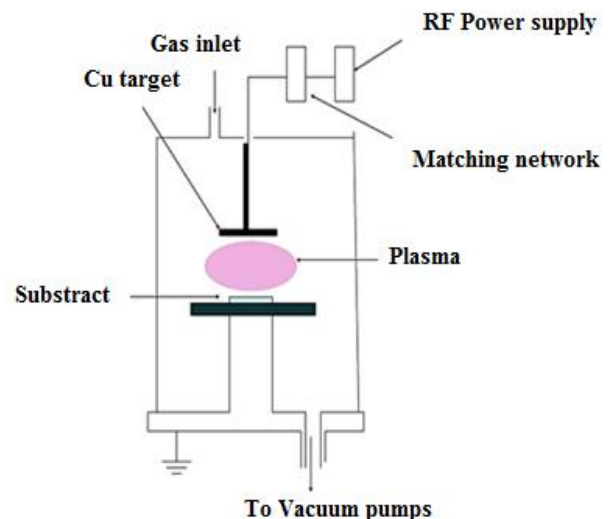


Figure 1. (Color online) The scheme of co-deposition by RF-Sputtering and RPECVD setup [4]

3. RESULTS AND DISCUSSION

To obtain the optical density of films Equation (1) was used [24,25]:

$$D_{opt} = 2.303 A \quad (1)$$

Here A is the absorbance of the films. Figure 2 shows the optical density of the films with various thicknesses of Ni layers. As it is clear the optical density for films is constant between 1 and 3 eV, and then increases with a relatively slow slope. The optical density of films containing Ni with a thickness of about 5 nm has a maximum value. However, the sizes of nanotubes show very significant changes with photon energy for Ni films with a layer thickness of 15 nm [26].

From RBS spectra (It has been reported in previous works [27]) it is possible to find out Cu, Ni, C, and O contents of the samples. In RBS spectra, steps at 1550 and 1700 KeV could be respectively due to O and Si nuclei of the amorphous SiO₂ substrate. Peaks at 1400 KeV and in the range 1800 to 1900 KeV were attributed to C, Cu, and Ni nuclei, respectively. The peak between 1800 and 1900 KeV is considered a convoluted peak. Their results of SIMN-RA software simulation of RBS spectra indicate that the Cu layer contains 40 % Cu, 55 % C, and 5 % O, and its thickness is about 100 nm. This is common among all prepared samples. The composition of Ni layers was obtained 80 % Ni, 10 % C, and 10 % O, and the thicknesses of these over layers for the samples with 2.7- and 10-min deposition were obtained 5, 10, and 15 nm, respectively. It is clearly observable that the intensity of RBS spectra was increased by the increase of the thickness of Ni layers.

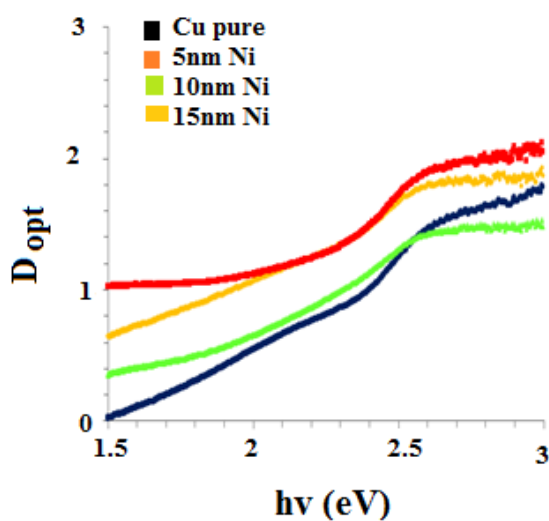
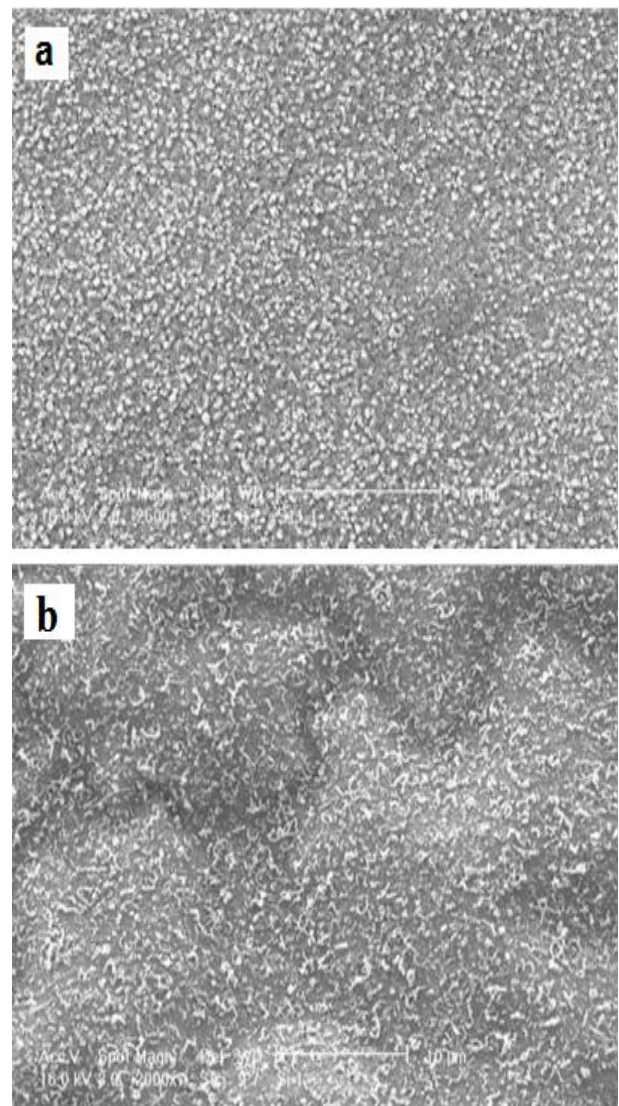


Figure 2. Optical density of films for Cu pure, Ni layer thickness 5 nm, 10 nm, and 15 nm

The SEM images of films with and without Ni for layers with 5, 10, and 15 nm thicknesses are shown in Figure 3(a-d), respectively. As it is clear by adding Ni the density of the CNTs is greatly enhanced. Furthermore, the average diameter of the grown CNTs depends on the Ni content and increases by increasing Ni content. The average diameter of the grown CNTs on films for Ni layers of thickness 5, 10, and 15 nm Ni are obtained about 10.3, 12.5, and 16.2 nm, respectively. As it is clear from Fig. 3(d) which shows the SEM image of films with 15 nm thickness, MWCNTs are formed on the films, shorter nanotubes are formed and the quality and height of these nanotubes in the third sample are higher than the other samples.

The surface morphology and the average nanoparticle size of films were obtained by AFM in non-contact mode and the results are shown in Figure 4. The nanotubes lateral size of the thin films can be estimated using AFM images. The variations of nanotubes lateral sizes of films surfaces versus different the Ni layer



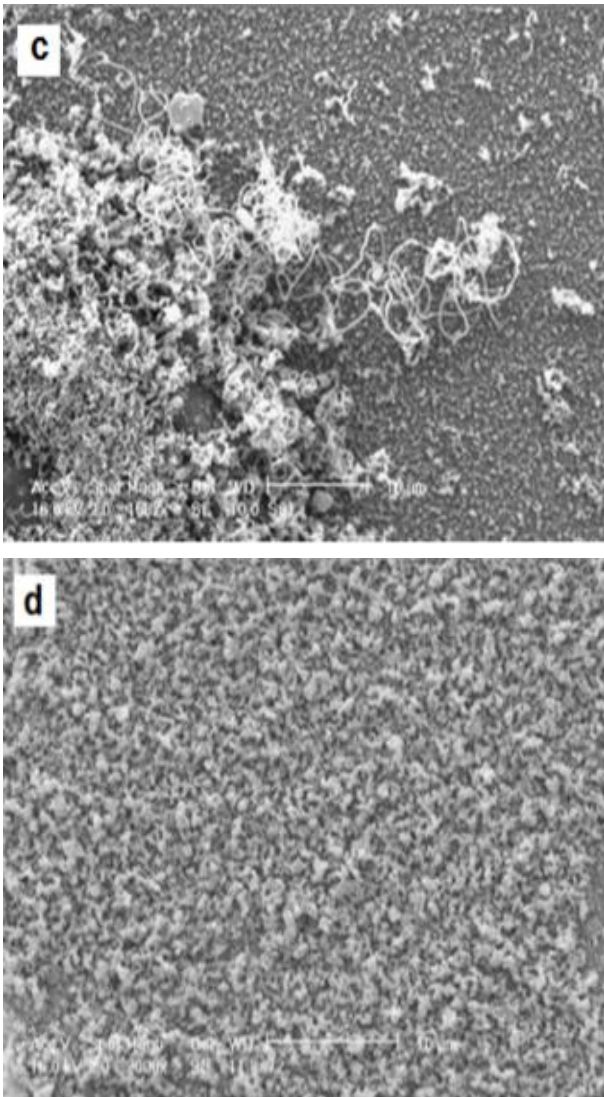


Figure 3. SEM images of films for different Ni layer thickness (a) Cu pure, (b) Ni-5 nm, (c) Ni-10 nm, and (d) Ni-15 nm

thicknesses for different deposited films, Cu pure layer, Ni-5 nm, Ni-10 nm, and Ni-15 nm were about 12, 14.4, 13.2, and 19.7 nm for films, respectively (Figure 5). The films deposited with a layer of Ni with a thickness of 15 nm have maximum nanotubes lateral size, however, Cu pure layer has a minimum of nanotubes lateral size. The AFM images show that the nanotubes synthesized on the substrates, firstly, have a uniform distribution that is distributed throughout the substrates, and secondly, at the measuring scale, the mean diameter values of the measured nanotubes also appear to be almost identical. It was found that the size of nanotubes on films surfaces was increased with the increasing of the Ni thickness of the Ni layer from 5 nm, then it was decreased up to 10 nm and from 10 to 15 nm it was increased. The nanotube's size changes as Gaussian plots, which can

almost be due to little changes in the size of the nanotubes with the change in thickness of the Ni layers. The AFM images for similar substrates were reported earlier [28]. By comparing SEM and AFM images we find that both are compatible with each other. It can be seen that in the pictures, CNTs have different diameters and in general the average diameter of grown carbon nanotubes increases with increasing thickness of nickel layers.

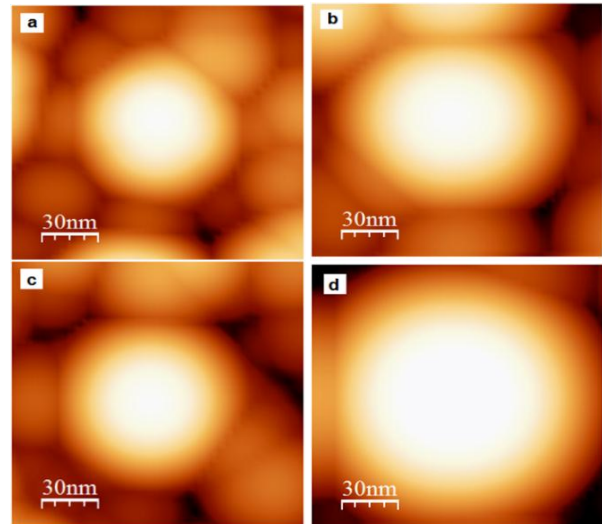


Figure 4. AFM images of films for different Ni layer thickness (a) Cu pure, (b) Ni-5 nm, (c) Ni-10 nm, and (d) Ni-15 nm

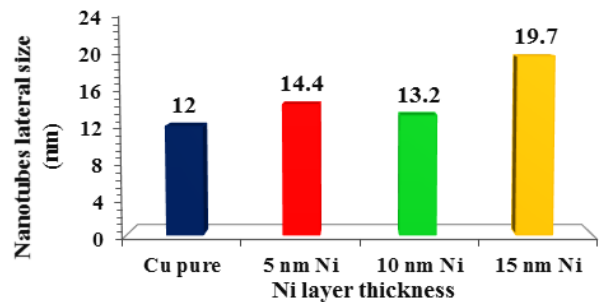


Figure 5. The variations of nanotubes lateral size of nanoparticles on the surface of films for Cu pure, Ni-5 nm, Ni-10 nm, and Ni-15 nm

Figure 6 (a-d) shows the variations in the height of the thin films on the surface versus the x and z axes for films without Ni thin layer and with layer containing Ni layer of thicknesses 5, 10, and 15 nm, respectively. The scanning size on the surface of the films for the AFM study was chosen as much as $1 \mu\text{m} \times 1 \mu\text{m}$ (the maximum scale value on the x-axis was as much as $1 \mu\text{m}$). The height's changes on the surface of the scanned films show that the films have a topological phase-change films. In the deposited films, the z values

were about 13 nm for the thin layer containing Ni thickness layer 5 nm, Ni thickness layer 10 nm, Cu pure, and about 17 nm for Ni thickness layer 15 nm. These results show that the films are smooth in this state and showed a second phase change. The films without

Ni thin films have lower fluctuations, and the peaks have a slower slope than other thin layers containing Ni thickness layer. The z variations versus x variations are closely related to both Cu and Ni materials, which have many peaks.

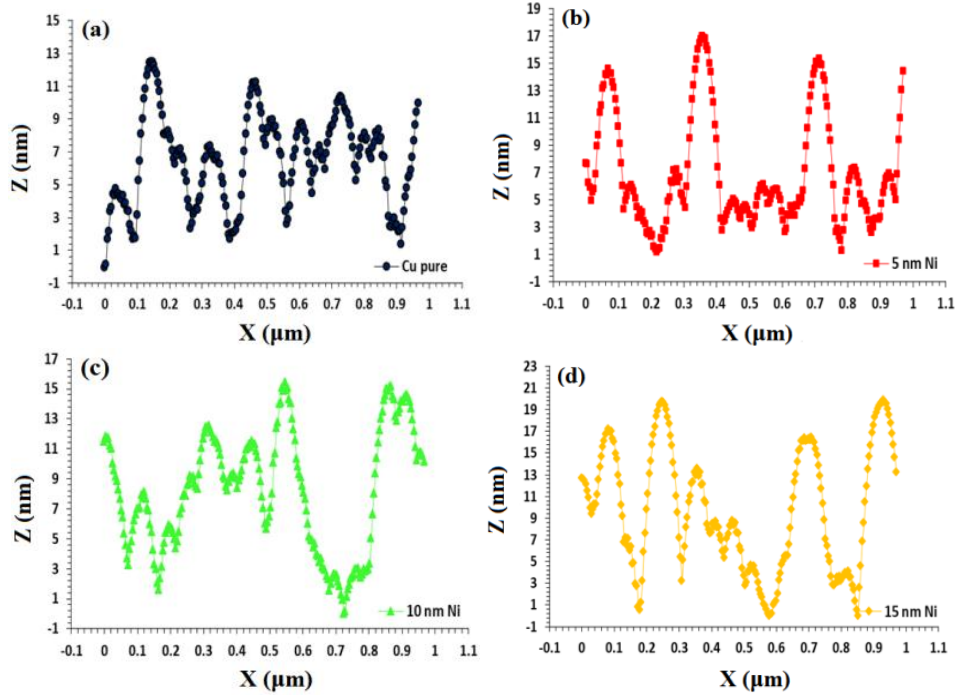


Figure 6. Z-height variations of nanoparticles on the surface of films versus x-axis of the films for different Ni thickness layer (a) Cu pure (b) Ni-5 nm, (c) Ni-10 nm, and (d) Ni-15 nm

The PSD spectra were extracted from the scanned area and 30 nm obtained from AFM images of the films as shown in Figure 4. It can be seen that all the PSD points include a high spatial frequency region. According to the Dynamic Scaling Theory (DST), the power spectral densities (PSDs) analyses closely show how the roughness varies with length scale. The AFM images can be divided into pixels as a small square area where the vectors $h(x_i)$ and $h(y_j)$ are the height at (x_i, y_j) positions. Then, the one-dimensional average of the power spectral densities (PSDs) is given as follows:

$$P(k) \propto \frac{2L}{N} \left[\left\langle \sum_{i=1}^{\frac{N}{2}} \left(\text{FFT}(h(x_i))^2 \right) \right\rangle_y + \left\langle \sum_{i=1}^{\frac{N}{2}} \left(\text{FFT}(h(y_i))^2 \right) \right\rangle_x \right] \quad (2)$$

Where FFT is the Fast Fourier Transform between the real and reciprocal spaces.

According to the dynamical scaling theory, the relation $P(k)$ and frequency k are given below for a system with lateral size L [29]:

$$P(k) \propto k^{-\beta} \quad (3)$$

Here β is calculated from the slope of the log-log in PSD spectra of high spatial frequency. The fractal dimensions D_f of films are obtained by solving the β slope of the log-log graph [28]:

$$D_f = 4 + \beta/2 \quad (4)$$

Figure 7 (a-d) show the variations of spectral density with a spatial frequency of films for: (a) pure Cu and Ni layers with thicknesses (b) 5 nm, (c) 10 nm, and (d) 15 nm. Especially in the high spatial frequency region, the spectral compaction power of all films reflects the attendance of fractal components in outstanding topographies. From these values, one can determine the relative amounts of surface disorder at various distance scales. As the thicknesses of Ni layers were increased, the performance of the spectral compaction power increases as a result of decreasing the size of the nanotubes. The Ni layer with 15 nm thickness and the pure Cu layers have maximum and minimum values of the fractal dimensions, respectively.

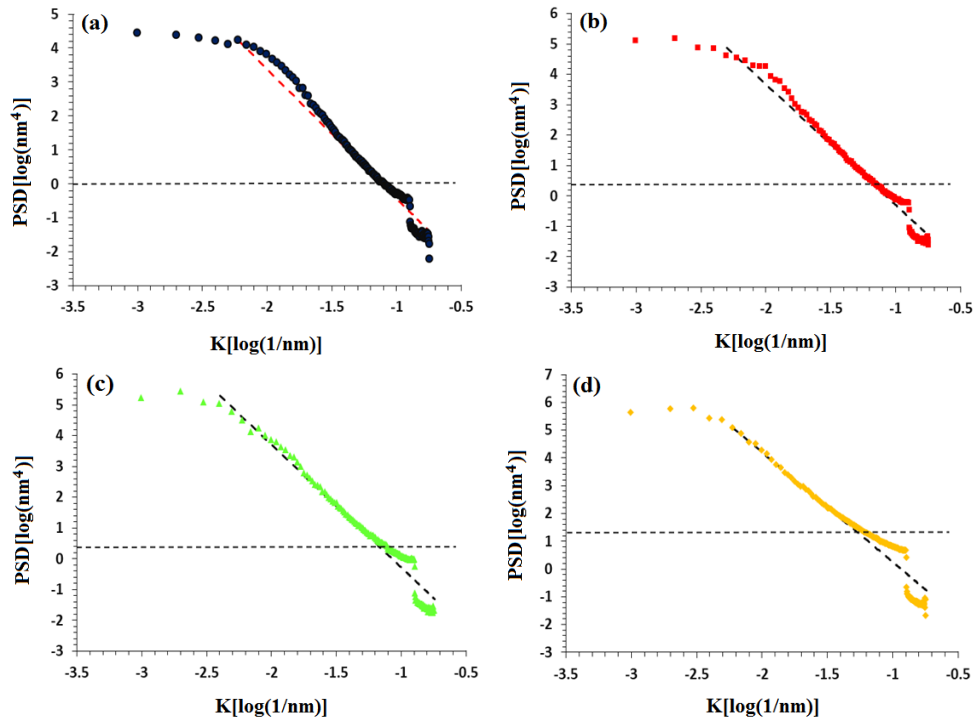


Figure 7. The variations of power spectral density of the films versus frequency k of films for different Ni layer thickness (a) Cu pure, (b) Ni-5 nm, (c) Ni-10 nm, and (d) Ni-15 nm

Figure 8 shows illustrate the variations of fractal dimensions versus of Ni layer thickness. The fractal dimensions of films for pure Cu films and Ni layers with thicknesses 5, 10, and 15 nm were estimated to be 2.92, 2.98, 2.95, and 2.93 nm, respectively. Therefore, the fractal dimensions of films increase with the increase of the Ni thickness layer up to 5 nm, and then, it was decreased over 5 nm.

Figure 9 shows the variations of bearing area of the films in respect to Ni layer thickness for Ni layers of thickness 5 nm, 10 nm, and 15 nm. The area shows the tolerance for height. In fact, it indicates the amount of

vacuum, zero coverage (cavity, bottom curvature of the diagram), monolayer (upper curvature of the diagram), and isolation (between the cavity and monolayer) of the layers. The films in Cu pure, Ni thickness layer 5 nm, Ni thickness layer 10 nm have cavity coverage of less than 5 % and layer content of about 90 % and 95 % which are monolayer height. In the vacuum, Ni thickness layer is 15 nm, the coating is 10 %, and the content of the film is about 90 %, 80 % of which is isolated. Thickness did not have much effect on the degree of isolation, so all four diagrams have similar results.

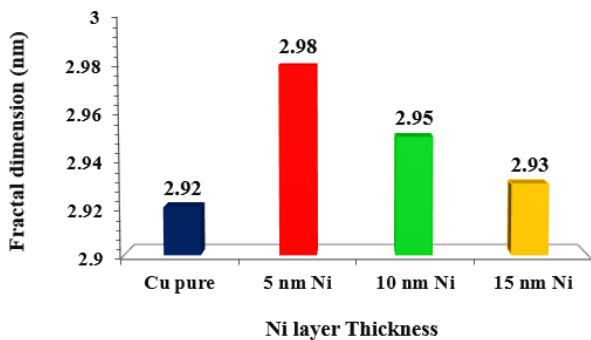


Figure 8. The variations of fractal dimensions of films for Cu pure, Ni-5 nm, Ni-10 nm, and Ni-15 nm

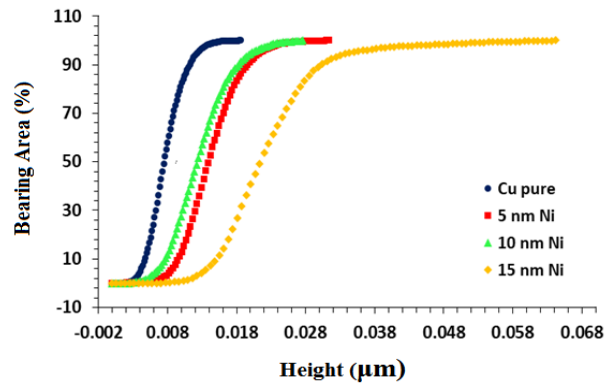


Figure 9. The bearing areas of films for Cu pure, Ni-5 nm, Ni-10 nm, and Ni-15 nm

4. CONCLUSION

In this article, we show that films have an important effect on the growth of MWCNTs based on Ni NPs catalyst. The optical density of films with a layer of Ni and thickness of 5 nm has the maximum value. The optical density and the average diameters of the grown CNTs increase with increasing Ni layer thickness. The average diameter of CNTs of films with a 15 nm layer of Ni is 17 nm. The AFM images show that the nanotubes synthesized on the substrates both have a uniform distribution and the mean diameter values of the measured nanotubes also appear to be almost identical. We found that the fractal dimensions of films were decreased with the increase of the thickness of the Ni layer. Thickness did not have much effect on the degree of isolation, so all four diagrams have similar results.

ACKNOWLEDGEMENTS

The authors would like to acknowledge the financial support of Malayer University for this research.

REFERENCES

- Li, X., Lv, M., Tian, Y., Gao, L., Liu, T., Zhou, Q., Xu, Y., Shen, L., Shi, W., Li, X., Lu, Y., "Negatively charged polymeric interphase for regulated uniform lithium-ion transport in stable lithium metal batteries", *Nano Energy*, Vol. 87, (2021), 106214. <https://doi.org/10.1016/j.nanoen.2021.106214>
- Genov, D. A., Seal, K., Sarychev, A. K., Noh, H., Shalae, V. M., Ying, Z. C., Zhang, X., Cao, H., "Surface plasmon delocalization by short-range correlations in percolating metal systems", *Applied Physics B*, Vol. 84, No. 1, (2006), 205-210. <http://doi.org/10.1007/s00340-006-2229-7>
- Singh, S., Basu, S., Ghosh, S. K., "Structure and morphology of Cu/Ni film grown by electrodeposition method: A study of neutron reflectivity and AFM", *Applied Surface Science*, Vol. 255, No. 11, (2009), 5910-5916. <https://doi.org/10.1016/j.apsusc.2009.01.030>
- Zhou, Y., Wang, S., Xiao, M., Han, D., Lu, Y., Meng, Y., "Formation of dimethyl carbonate on nature clay supported bimetallic copper-nickel catalysts", *Journal of Cleaner Production*, Vol. 103, (2015), 925-933. <https://doi.org/10.1016/j.jclepro.2014.08.075>
- Bian, J., Xiao, M., Wang, S. J., Lu, Y. X., Meng, Y. Z., "Graphite oxide as a novel host material of catalytically active Cu-Ni bimetallic nanoparticles", *Catalysis Communications*, Vol. 10, No. 11, (2009), 1529-1533. <https://doi.org/10.1016/j.catcom.2009.04.009>
- Zhang, M., Yang, K., Zhang, X., Yu, Y., "Effect of Ni (111) surface alloying by Pt on partial oxidation of methane to syngas: A DFT study", *Surface Science*, Vol. 630, (2014), 236-243. <https://doi.org/10.1016/j.susc.2014.08.023>
- Tokarz, A., Fraczek, T., Balaga, Z., Nitkiewicz, Z., "Structure, hardness and thermal stability of electrodeposited Cu/Ni nanostructured multilayers", *Reviews on Advanced Materials Science*, Vol. 15, No. 3, (2007), 247-252. https://www.ipme.ru/e-journals/RAMS/no_31507/tokarz.pdf
- Liu, H. D., Yang, B., Mao, M. R., Liu, Y., Chen, Y. M., Cai, Y., Fu, D. J., Ren, F., Wan, Q., Hu, X. J., "Enhanced thermal stability of solar selective absorber based on nano-multilayered TiAlON films deposited by cathodic arc evaporation", *Applied Surface Science*, Vol. 501, (2020), 144025. <https://doi.org/10.1016/j.apsusc.2019.144025>
- Phin, H. Y., Ong, Y. T., Sin, J. C., "Effect of carbon nanotubes loading on the photocatalytic activity of zinc oxide/carbon nanotubes photocatalyst synthesized via a modified sol-gel method", *Journal of Environmental Chemical Engineering*, Vol. 8, No. 3, (2020), 103222. <https://doi.org/10.1016/j.jece.2019.103222>
- Ajayan, P. M., Ebbesen, T. W., Ichihashi, T., Iijima, S., Tanigaki, K., Hiura, H., "Opening carbon nanotubes with oxygen and implications for filling", *Nature*, Vol. 362, No. 6420, (1993), 522-525. <https://doi.org/10.1038/362522a0>
- Harris, P. J., Hernández, E., Yakobson, B. I., "Carbon Nanotubes and Related Structures: New Materials for the Twenty-First Century", *American Journal of Physics*, Vol. 72, No. 3, (2004), 415-415. <https://doi.org/10.1119/1.1645289>
- Dresselhaus, M. S., Dresselhaus, G., Eklund, P. C., *Science of Fullerenes and Carbon Nanotubes: Their Properties and Applications*, Elsevier, (1996). <https://doi.org/10.1016/B978-0-12-221820-0.X5000-X>
- Ebbesen, T. W., Ajayan, P. M., Hiura, H., Tanigaki, K., "Purification of nanotubes", *Nature*, Vol. 367, No. 6463, (1994), 519-519. <https://doi.org/10.1038/367519a0>
- Ren, Z., Lan, Y., Wang, Y., "Technologies to Achieve Carbon Nanotube Alignment", In *Aligned Carbon Nanotubes*, Springer, Berlin, Heidelberg, (2012), 111-156. https://doi.org/10.1007/978-3-642-30490-3_6
- Dhore, V. G., Rathod, W. S., Patil, K. N., "Synthesis and characterization of high yield multiwalled carbon nanotubes by ternary catalyst", *Materials Today: Proceedings*, Vol. 5, No. 2, (2018), 3432-3437. <https://doi.org/10.1016/j.matpr.2017.11.589>
- Li, M., Liu, X., Zhao, X., Yang, F., Wang, X., Li, Y., "Metallic catalysts for structure-controlled growth of single-walled carbon nanotubes", *Single-Walled Carbon Nanotubes*, (2019), 25-67. <https://doi.org/10.1007/s41061-017-0116-9>
- Esconjauregui, S., Whelan, C. M., Maex, K., "The reasons why metals catalyze the nucleation and growth of carbon nanotubes and other carbon nanomorphologies", *Carbon*, Vol. 47, No. 3, (2009), 659-669. <https://doi.org/10.1016/j.carbon.2008.10.047>
- Li, Y. S., Hirose, A., "Controlled synthesis of diamond and carbon nanotubes on Ni-base alloy", *Applied Surface Science*, Vol. 255, No. 5, (2008), 2251-2255. <https://doi.org/10.1016/j.apsusc.2008.07.076>
- Gao, L., Peng, A., Wang, Z. Y., Zhang, H., Shi, Z., Gu, Z., Cao, G., Ding, B., "Growth of aligned carbon nanotube arrays on metallic substrate and its application to supercapacitors", *Solid State Communications*, Vol. 146, No. 9-10, (2008), 380-383. <https://doi.org/10.1016/j.ssc.2008.03.034>
- Bonnet, F., Ropital, F., Berthier, Y., Marcus, P., "Filamentous carbon formation caused by catalytic metal particles from iron oxide", *Materials and Corrosion*, Vol. 54, No. 11, (2003), 870-880. <https://doi.org/10.1002/maco.200303742>
- Guevara, L., Wanner, C., Welsh, R., Atwater, M. A., "Using mechanical alloying to create bimetallic catalysts for vapor-phase carbon nanofiber synthesis", *Fibers*, Vol. 3, No. 4, (2015), 394-410. <https://doi.org/10.3390/fib3040394>
- Kharlamova, M. V., "Investigation of growth dynamics of carbon nanotubes", *Beilstein Journal of Nanotechnology*, Vol. 8, No. 1, (2017), 826-856. <https://doi.org/10.3762/bjnano.8.85>
- Kharlamova, M. V., Eder, D., "Carbon nanotubes: Synthesis, properties, and new developments in research", *Synthesis and Applications of Nanocarbons*, (2020), 107-147. <https://doi.org/10.1002/9781119429418.ch4>
- Hassanien, A. S., Akl, A. A., "Effect of Se addition on optical and electrical properties of chalcogenide CdSSe thin films", *Superlattices and Microstructures*, Vol. 89, (2016), 153-169. <https://doi.org/10.1016/j.spmi.2015.10.044>
- Dalouji, V., Goudarzi, S., Solaymani, S., "The optical density and topography characterizations of MWCNTs on Ni-Cu/a-C: H

- substrates with different copper percentage”, *Microscopy Research and Technique*, Vol. 84, No. 6, (2021), 1205-1211. <https://doi.org/10.1002/jemt.23679>
26. Dejam, L., Solaymani, S., Achour, A., Stach, S., Țălu, Ș., Nezafat, N. B., Dalouji, V., Shokri, A. A., Ghaderi, A., “Correlation between surface topography, optical band gaps and crystalline properties of engineered AZO and CAZO thin films”, *Chemical Physics Letters*, Vol. 719, (2019), 78-90. <https://doi.org/10.1016/j.cplett.2019.01.042>
27. Dalouji, V., Rahimi, N., Goudarzi, S., Solaymani, S., “MWCNTs synthesized on Ni Cu NPs @ aC: H films: study of the dielectric relaxation time, the free carriers concentration and the dissipation factor with different Ni layers thickness”, *Optical and Quantum Electronics*, Vol. 53, No. 11, 648, (2021), 1-13. <https://doi.org/10.1007/s11082-021-03289-w>
28. Hedayati, K., “Structural and magnetic characterization of electrodeposited Ni–Cu/Cu and Fe–Ni–Cu/Cu multilayer”, *Applied Physics A*, Vol. 118, No. 3, (2015), 975-979. <https://doi.org/10.1007/s00339-014-8851-z>
29. Rahimi, N., Dalouji, V., Souri, A., “Studying the optical density, topography, and structural properties of CZO and CAZO thin films at different annealing temperatures”, *Advanced Ceramics Progress*, Vol. 6, No. 2, (2020), 17-23. <https://doi.org/10.30501/acp.2020.107466>



Materials and Energy Research Center
MERC

Contents lists available at [ACERP](#)

Advanced Ceramics Progress

Journal Homepage: www.acerp.ir



Original Research Article

Modelling and Optimization of Densification and Hardness of Cu/SiC Nanocomposites based on Response Surface Methodology (RSM)

M. R. Akbarpour ^{a,*}, F. S. Torknik ^b

^a Associate Professor, Department of Materials Engineering, Faculty of Engineering, University of Maragheh, Maragheh, East Azerbaijan, Iran

^b PhD, Department of Semiconductors, Materials and Energy Research Center (MERC), Meshkindasht, Alborz, Iran

* Corresponding Author Email: mreza.akbarpour@gmail.com (M. R. Akbarpour)

URL: https://www.acerp.ir/article_144396.html

ARTICLE INFO

Article History:

Received 18 January 2022
Received in revised form 01 February 2022
Accepted 06 February 2022

Keywords:

Copper
SiC
Composites
Powder Metallurgy
Response Surface Methodology

ABSTRACT

Nowadays, Response Surface Methodology (RSM) is widely used for modelling and optimizing the performance of manufacturing technologies. Obtaining the optimum process parameters based on powder metallurgy methods is of great concern in manufacturing. In this paper, appropriate milling time for fabrication of Cu/SiC nanocomposites was determined to maximize the densification and hardness of the nanocomposite samples. The samples were prepared by high-energy planetary ball milling of the powders and conventional uniaxial pressing and sintering method. Microstructural characterization was carried out using scanning electron microscopy and optical microscopy, and the hardness of the samples was measured through Vickers microhardness tester. The highest hardness of 170 HV and minimum densification of 0.74 were obtained for the sample milled for 25 h. In addition, the effects of milling time on the hardness and density of the sintered samples were evaluated using one-factor RSM. Polynomial mathematical models were successfully developed to determine the relative density and microhardness of the sintered samples. The analysis of variance confirmed that the suggested models could be satisfactorily employed to predict the relative density and microhardness.



<https://doi.org/10.30501/ACP.2022.325167.1080>

1. INTRODUCTION

Composites are increasingly used to improve the performance of electrodes and heat exchangers [1–3]. In the past few years, copper-based Metal-Matrix Composites (MMCs) have received considerable attention in the manufacturing sector. Several key factors make copper-based metal matrix composites essential materials including their low density, improved fatigue resistance, high corrosion resistance, and higher specific strength [4,5]. Among the copper-based composites, Cu/SiC composites have numerous

industrial applications that help overcome the challenges of thermal management, electrical contact materials in relays, contactors, switches, circuit breaks, and electrical brushes in rotation or sliding devices in the rapidly increasing power of advanced electronics. Generally, SiC as a reinforcing agent can improve the strength of the copper matrix [3]. Cu/SiC composites combine the superior ductility and toughness of copper with the high strength, modulus, and thermal conductivity of SiC reinforcement. Different solid-state and casting methods were used to produce Cu/SiC composites. Mechanical milling and sintering is a

Please cite this article as: Akbarpour, M. R., Torknik, F. S., "Modelling and Optimization of Densification and Hardness of Cu/SiC Nanocomposites based on Response Surface Methodology (RSM)", *Advanced Ceramics Progress*, Vol. 7, No. 4, (2021), 28-35. <https://doi.org/10.30501/ACP.2022.325167.1080>

2423-7485/© 2021 The Author(s). Published by MERC.

This is an open access article under the CC BY license (<https://creativecommons.org/licenses/by/4.0/>).



method used for composite production that has been extensively studied in the literature [2,3,6]. This method is able to evenly distribute SiC micro/nanoparticles and maintain the fine-grained structure of the matrix phase. G. Celebi Efe et al. evaluated the effects of the particle size and sintering temperature of SiC on the properties of Cu/SiC composites [7,8]. They found that the electrical conductivity of the composites containing SiC with the particle size of five μm was better than that of Cu/SiC composites containing SiC with the particle size of one μm . M. R. Akbarpour et al. [3,9] studied the effects of nano/micro SiC on the properties of Cu/SiC composites and obtained improved mechanical properties by adding optimum SiC vol. %. In addition, application of the hybrid-sized (micro and nano) SiC resulted in higher wear resistance, lower friction coefficient, and more compressive strength than those of micro composites. Some principles for Cu/SiC composites were obtained based on the previous researches [6,10,11]: (1) nanosize SiC particles were more effective in strengthening than the micro-sized ones; (2) coating of SiC with Ni, Cu, etc. would improve the interfacial bonding between Cu and SiC, hence improvement of its thermal, electrical, and mechanical properties [12]; and (3) an optimum SiC content was required to achieve physical/mechanical properties [11]. Cost reduction during production and operation is the main technological parameter to be taken into account in the advancement of all materials. One of the main parameters that affect the composite properties and production costs is milling time. During milling of Cu/SiC powder, the powder morphology and hardness changed, thus affecting the composite densification and properties [13]. Identification of the relationships among the milling time variable, densification, and microhardness of Cu/SiC nanocomposites produced by high-energy ball milling and conventional sintering process is of high significance. In this study, copper metal reinforced with SiC nanoparticles was mechanically milled at different times. The milled samples were sintered and then, their density and hardness were measured. The obtained results were used to model the effect of milling time on density and hardness of Cu/SiC nanocomposite based on the RSM method.

2. MATERIALS AND METHODS

In this study, Cu and SiC nanoparticles were used to fabricate Cu/SiC composites. The copper powder was characterized by a purity of 99.7 % and particle size of less than 20 μm (Merck Co., Germany). On the contrary, the SiC nanoparticles had a purity of more than 99 % and average particle size of 40 nm. Then, Cu mixed with 4 vol. % SiC, and 0.5 wt. % stearic acid was milled for 0, 1, 5, 10, 15, and 25 h under Ar atmosphere

at the BPR ratio of 10 and rotational speed of 300 RPM. The stainless steel milling medium was used for planetary milling. The powders were compressed into a steel mould under uniaxial pressure of 800 MPa to produce green compacts. The green compacts were sintered at 900 °C for an hour under argon gas. The sintered samples were ground by emery paper grades of 200-3000 and then, they were polished using alumina suspension of 3 μm and 1 μm , respectively. The samples were etched to reveal their microstructure. In addition, 35 wt. % iron trichloride + 5 wt. % hydrochloric acid + 60 wt. % water solution was used as etchant in copper-based nanocomposites. The microstructure of the samples was evaluated by X-Ray Diffraction (XRD) and Scanning Electron Microscopy (SEM), and their density was measured by the Archimedes method. Vickers microhardness of the sintered samples was determined using the Olympus micro-hardness tester (FM-700) under the load of 50 g and dwell time of 15 s.

Response Surface Methodology (RSM) was also utilized in the experimental design of many metallurgical processes [14]. The current study employed the one-factor design, a standard RSM design, to optimize the milling time and achieve better densification and high hardness in the nanostructured Cu prepared by high-energy mechanical milling method. To this end, Design-Expert 7.0 software was used to produce the experimental layout and model the empirical results.

3. RESULTS AND DISCUSSION

3.1. Microstructural Characterization

Figure 1 represents the Cu/SiC powder morphology after milling at different time durations. The powder morphology changed as the milling proceeded, as reported in the literature [3,11,15]. As seen, the powder particles became finer and slightly flaky in terms of quality after one hour milling. However, more flake-like particles were formed at the milling times of 5 and 10 h. The flakes fractured with enhanced work hardening at higher milling durations, hence the number of flaky particles decreased. As expected, the samples milled for 1 and 25 h had the smallest particle sizes. The morphological changes in the powder of metals and metal matrix composites during milling were reported in previous studies [10]. The powder milled for 25 h was characterized by semi-spherical morphology. Milling the composite powder also resulted in a homogeneous dispersion of nano-reinforcements. Figure 2 illustrates the elemental distribution maps for Si, C, and Cu and indicates the dispersion level of SiC nanoparticles in a composite particle after five hour of milling. Finally, we succeeded in obtaining homogenous dispersion of SiC nanoparticles.

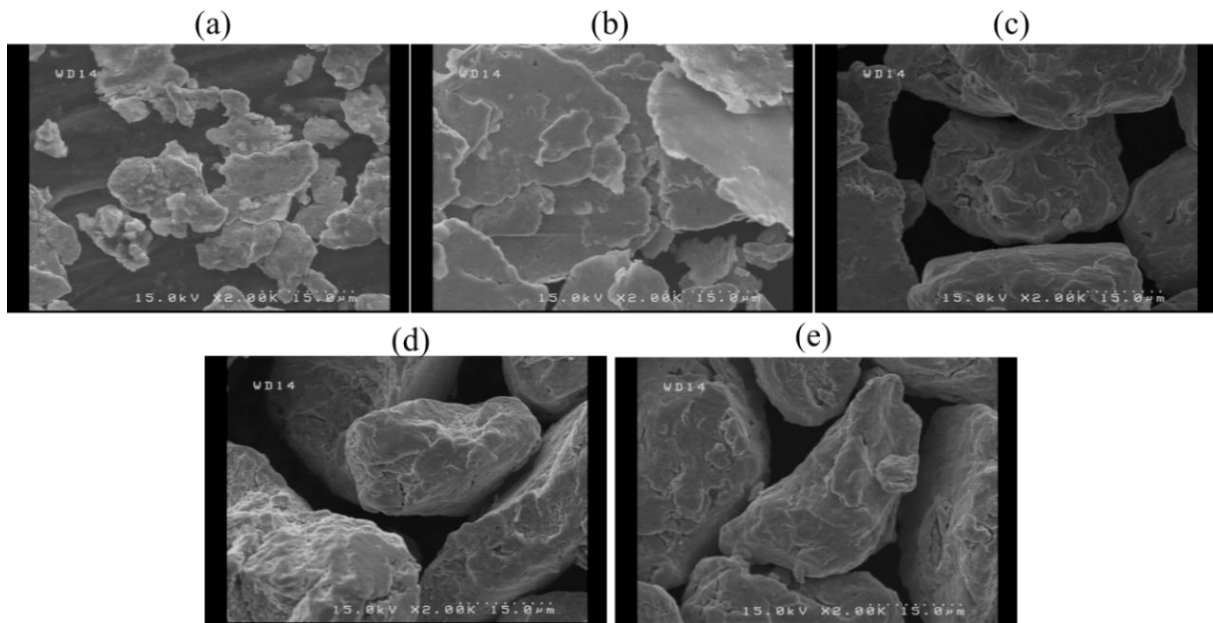


Figure 1. SEM micrographs of the powder milled for: (a) 1, (b) 5, (c) 10, (d) 15, and (e) 25 h

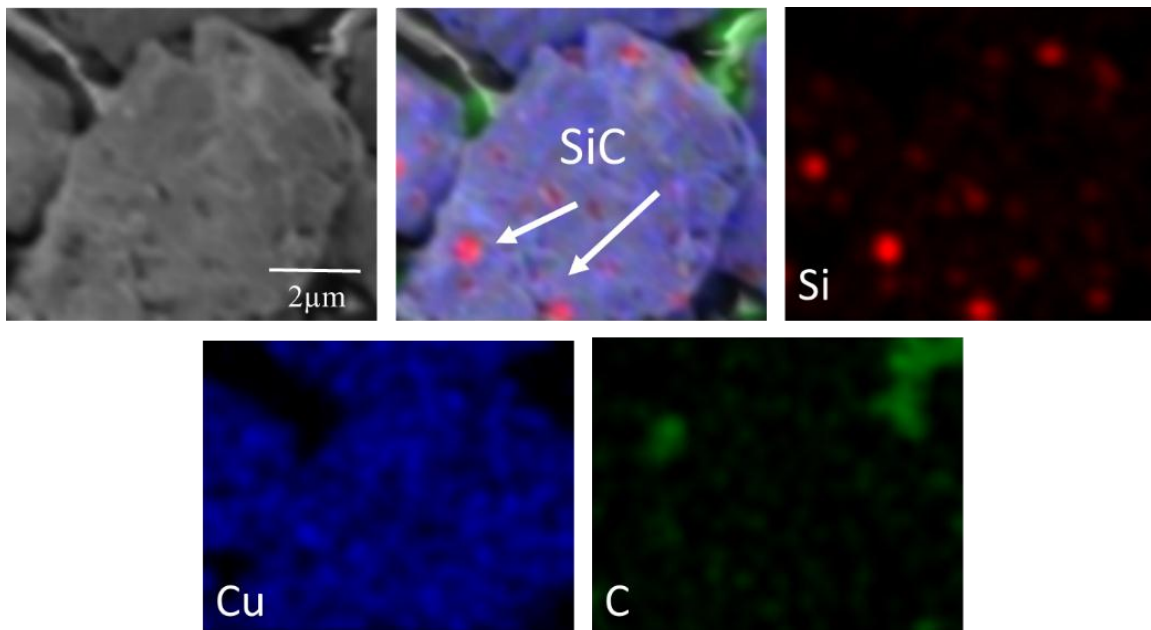


Figure 2. Elemental distribution map on a Cu/SiC nanocomposite particle

Figure 3 represents the optical microscope images of the bulk samples prepared by milling at different times and sintering processes. As observed, milling duration affected the grain size and shape of the bulk samples. The sample milled for an hour with deformed particles exhibited larger bimodal and relatively equiaxed grains. On the contrary, the sample milled for five hours with

flake-shape particles was characterized by elongated and fine grains. Longer duration of milling (e.g. 25 h) resulted in very fine and equiaxed grains, as shown in Figure 3c. Therefore, it can be concluded that milling time affects the final microstructure and grain morphology of the sintered samples.

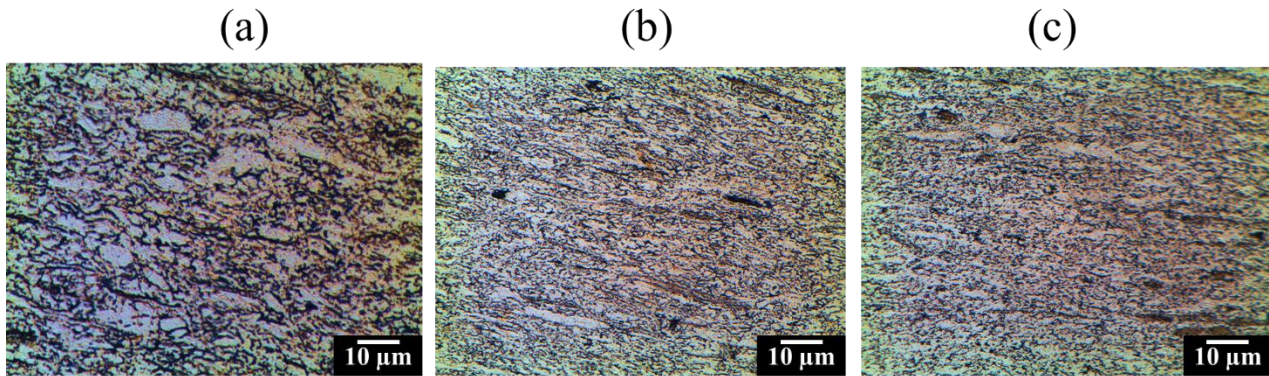


Figure 3. Optical images showing the microstructure of the composite samples prepared after milling for: (a) 1h, (b) 5h, and 25 h

3.2. Model Development

The current research employed one-factor response surface approach to plan the experimentation study. A total of 15 experiments were performed on Cu/SiC composite considering one input parameter (milling time). Table 1 lists the input parameter design factors and their values. The experimental layout and mathematical modelling of the experimental results were obtained using Design-Expert 7.0 software.

The regression models for all different experiments are all significant terms. In addition, Box Cox plots were used to select the correct power law transformation. Most of the data transformations can be described through the power function $y^{\lambda} = y^{\lambda}$, where λ is the powder of responses (y). If the standard deviation associated with the observation is proportional to the mean raised to the λ power, transforming the observation by the power gives a scale satisfying the equal variance requirement of the statistical model.

The lowest point on the Box Cox plot represents the value of lambda. Figure 4 shows the Box Cox plots for these two responses. the lambda value 3 refers to the

lowest point on the plots. Both actual and theoretical relationships were developed among models and process parameters, as illustrated in Eqs. (1-2). The regression models were obtained with A-Milling time. The response surface for all the models were constructed which seemed reasonable.

The normal probability plots of the responses are shown in Figs. 5 (a) and (b). As observed in this figure, the trend of residuals follows a normal distribution, the points of which conform a straight line expect some scatterings even with normal data. Figs. 5 (c) and (d) display the observed actual response values versus the predicted ones in terms of microhardness and relative density. According to these figures, it can be stated that the models can agreeably predict the microhardness and relative density of the sintered Cu/SiC nanocomposite at a function of milling time.

Figure 6 shows the data points and model as well as the observed residuals versus the milling time with a normal distribution. In this figure, the residuals seem to be randomly scattered with a normal distribution.

TABLE 1. One-factor design matrix with the collected data

Std	Run	Factor 1 A:Time, h	Response 1 Microhardness, HV	Response 2 Relative density
10	1	25	168.4	0.747
1	2	1	143	0.945
4	3	10	147.3	0.846
13	4	15	158.8	0.759
6	5	25	170.6	0.749
12	6	1	147.5	0.935
8	7	5	144.8	0.912
11	8	5	140.6	0.908
15	9	10	149.5	0.865
14	10	25	173.5	0.76
2	11	1	145.3	0.953
3	12	15	156.9	0.76
7	13	5	143.9	0.921
5	14	10	150	0.856
9	15	15	159.6	0.749

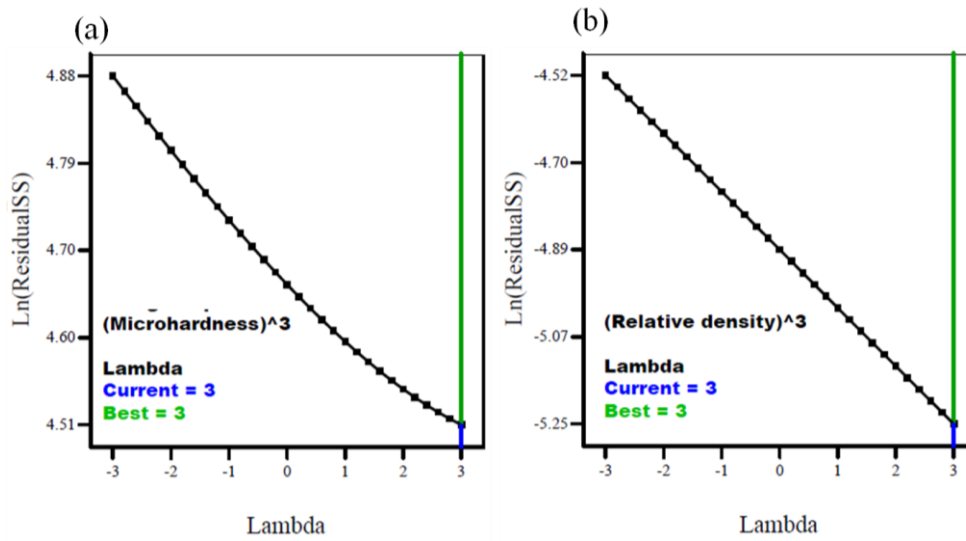


Figure 4. The Box Cox plots for the responses

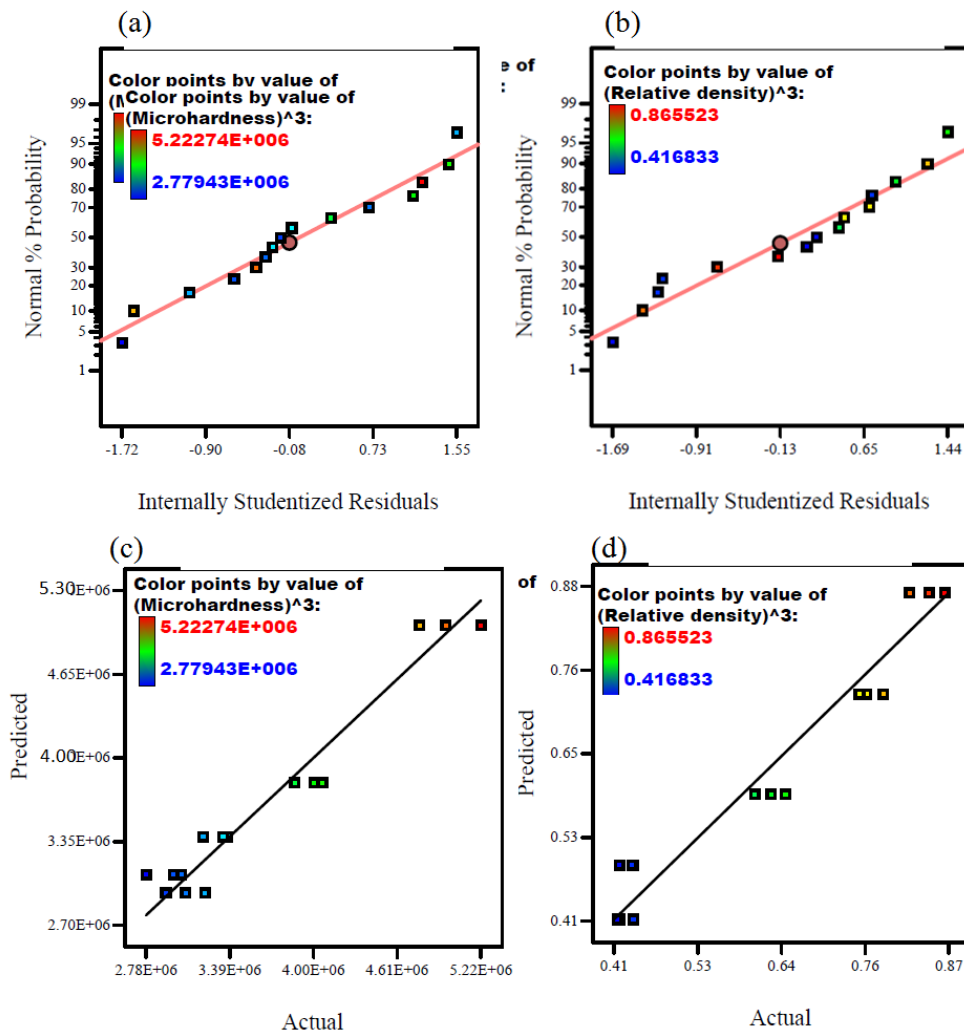


Figure 5. Normal probability plots of the responses and actual response values versus the predicted ones

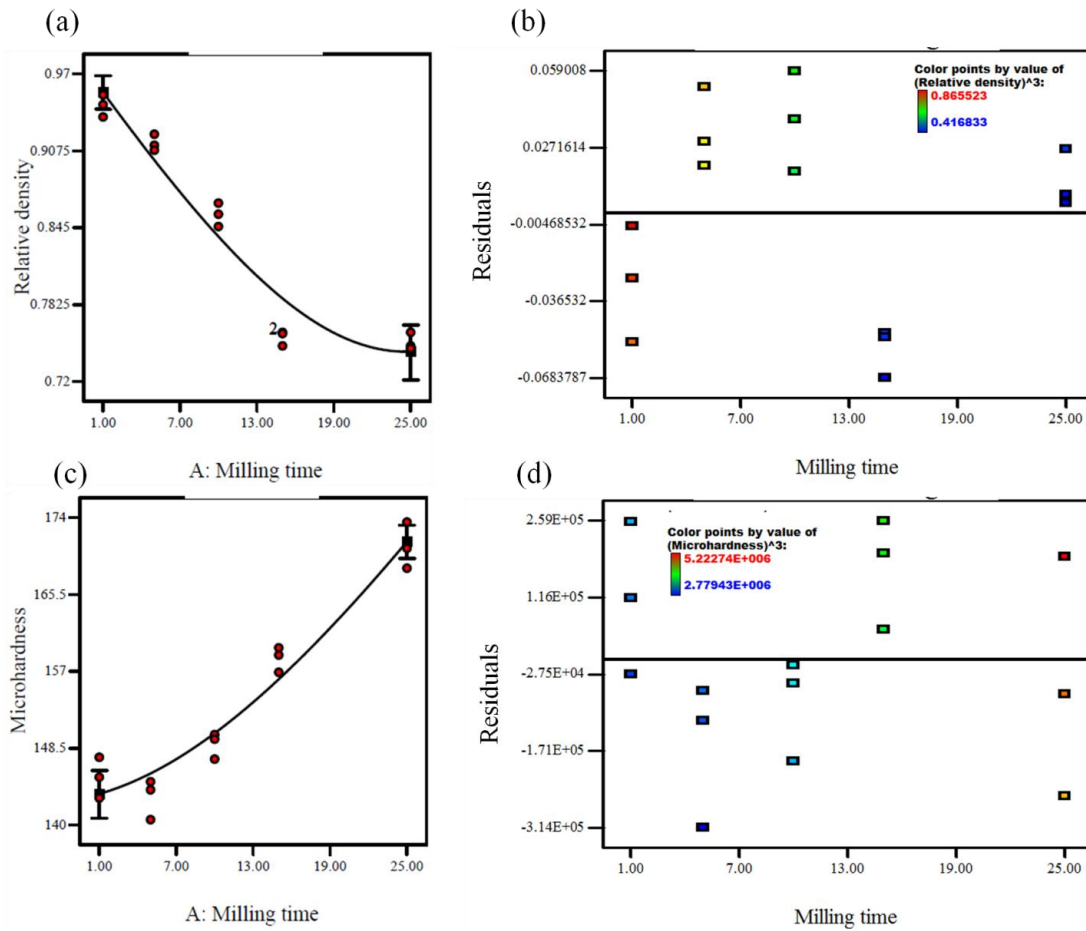


Figure 6. The data points, model, and observed residuals versus milling time

Construction of a regression model for microhardness and relative density of as-sintered samples requires consideration of the effect of milling time which is given in Equations (1) and (2):

$$Hv^3 = 3622608.57 + 1038971.65 A - 368602.19 A^2 \quad (1)$$

$$R^3 = 0.523 - 0.229 A + 0.118 A^2 \quad (2)$$

Tables 2 and 3 present Analysis of Variance (ANOVA) that helps obtain the microhardness and relative density (R) of the nanocomposite. In the case of the microhardness property of the nanocomposite given in Table 2, the following remarks can be made:

- The Model F-value of 111.97 is indicative of the significance of this model. There is only a 0.01 % chance of the occurrence of a "Model F-Value" this large due to noise.
- Values of "Prob > F" less than 0.0500 imply the significance of the model terms, i.e., both A and A².

- "Lack of Fit F-value" of 5.33 indicates that lack of fit is significant. There is only a 2.65 % chance of the occurrence of "Lack of Fit F-value" this large due to noise.
- The "Pred R-Squared" of 0.9169 is in reasonable agreement with the "Adj R-Squared" of 0.9407.
- "Adeq Precision" measures the signal-to-noise ratio. The ratio greater than 4 is desirable, and the ratio equal to 24.012 is an adequate signal. This model can be used to navigate the design space.

The major findings of the Table 3 are summarized in the following:

The Model F-value of 104.33 implies that the model is significant. There is only a 0.01 % chance that a "Model F-Value" this large could occur due to noise.

Values of "Prob > F" less than 0.0500 are indicative of the significance of the model terms, i.e., A and A².

The "Lack of Fit F-value" of 33.00 implies that Lack of Fit is significant. There is only a 0.01 % chance that a "Lack of Fit F-value" this large could occur due to noise.

The "Pred R-Squared" of 0.9197 is in reasonable agreement with the "Adj R-Squared" of 0.9366.

"Adeq Precision" measures the signal-to-noise ratio. The ratio greater than 4 is desirable, and that equal to

23.170 is the adequate signal. This model can be used to navigate the design space.

TABLE 2. ANOVA for microhardness of nanostructured Cu-4 vol. % SiC

Source	Sum of Squares	df	Mean Square	F Value	p-value Prob > F	
Model	8.39E+12	2	4.19E+12	111.9707	< 0.0001	significant
A-Milling time	7.83E+12	1	7.83E+12	208.9811	< 0.0001	
A ²	3.73E+11	1	3.73E+11	9.960634	0.0083	
Residual	4.49E+11	12	3.74E+10			
Lack of Fit	2.32E+11	2	1.16E+11	5.331375	0.0265	significant
Pure Error	2.17E+11	10	2.17E+10			
Cor Total	8.83E+12	14				
Std. Dev.			193507.4		R-Squared	0.94914
Mean			3653624		Adj R-Squared	0.940663
C.V. %			5.296314		Pred R-Squared	0.91688
PRESS			7.34E+11		Adeq Precision	24.0116

TABLE 3. ANOVA for as-sintered relative density of Cu/SiC powder milled for different times

Source	Sum of Squares	df	Mean Square	F Value	p-value Prob > F	
Model	0.408613	2	0.204307	104.3275	< 0.0001	significant
A-Milling time	0.381079	1	0.381079	194.5947	< 0.0001	
A ²	0.038391	1	0.038391	19.60384	0.0008	
Residual	0.0235	12	0.001958			
Lack of Fit	0.020408	2	0.010204	33.00037	< 0.0001	significant
Pure Error	0.003092	10	0.000309			
Cor Total	0.432113	14				
Std. Dev.			0.044253		R-Squared	0.945616
Mean			0.617838		Adj R-Squared	0.936553
C.V. %			7.162545		Pred R-Squared	0.919746
PRESS			0.034679		Adeq Precision	23.17038

4. CONCLUSION

In this research, Cu/SiC powder was milled at different times and consolidated through conventional sintering method. In addition, the hardness and density of the sintered composite compacts were determined. Then, one-factor response surface approach was taken into account to model the effects of milling time on the composite features. The results from ANOVA analysis revealed that with a cube transformation, both microhardness and relative density had a polynomial

relationship with the milling time. Of note, there was good agreement between the predicted results and measured values.

ACKNOWLEDGEMENTS

The authors would like to express their gratitude to University of Maragheh for financial support of this research.

REFERENCES

1. Akbarpour, M. R., Alipour, S., Safarzadeh, A., Kim, H. S., "Wear and friction behavior of self-lubricating hybrid Cu-(SiC + x CNT) composites", *Composite Part B: Engineering*, Vol. 158, (2019), 92–101. <https://doi.org/10.1016/j.compositesb.2018.09.039>
2. Somani, N., Sharma, N., Sharma, A., Gautam, Y. K., Khatri, P., Solomon, J. A. A., "Fabrication of Cu-SiC composites using powder metallurgy technique", *Materials Today: Proceedings*, Vol. 5, No. 14, (2018), 28136–28141. <https://doi.org/10.1016/j.matpr.2018.10.055>
3. Akbarpour, M. R., Najafi, M., Alipour, S., Kim, H. S., "Hardness, wear and friction characteristics of nanostructured Cu-SiC nanocomposites fabricated by powder metallurgy route", *Materials Today Communications*, Vol. 18, (2019), 25–31. <https://doi.org/10.1016/j.matcomm.2018.11.001>
4. Torabi, H., Arghavanian, R., "Investigations on the corrosion resistance and microhardness of Cu-10Sn/SiC composite manufactured by powder metallurgy process", *Journal of Alloys and Compounds*, Vol. 806, (2019), 99–105. <https://doi.org/10.1016/j.jallcom.2019.07.245>
5. Akbarpour, M. R., "Effects of mechanical milling time on densification, microstructural characteristics and hardness of Cu-SiC nanocomposites prepared by conventional sintering process", *Materials Chemistry and Physics*, Vol. 261, (2021), 124205. <https://doi.org/10.1016/j.matchemphys.2020.124205>
6. Raimundo, R. A., Santos, K. V., Lourenco, C. S., Costa, F. A., Morales, M. A., Macedo, D. A., Silva, A. G., Gomes, U. U., "Effect of high energy milling on microstructure and mechanical properties of Al₂O₃-10 wt% Co composites consolidated by spark plasma sintering (SPS)", *Ceramics International*, Vol. 47, No. 1, (2021), 677–685. <https://doi.org/10.1016/j.ceramint.2020.08.176>
7. Efe, G. C., Yener, T., Altinsoy, I., İpek, M., Zeytin, S., Bindal, C., "The effect of sintering temperature on some properties of Cu-SiC composite", *Journal of Alloys and Compounds*, Vol. 509, No. 20, (2011) 6036–6042. <https://doi.org/10.1016/j.jallcom.2011.02.170>
8. Efe, G. C., Zeytin, S., Bindal, C., "The effect of SiC particle size on the properties of Cu-SiC composites", *Materials & Design (1980-2015)*, Vol. 36, (2012), 633–639. <https://doi.org/10.1016/j.matdes.2011.11.019>
9. Akbarpour, M. R., Mirabad, H. M., Alipour, S., "Microstructural and mechanical characteristics of hybrid SiC/Cu composites with nano- and micro-sized SiC particles", *Ceramics International*, Vol. 45, No. 3, (2019), 3276–3283. <https://doi.org/10.1016/j.ceramint.2018.10.235>
10. Salur, E., Acarer, M., Şavklıyıldız, İ., "Improving mechanical properties of nano-sized TiC particle reinforced AA7075 Al alloy composites produced by ball milling and hot pressing", *Materials Today Communications*, Vol. 27, (2021), 102202. <https://doi.org/10.1016/j.matcomm.2021.102202>
11. Ponhan, K., Tassenberg, K., Weston, D., Nicholls, K. G., Thornton, R., "Effect of SiC nanoparticle content and milling time on the microstructural characteristics and properties of Mg-SiC nanocomposites synthesized with powder metallurgy incorporating high-energy ball milling", *Ceramics International*, Vol. 46, No. 17, (2020), 26956–26969. <https://doi.org/10.1016/j.ceramint.2020.07.173>
12. Schubert, T., Brendel, A., Schmid, K., Koeck, T., Zieliński, W., Weißgärber, T., Kieback, B., "Interfacial design of Cu/SiC composites prepared by powder metallurgy for heat sink applications", *Composites part A: Applied Science and Manufacturing*, Vol. 38, No. 12, (2007), 2398–2403. <https://doi.org/10.1016/j.compositesa.2007.08.012>
13. Suryanarayana, C., "Mechanical alloying and milling", *Progress in Materials Science*, Vol. 46, No. 1-2, (2001), 1–184. [https://doi.org/10.1016/S0079-6425\(99\)00010-9](https://doi.org/10.1016/S0079-6425(99)00010-9)
14. Gangil, M., Pradhan, M. K., "Modeling and optimization of electrical discharge machining process using RSM: A review", *Materials Today: Proceedings*, Vol. 4, No. 2, (2017), 1752–1761. <https://doi.org/10.1016/j.matpr.2017.02.017>
15. Akbarpour, M. R., Salahi, E., Hesari, F. A., Simchi, A., Kim, H. S., "Microstructure and compressibility of SiC nanoparticles reinforced Cu nanocomposite powders processed by high energy mechanical milling", *Ceramics International*, Vol. 40, No. 1, (2014), 951–960. <https://doi.org/10.1016/j.ceramint.2013.06.091>



Materials and Energy Research Center

MERC

Contents lists available at ACERP

Advanced Ceramics Progress

Journal Homepage: www.acerp.ir

Advanced Ceramics Progress

Original Research Article

Experimental and Numerical Study of the Thermo-Mechanical Behavior of Plasma-Sprayed Gadolinium and Yttria Zirconate-Based Thermal Barrier Coatings

N. Nayebpashaei ^{a,*}, E. Etemadi ^b, B. Mohammad Sadeghi ^c, S. H. Seyedein ^d^a Assistant Professor, Department of Metallurgy and Mechanical Engineering, Technology and Engineering Research Center, Standard Research Institute (SRI), Karaj, Alborz, Iran^b PhD Candidate, Faculty of Materials Science and Engineering, Malek Ashtar University, Tehran, Tehran, Iran^c Assistant Professor, School of Metallurgy and Materials Engineering, Iran University of Science and Technology, Tehran, Tehran, Iran^d Professor, School of Metallurgy and Materials Engineering, Iran University of Science and Technology, Tehran, Tehran, Iran* Corresponding Author Email: n.nayebpashaei@standard.ac.ir (N. Nayebpashaei)URL: https://www.acerp.ir/article_144395.html

ARTICLE INFO

A B S T R A C T

Article History:

Received 01 January 2022
Received in revised form 02 February 2022
Accepted 06 February 2022

Keywords:

Functionally Graded Thermal Barrier Coating (FGTBC)
Thermal Shock
Residual Stress
Nano-Indentation
Finite Element Method

The current study aims to analyze the thermal and residual stress distributions in both duplex and functionally-graded thermal barrier coatings (TBCs) of yttria-stabilized zirconia (YSZ) and gadolinium zirconate (GZ) during a realistic heating regime. To this end, finite element model was employed to model the effects of thermal loading on the thermomechanical response and stress distribution. In addition, three different YSZ-based TBC systems, one duplex, and two FG-TBCs were fabricated using the APS method. The coatings were characterized based on SEM/EDS, map analysis, and XRD. The residual stress, elastic modulus, microhardness, and fracture toughness of the coatings were determined using nanoindentation method. The obtained results revealed that the microstructure, porosity, and chemical composition changed gradually due to the functionally-graded coating. Examination of the surface of the samples after the application of thermal shock showed that the separation of the layers occurred more frequently in the cases of two-layer coatings than in the graded ones. The contours of the heat flux and nodal temperatures confirmed that most of the damaging thermal residual stresses were concentrated in the ceramic top coat, thus resulting in less damage and life-shortening of the substrate. The magnitude of the residual stress in the FG-TBC was lower than that in the duplex TBC, and the stress distribution was more uniform, hence improvement in the performance and extension of the life of the thermal barrier system. According to the findings, the YSZ-based TBC outperformed the gadolinium zirconate-based TBC in terms of thermal shock resistance and residual stress.

<https://doi.org/10.30501/ACP.2022.322563.1078>

1. INTRODUCTION

Tolerance of higher temperatures in different parts of internal combustion engines has always been an important concern in aerospace and turbine industries.

Thermal Barrier Coatings (TBCs) are regarded as important elements in the durability of hot section components. They function as the insulating components such as turbine blades, combustor cans, ducting and nozzle guide vanes operating at elevated temperature. In

Please cite this article as: Nayebpashaei, N., Etemadi, E., Mohammad Sadeghi, B., Seyedein, S. H., "Experimental and Numerical Study of the Thermo-Mechanical Behavior of Plasma-Sprayed Gadolinium and Yttria Zirconate-Based Thermal Barrier Coatings", *Advanced Ceramics Progress*, Vol. 7, No. 4, (2021), 36-51. <https://doi.org/10.30501/ACP.2022.322563.1078>

2423-7485/© 2021 The Author(s). Published by MERC.

This is an open access article under the CC BY license (<https://creativecommons.org/licenses/by/4.0/>).

addition, they make an increase in the operating temperature of gas turbines possible [1-5].

The typical TBC is composed of three layers namely Bond Coat (BC), Top Coat (TC), and Thermally Grown Oxide (TGO). The BC is made of MCrAlY (with M=Ni and/or Co), and the TC often consists of a thermal barrier layer based on Yttria-Stabilized Zirconia (YSZ) [1-3]. At high temperatures, oxygen is transferred from the TC to the BC through micro cracks and interconnected pinholes within the TC. During the operation, aluminum in the BC diffuses and reacts with oxygen from the combustion gases. As a result, an oxidized scale of alumina (Al_2O_3) is formed on the BC called the TGO layer which is primarily related to the oxidation of the BC. The major disadvantages of YSZ are the limited operational temperature resulting from the phase transformation, sintering induced volume shrinkage, and low corrosion resistance. To overcome these drawbacks, the necessity of searching for new alternative materials is highlighted more than ever [1,6-8]. Zirconate-based TBCs are expected to be appropriate candidates for future applications in high-temperature components due to their low thermal conductivity, high stability, and high sintering resistance at high temperatures [1,8]. Gadolinium Zirconate ($Gd_2Zr_2O_7$ or GZ) is another candidate material that is a new and promising alternative ceramic coating material to YSZ that enjoys several major advantages such as higher thermal stability at elevated temperatures and lower thermal conductivity (1.3 W/mK^{-1} at $1100 \text{ }^\circ\text{C}$), and better hot corrosion resistance than those of YSZ (1.8 W/mK^{-1} at $1100 \text{ }^\circ\text{C}$), thus potentially allowing better thermal insulation [9,10].

Some problems may arise in the case of plasma-sprayed TBC such as spallation caused by the TGOs with different thickness values and morphologies as well as cracking in long-term services due to their poor bond strength and high residual stresses. Functionally Graded Thermal Barrier Coatings (FG-TBCs) with a gradual compositional variation from the TC to the BC were proposed to overcome these limitations. The microstructural grading of FG-TBCs could help reduce the mismatch in thermomechanical properties. In addition, using FG-TBCs may improve other properties such as adhesion, corrosion, and oxidation [4,5,11].

Evaluating and measuring the residual stresses is of high importance in industry in determining the lifetime of the components. The measurement techniques for residual stress in the coatings can be divided into two groups of destructive and non-destructive methods. The non-destructive methods measure some parameters that are related to the stress. X-ray or neutron diffraction are referred to as the non-destructive methods, and the hole-drilling and layer removal method are regarded as the destructive ones. Nanoindentation is an indentation method for testing the hardness and other related mechanical properties of materials. It is also used to

estimate the residual stress in thin films and coatings [12-15].

According to the literature, several experimental, analytical, and numerical studies have been conducted on the residual stress, crack evolution, failure mechanism, splatting impact, TGO and layer thickness, and thermal shock resistance of the TBCs [7,8,16-20]. For instance, Z. Valefi and M. Saremi [7] evaluated the effects of plasma spray parameters, atomizing gas, and substrate preheat temperature on the microstructure and phase composition of YSZ coatings produced through the SPSS process. According to their findings, upon increasing the power of plasma, using hydrogen as the precursor atomizing gas, and increasing the substrate preheat temperature, the amount of non-pyrolyzed precursor in the coatings would decrease [7]. S. M. Yunus et al. [17] compared the thermal resistance of a the plasma sprayed multilayer (GZ/YSZ) TBC with that of the single-layer YSZ coating and found that the single-layer YSZ system performed 12 % better than the multilayer TBC system at $1250 \text{ }^\circ\text{C}$ [17]. N. Nayeypashae et al. [19] simulated the residual stress distribution and fracture mode of the TBCs based on the micromechanical approach FE with and without considering the presence of two-phase TGO. Their obtained results showed acceptable agreement between the simulated and experimental failure and crack growth modes. J. Song et al. [21] evaluated the effect of the non-uniform growth of the TGO on the stress evolution and interfacial crack initiation using the finite element method. They concluded that the non-uniform growth of the TGO would increase the magnitude of the residual stress in the TC layers, thus leading to early initiation of interfacial cracks [21].

The current study aimed to investigate the thermal and residual stress distribution in duplex TBC and functionally graded YSZ and GZ-TBCs during a realistic heating regime including heating, operating time, and final cooling. Despite the common applications of functionally graded strategies in surface engineering, very few studies have been conducted on the numerical aspects of functionally graded TBCs with novel zirconate (GZ) composition as the top ceramic layer TBCs in the literature. In addition, limited studies have focused on the thermal shock behavior of the TBC containing GZ as the TC so far.

2. MATERIALS AND METHODS

Yttria Zirconate-based TBC is usually applied in experimental studies. The used powders for bond and top coats were prepared according to the instructions given in Table 1. Prior to spraying, the starting powders were heat-treated at $100 \text{ }^\circ\text{C}$ for two hours to remove moisture. To obtain better substrate roughness and a clean surface, the Inconel (substrate) was blasted with silicon carbide particles with a mesh count of 25 in. at the optimum

pressure of four bars, followed by smooth grinding, degreasing, and acid pickling. Table 2 lists the plasma spray parameters used for TBC coating. X-Ray Diffraction (XRD) analysis was carried out to evaluate the materials formed on the top surface of the coating and characterize the coating surface after cooling the sprayed sample using a Siemens D 500 instrument. A thermal cycle was taken into account at the dwell time of 300 seconds and temperature of 1300 °C to perform the

thermal shock. The samples were heated to the target temperature of 1300 °C in an electric furnace with air and then cooled to 25 °C using an air blast unit.

The thermal shocks with the oxidation time (cause of TGO formation) were repeated 45 times. Finally, to reveal the microstructure of the multiple shocked coatings in SEM studies, the samples were mounted, ground, and polished. The coating components were identified using OM, SEM/EDS, and mapping analysis.

TABLE 1. Specifications of powders used in plasma spraying

Layer	Composition	Powder	Morphology	Size (µm)
Top coat	ZrO ₂ -8 wt % Y ₂ O ₃	Metco 204 –NS	Spherical	40-75
Bond coat	Ni-22Cr-10Al-1Y	AMDRY 962	Spherical	11-106

TABLE 2. Operating parameter of plasma spraying Inconel 738 used in this research

Parameter	Unit	YSZ (metco204Ns)	25 NiCrAlY + 75 YSZ	50 NiCrAlY + 50 YSZ	75 NiCrAlY + 25 YSZ	NiCrAlY (Amdry962)
Arc current intensity	A	500	500	500	450	450
Voltage	V	55	55	55	50	50
Carrier gas flow rate (Argon)	SCFH*	80	80	80	85	85
Carrier gas flow rate (Hydrogen)	SCFH	15	15	15	15	15
Powder carrier gas flow rate (Argon)	SCFH	30	30	30	30	30
Powder feed rate	lb/hr	25	20	20	15	15
Spray distance	cm	8	8	10	10	12
Injection diameter	mm	2	2	2	2	2
Cooling circulation system	-	water	water	water	water	water

*Standard Cubic Feet per Hour

2.1. Evaluation of Residual Stress by Nano Indentation Method

In this study, the residual stress was measured through nanoindentation method as well as indentation fracture technique. When using this technique to indent the surface of a brittle material with moderate force, it often produces a permanent impression with radially aligned cracks at the corner of the indent [12,22]. In order to calculate the residual stress, first, the mechanical properties of the coating such as Young's modulus, microhardness, and fracture toughness should be calculated. The calculation method is based on the methods presented in the previous study [23].

According to the load-depth curve, the hardness H and reduced modulus E_r are defined by Equations 1 and 2 [23]:

$$H = \frac{P_{\max}}{A_c} \quad (1)$$

$$E_r = \frac{\sqrt{\pi}}{2\beta} \frac{S}{\sqrt{A_c}} \quad (2)$$

where P_{\max} is the maximum load, A_c the contact area, $S = dP/dh$ the contact stiffness at initial unloading, and b a constant that depends on the geometry of the indenter. The reduced modulus E_r is defined through Equation (3) [23] as:

$$\frac{1}{E_r} = \frac{1-\nu_i^2}{E_i} + \frac{1-\nu_s^2}{E_s} \quad (3)$$

where E and E_i are the elastic moduli of the specimen and indenter, respectively, and ν and ν_i are the Poisson's ratios of the specimen and indenter, respectively [23]. The Poisson's ratios of the TBC and diamond indenter are 0.2 and 0.07, respectively, and the value of E_i for the diamond is 1141 GPa [24].

For Berkovich diamond indenter, we have $A_c = 24.49 h_c^2 \approx 24.5 h_c^2$ where h_c is the contact depth. Hence, Equation (1) will be as $H = \frac{P_{\max}}{24.5 h_c^2}$.

When a Vickers indenter is penetrated into the interface of two different materials, the fracture toughness for the

coating/BC interface is evaluated using Equation (4) [23]:

$$K_{IC} = \delta \left(\frac{E}{H} \right)^{1/2} \frac{P}{c^{3/2}} \quad (4)$$

where δ is the geometric factor and $\delta=0.015$ for a Vickers indenter, and $c = (c_1+c_2+c_3)/3$ is the average length of three radial cracks with the lengths of c_1 , c_2 , and c_3 [23].

When applying the TBC containing stress and nanoindentation perpendicular to the cross-section of the TC layer in accordance with Figure 1, the fracture toughness is measured through Equation (5) [23]:

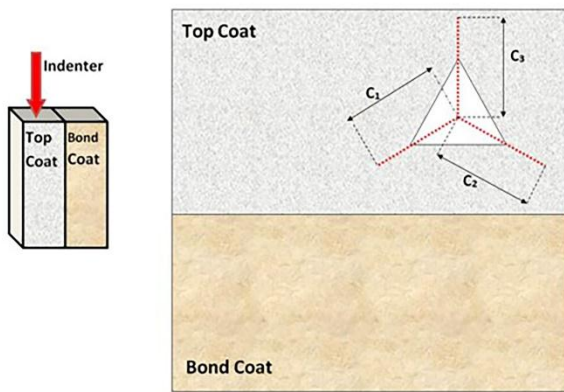


Figure 1. Schematics of Berkovich indentation perpendicular to the top coat of multiple-shocked coating

$$K_{IC} = \delta \left(\frac{E}{H} \right)_i^{1/2} \frac{P}{c^{3/2}} + \frac{2}{\sqrt{\pi}} \sigma c^{1/2} \quad (5)$$

Then, the ratio $P/c^{3/2}$ can be obtained as [23]:

$$\frac{P}{c^{3/2}} = \left(\frac{K_{IC}}{\chi_i} \right) + \left(-\frac{2\sigma}{\sqrt{\pi}\chi_i} \right) c^{1/2} \quad (6)$$

where $\chi_i = \delta \left(\frac{E}{H} \right)_i^{1/2}$. Equation (6) is regarded as a function of $c^{-1/2}$ where $\left(-\frac{2\sigma}{\sqrt{\pi}\chi_i} \right)$ and $\left(\frac{K_{IC}}{\chi_i} \right)$ denote the slope and intercept of Equation (6), respectively [23]. To obtain a better linear equation, a series of indentation tests should be carried out.

2.2. Performing Nano Indentation Test

A Triboscope system (Hyston Inc. USA) was used to measure the stress in the nanoindentation method. A Berkovich diamond indenter was used for performing nanoindentation experiments. A device equipped with Atomic Force Microscopy (AFM) (NanoScope E, Digital Instruments, USA) was also used to examine the surface topography of the specimens. The values of the loading rate, pause time, and unloading rate were 5 mNs^{-1} , 5 s , and 5 mNs^{-1} , respectively. At room temperature, a series of forces ranging from $500 \text{ }\mu\text{N}$ to $10,000 \text{ }\mu\text{N}$ in

increments of $1,000 \text{ }\mu\text{N}$ were perpendicularly applied to the cross-section of the top layer of the multi-shocked TBC considering the YSZ. The length of the cracks was calculated using the image processing toolbox of the MATLAB software.

2.3. Finite Element Analysis

This section primarily aims to determine the temperature and stress distribution in the TBC. To this end, a simulation of TBC was performed using ABAQUS software. In addition, a two-dimensional finite element model was employed to numerically simulate the temperature distribution and consequent induced residual stress in the TBC. The schematic illustration of the studied area in the TBC system used in the hot section of the gas turbines is given in Figure 2.

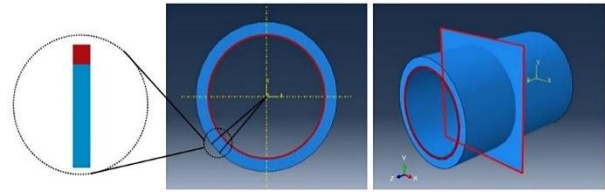


Figure 2. TBC calculation domain

As graphically shown in Figure 3, the duplex TBC system consists of both metallic and ceramic layers including an Inconel 738 substrate, a NiCoCrAlY sliding layer (BC), and GZ (YSZ) as a Top Layer (TC). The selected functionally graded TBC system used in this study is made of the following layers: an Inconel 738 substrate, a NiCoCrAlY bond (BC), 50 % BC + 50 % GZ (YSZ), and GZ (YSZ) as the top coat (Figure 3).

In order to obtain accurate results, appropriate thermal and mechanical boundary conditions should be considered. The thermal cycling applied at the highest level of the thermal barrier is shown in Figure 4. The heating cycle under study involves heating from $25 \text{ }^\circ\text{C}$ to $1300 \text{ }^\circ\text{C}$ in 30 seconds. In the second stage, it sustains temperature of $1300 \text{ }^\circ\text{C}$ for 200 seconds and in the third stage, it is cooled down from $1300 \text{ }^\circ\text{C}$ to $25 \text{ }^\circ\text{C}$ in 30 seconds.

In order to provide a suitable boundary condition for the bottom surface of the substrate, a thermal flux was used on this surface. To apply this thermal flux, the heat transfer coefficient (h) was assumed to be $25 \text{ W/m}^2\cdot\text{K}$ [25].

As illustrated in Figure 5, in order to satisfy the mechanical boundary conditions, the point of the TBC system should be kept constant. In addition, the degree of freedom of the movement of all nodes located on the vertical surface of the TBC system should be closed in a horizontal direction to create symmetrical boundary conditions. On the contrary, the degree of freedom of their movement in the vertical direction should be kept

open. Considering the dependence of the thermal and mechanical properties of the material on temperature, we gave the properties of different layers of TBC at different temperatures to the software as the inputs. Table 3 lists

these thermal and mechanical properties of different layers of TBC [26-28]. In order to validate the proposed model in this study, a comparison was made between the simulation and experimental results obtained from the nanoindentation method.

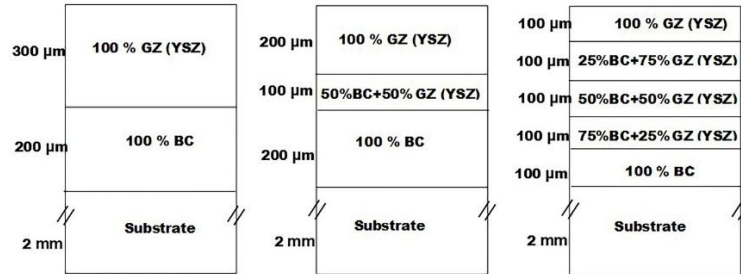


Figure 3. Schematic view of (a) duplex and functionally graded (b,c) coating designs

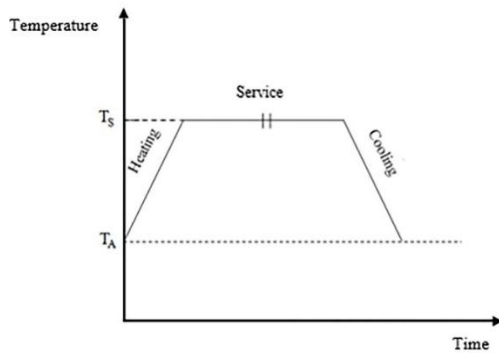


Figure 4. Thermal cycle applied at the highest level of thermal barrier coating

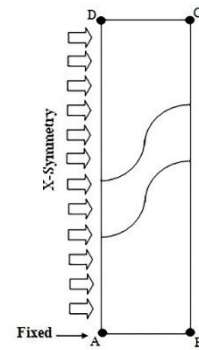


Figure 5. Assigning mechanical boundary conditions

TABLE 3. Thermal and mechanical properties of different layers of the thermal barrier coating [26–28]

Material properties	Temperature (K)	TGO Al ₂ O ₃	Top Coat YSZ	Top Coat GZ	Bond Coat NiCrAlY	Substrate Hastelloy-X
E (GPa)	276	380	210	175	225	201
	673	338	205	170.8	186	180
	1073	-	181	150.8	147	150
	1473	312	162	135	134	141
P (Kg/m ³)	276					
	673	3978	5400	6320	7320	8220
	1073					
	1473					
ν	276					
	673	0.27	0.2	0.2	0.3	0.32
	1073					
	1473					
α (×10 ⁻⁶ .K ⁻¹)	276	5.1	9.1	8.9	11.6	13.4
	673	-	10.58	9.04	14	14.2
	1073	-	11.13	10.08	16	15.6
	1473	9.8	8.5	10.9	20.8	15.8
C _p (J.(kg.K) ⁻¹)	276		500	344	501	442
	673		576	430	592	514
	1073	857	637	456	781	668
	1473		650	460	764	831
K (W/m.°C)	276		1.06	1.11	4.3	10.4
	673		0.8	0.77	6.4	18.6
	1073	25.2	0.65	0.61	10.2	23.8
	1473		0.62	0.58	11.3	27.4

3. RESULTS AND DISCUSSION

Figure 6a shows the optical microscopy images of the structure of YSZ-based duplex TBC composed of three sections: substrate, bond coat, and top coat. The transparent areas represent the metal phases, dark gray areas the ceramic phases, and black areas the pores in the coating. The BC shown in a lighter color is a layered structure consisting of splats approximately parallel to the substrate surface. This microstructure is one of the main features of plasma spray coatings. As observed in Figure 6a, the interface between the layers of the TC and bond coats in the duplex TBC is clearly distinguished. Figure 6b shows the optical microscopy images of the structure of YSZ-based functionally graded TBC. According to this figure, the coating is characterized by a layered structure, and each layer contains micro cracks and pores that appear in black color. From the BC to the TC layer of the FG-TBC, the portion of NiCrAlY in the layers gradually changes. This gradient distribution of layers in the FG-TBC leads to the reduction of residual stresses caused by different CTEs between the metal and ceramic phases.

X-Ray Diffraction (XRD) analysis was carried out to distinguish between the phases of the initial (feedstock) powder and as-sprayed TC layer for Yttria stabilized Zirconia-based TBC, the results of which are shown in Figure 7. As observed in Figure 7a, the feedstock powder contains zirconium dioxide (ZrO_2) with the dominant structure of tetragonal phase in the form of partially stabilized zirconia and stabilized (non-transformable) zirconia and lower amount of cubic and monoclinic phases. As shown in Figure 7b, plasma spraying causes a

significant reduction in the intensity of monoclinic phase. The as-sprayed coating is mostly composed of tetragonal phase with only traces of the monoclinic phase, and the amount of the cubic phase decreases in terms of the feedstock.

According to the equilibrium phase diagram of zirconia-yttria, the stable zirconia phase at room temperature contains 8 % of the weight of zirconia in the tetragonal phase. The non-transformable (stable) tetragonal phase is the main phase of plasma-sprayed zirconia which is formed as a result of rapid cooling of the whipped molten particles on the surface. In plasma spraying, a high proportion of Y_2O_3 (8 % by weight) in YSZ increases the phase temperature stability of the tetragonal ZrO_2 after cooling. Plasma spraying as a rapid process often leads to the formation of transformable (semi-stable) phases in the coating. In plasma sprayed TBCs, rapid cooling leads to the formation of a transformable (semi-stable) tetragonal phase (t') instead of a non-transformable (stable) tetragonal phase (t). In other words, rapid cooling during thermal spraying preserves the yttrium distribution of the primary powder in the tetragonal phase, thus leading to preservation of the transformable (semi-stable) tetragonal phase at room temperature. When the YSZ coating is semi-stable, and its chemical composition is the same as that of the more stable phase at higher temperatures, the chemical composition of the material will be mixed at room temperature rather than just the tetragonal phase predicted at room temperature. The resulting phases will be cubic and tetragonal [29,30].

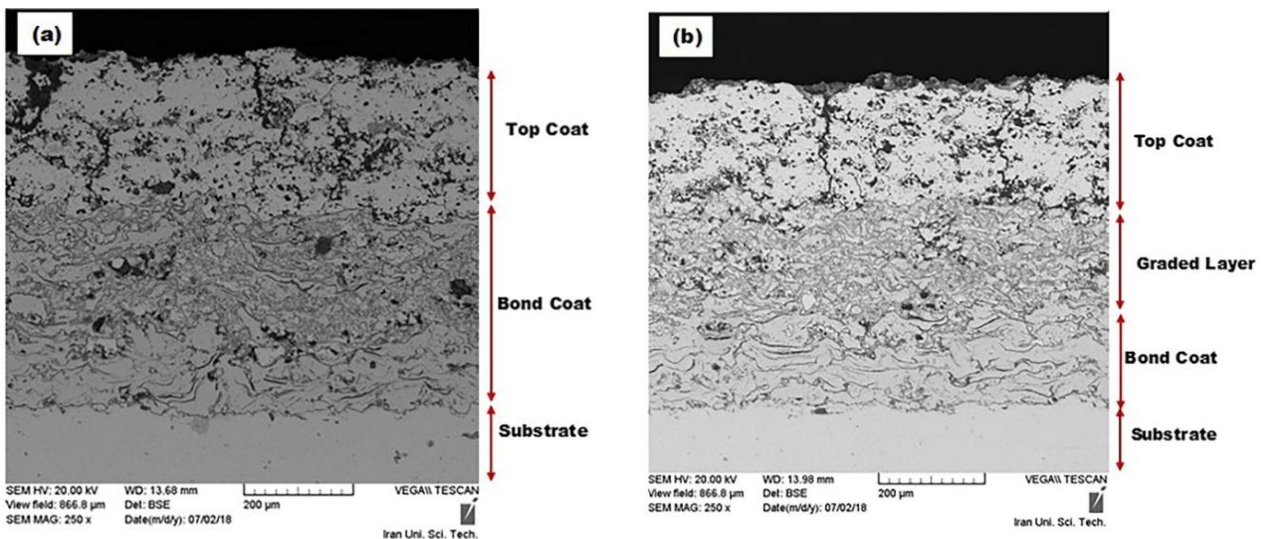


Figure 6. SEM images of the structure of (a) duplex coating and (b) functionally graded Yttria stabilized Zirconia based thermal barrier coating

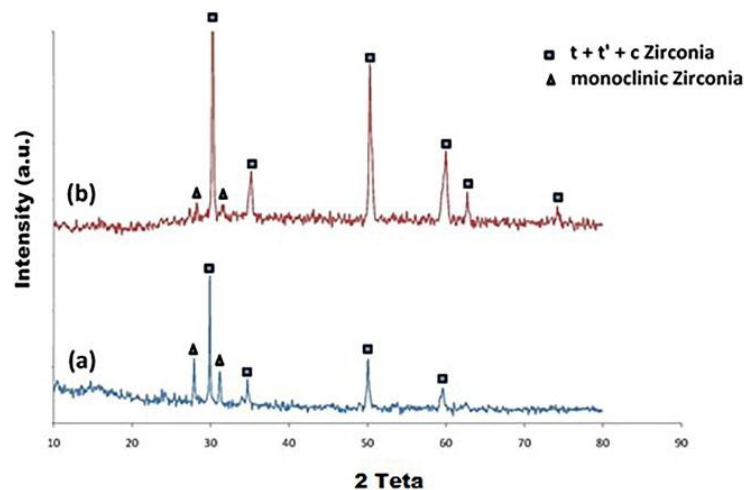


Figure 7. X-Ray Diffraction (XRD) analysis of a) the feedstock powder of YSZ-based top coat and b) as sprayed topcoat

Thermal spraying forms semi-stable compounds sensitive to the spray parameters. Even if the samples are coated with spray parameters that are as similar as possible (same source power, similar spray distance, etc.), the differences in the properties of the initial powder should be ignored. These changes in the properties of the initial powder result in different microstructures (porosity and pore properties) in the generated coatings. Therefore, the coatings differ in their properties, hence different phases of the sprayed coating [29,31,32].

High amount of cubic and monoclonal phases, instead of the tetragonal phase, is undesirable due to their lower mechanical properties. When cooled down to room temperature, the tetragonal phase is transformed into the monoclonal phase. This transformation is accompanied by an increase in the volume, hence creation of significant stress and possibly nucleation and crack growth within the TBC that would reduce the lifecycle of the coating [29–31].

As reported, the removal and depletion of yttrium (Y) from YSZ during operation and its exposure to high temperatures (above 1200 °C) and thermal cycling would form a monoclinic phase upon cooling to room temperature. As a result, the monoclinic phase is formed based on the Y-depleted tetragonal phase during cooling. According to the findings, the higher the concentration of stabilizing elements in the tetragonal zirconia, the lower the proportion of formed monoclinic phase [29,32].

Normally, it is expected that no peak is found for monoclinic zirconia ($m\text{-ZrO}_2$) in the YSZ layer after spraying. However, in this study, XRD analysis confirmed the presence of small amount of monoclinic phase in the TBC immediately after deposition (in the sprayed state), in addition to the presence of dominant non-transformable (stable) tetragonal ($t\text{-ZrO}_2$), convertible tetragonal (semi-stable) ($t'\text{-ZrO}_2$), and cubic

phases. Apparently, according to the spraying conditions in this study, all of the monoclinic phases in the YSZ powder cannot be removed. However, plasma spraying caused a significant reduction in the monoclonal phase in the primary powder.

Figure 8 depicts the SEM structure of duplex YSZ based-coating with map analysis of the elements. According to dot mapping of the elements, while Cr, Ni, and Al are mostly concentrated in the lower BC layer, Zr and Y are concentrated only in upper TC layer.

Figure 9 illustrates the SEM images of the structure of YSZ based-functionally graded coating as well as map analyses of elements. Dot mappings confirms that although Cr, Ni, and Al are mainly concentrated in lower BC layer, they are also present in the upper graded layers, hence a gradual change can be observed in Ni, Cr, and Al elements from the bond to top coats. In addition, a slight gradual distribution of Zr and Y from the top to the bond coats was observed. The results of SEM analysis revealed that microstructure, porosity, and chemical composition changed gradually through the functionally graded coating.

In order to carry out finite element analysis, a mesh sensitivity analysis was taken into account to determine the number of required elements in a model, thus ensuring that the analysis results were not affected by changing the mesh size. The mesh sensitivity is determined based on Figure 10 which shows the temperature change as a function of element size. Figure 11 shows the contour of the stress distribution S_{22} (in Pascal) for Gadolinium Zirconate-based TBC containing two-layer (duplex) thermal barrier, three-layer functionally graded thermal barrier, and five-layer functionally graded TBCs. According to Figure 11a, the maximum tensile stress and compressive stress in the duplex GZ-based TBC are about 19.42 MPa and 18.09 MPa, respectively. As observed in Figure 11b, the maximum tensile stress in the

GZ-based three-layer functionally graded TBC is reduced to 11.37 MPa. The gradual change in the thermal expansion coefficients of the FGM layers leads to better adhesion among the layers and lower stress concentration. As shown in Figure 11c, the maximum tensile stress in the GZ-based five-layer functionally graded TBC is 8.53 MPa, which is the least one compared to the maximum stress level in the two-layer thermal barrier and three-layer functionally graded TBCs. The simulation results of the stress distribution in the duplex and functionally graded GZ based TBC were in good agreement with those reported in the literature [18,29,30]. In the functionally graded TBC, the less

difference between thermal expansions of layers would improve the adhesive bonding of ceramic/metal interface, thus avoiding later stress concentration and lessening the risk of crack initiation and propagation [11,33,34]. The maximum tensile stress in the three-layer functionally graded TBC was reduced by 41 %, compared to that of the two-layer TBC. In addition, the maximum tensile stress in the five-layer functionally graded TBC was reduced by 25 %, compared to that of the three-layer functionally graded TBC. This shows the effect of using functionally graded TBCs on both residual stress reduction and coating lifetime extension.

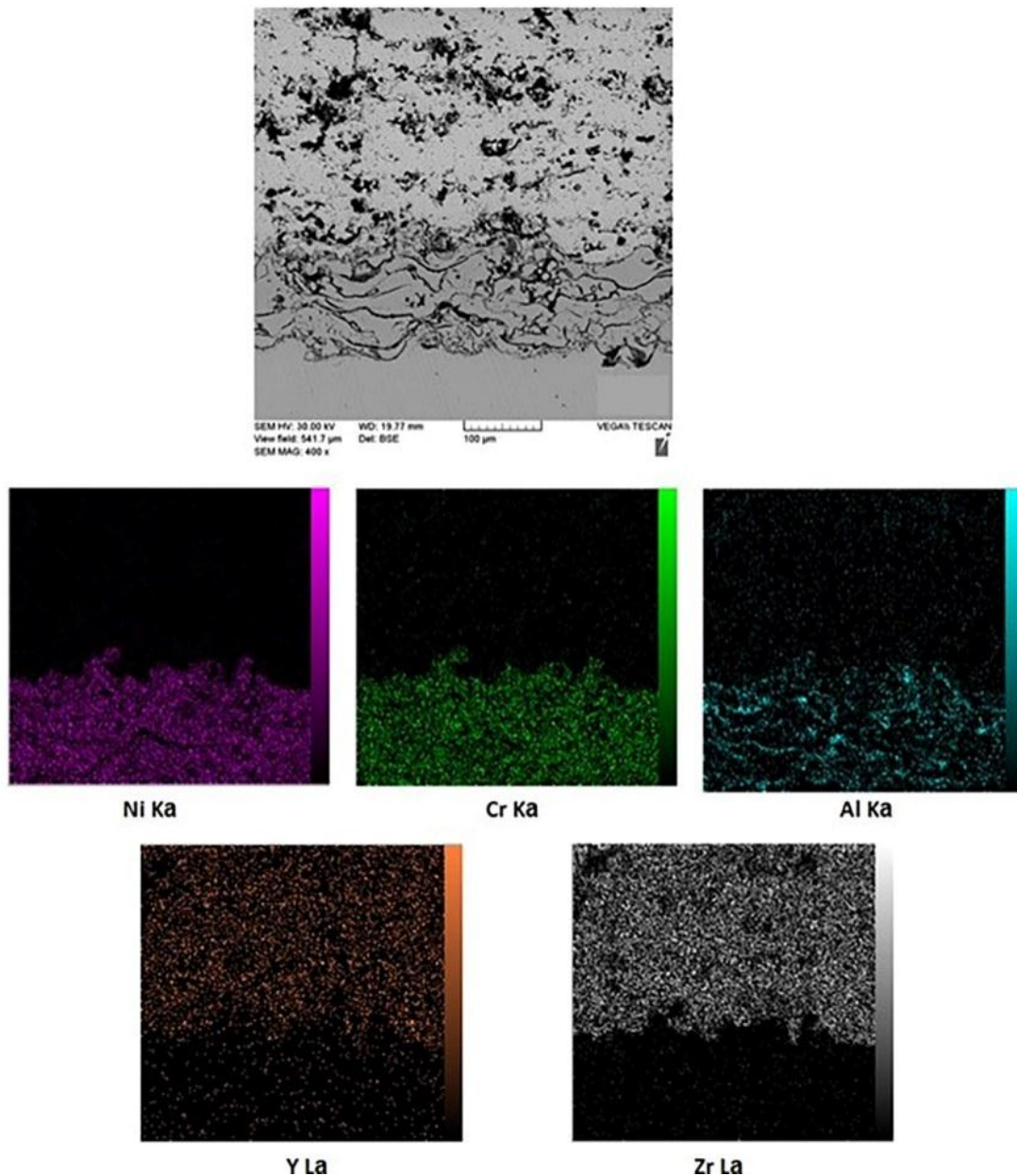


Figure 8. SEM image of the structure of YSZ/NiCrAlY coating with map analyses of elements

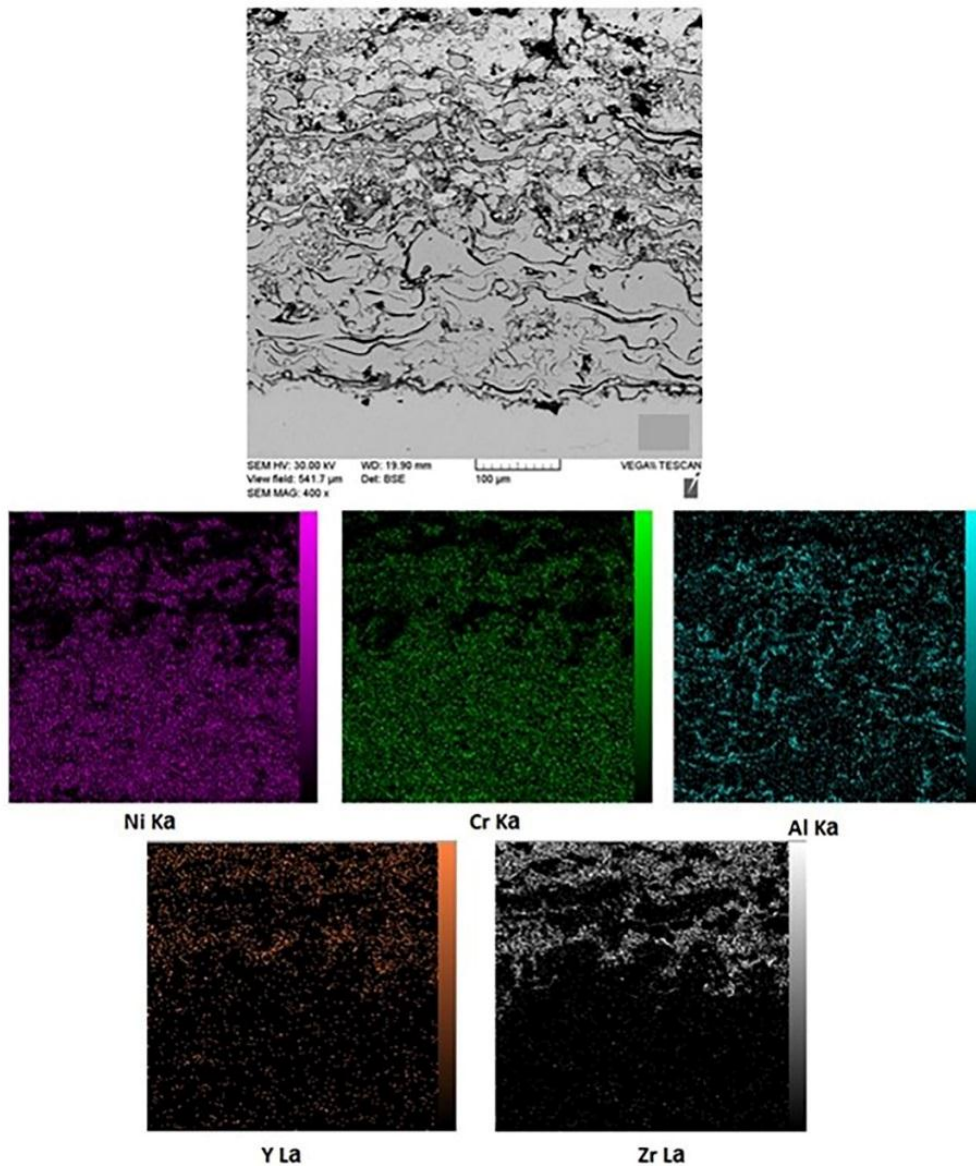


Figure 9. SEM image of the structure of Yttria stabilized Zirconia based functionally graded coating with map analyses of elements

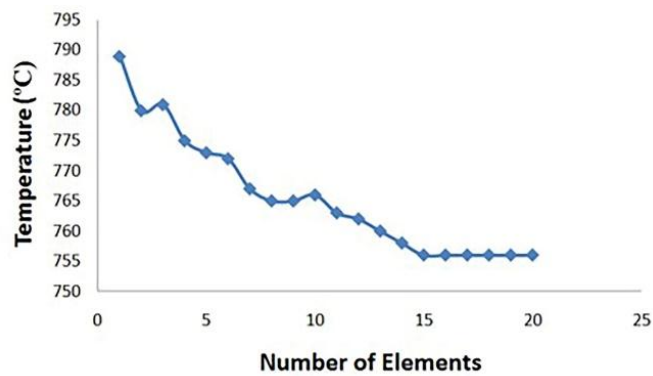


Figure 10. Mesh sensitivity analysis for TBC coating analysis

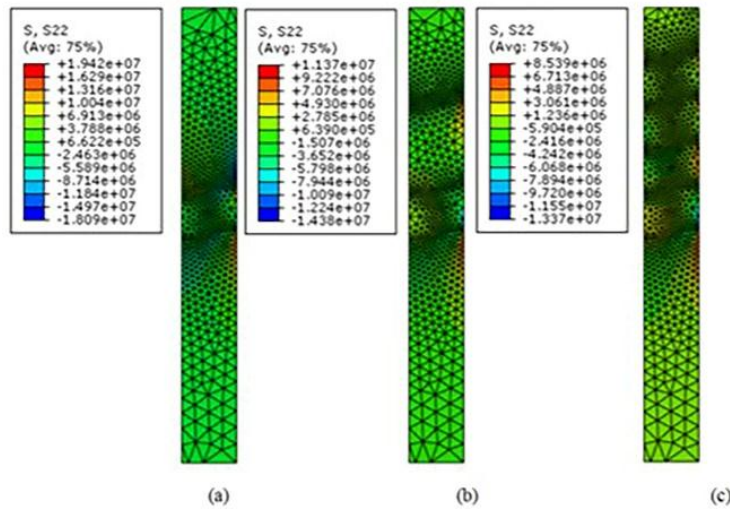


Figure 11. Stress distribution contours S22 (in Pascal) in Gadolinium Zirconate based thermal barrier coating a) duplex, b) three-layer FG-TBC, and c) five-layer FG-TBC

Figure 12 shows the contour of the stress distribution S22 (in Pascal) for Ytria stabilized Zirconia-based TBC: duplex (YSZ/NiCrAlY), a three-layer FG-TBC (YSZ/ 50 %YSZ + 50 %NiCrAlY/NiCrAlY) and a five-layer FG-TBC (YSZ/ 75 %YSZ + 25 %NiCrAlY/ 50 %YSZ + 50 %NiCrAlY/ 25 %YSZ + 75 %NiCrAlY/ NiCrAlY). Given that the thermal expansion of the BC is greater than that of the ceramic layer, compressive strength is observed in peak regions and tensile strength in valleys. In addition, a slow transition can be observed while approaching from the peak to the valley. The simulation results revealed that after the thermal shock, the average values of the maximum stress are 29 MPa for the duplex TBC (interface of TC / bond coat), 3.15 MPa for the three-layer FG-TBC system (interface of 50 % NiCrAlY - 50 %YSZ / YSZ), and 1.8 MPa for the five-layer FG-TBC system (interface of 25 % NiCrAlY- 75 % YSZ / YSZ). Of note, the stress distribution in the five-layer FG-TBC system is uniform which affects the performance and longevity of the thermal barrier system. The reason for this phenomenon is that the coefficient of the thermal expansion changed gradually throughout the five-layer functionally graded coating.

A comparison of Figures 11 and 12 confirms the higher amount of the residual stress in the Gadolinium zirconate-based TBC than that in the Ytria zirconate-based TBC. In Table 3, $\alpha_{GZ} < \alpha_{YSZ} < \alpha_{NiCrAlY}$; therefore, the difference in the thermal expansion coefficients of GZ and NiCrAlY is greater than that of YSZ and NiCrAlY, thus resulting in higher stress concentration.

As observed in Figure 13, the temperature distribution contours for the Gadolinium Zirconate-based TBC are shown in the following forms: two-layer (duplex) TBC, three-layer FG-TBC, and five-layer FG-TBC. The temperature difference between the TC surface and

substrate in a three-layer TBC is 35 °C which is lower than that of two-layer (duplex) TBC, i.e., 62 °C. The three-layer functionally graded TBC has a 43 % lower insulating value than that of the two-layer TBC, and the five-layer functionally graded TBC has a 17 % lower insulating value than that of the three-layer functionally graded TBC mainly because the thickness of the TC of FG-TBCs is less than that of duplex TBCs. To provide thermal insulation, the layers near the surface (high temperature side) of FG-TBC should be ceramic rich. The composition gradually changes along the TBC thickness, from the ceramic-rich near the surface to the metal-rich near the coating-metallic substrate interface. The layers near the interface are metal-rich, thus having higher fracture toughness [33,34].

Figure 14 shows the temperature distribution contours of the two-layer, three-layer, and five-layer functionally graded Ytria stabilized Zirconia-based TBCs. The simulation results revealed that the temperature dropped by 102 °C along the duplex TBC. Thermal insulation was found to be reduced by 30 % in the functionally graded YSZ/NiCrAlY coatings, compared to duplex coatings. It was previously reported that the insulation value of FG-TBCs was lower than that of conventional duplex YSZ TBCs with the same total coating thickness and YSZ porosity. The five-layer FG-TBC performs even worse than its three-layer counterpart due to a thinner YSZ top layer [35]. As observed in Figure 14, heat is primarily concentrated in the upper section of the coating system, and the substrate is protected from thermal damages. In other words, heat transfer is limited to the heat resistive ceramic parts while the BC and substrate experience lower temperatures, thus allowing for higher working temperatures. TBC protects the substrate from thermal load and keeps it at relatively lower

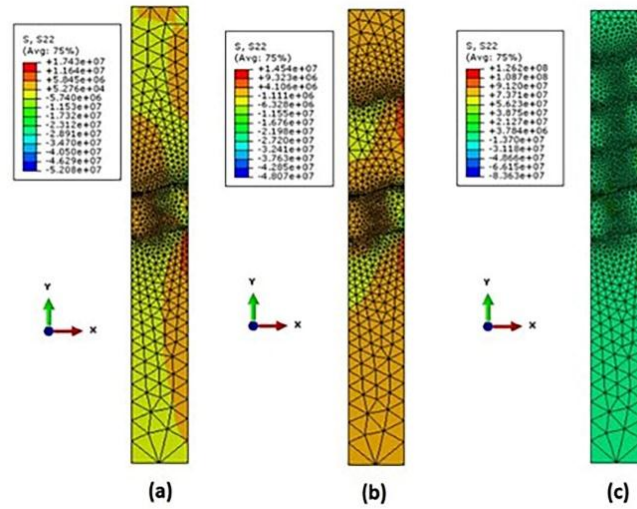


Figure 12. Stress distribution contours S_{22} (in Pascal) in Yttria Zirconate base thermal barrier coating a) duplex, b) three-layer FG-TBC, and c) five-layer FG-TBC

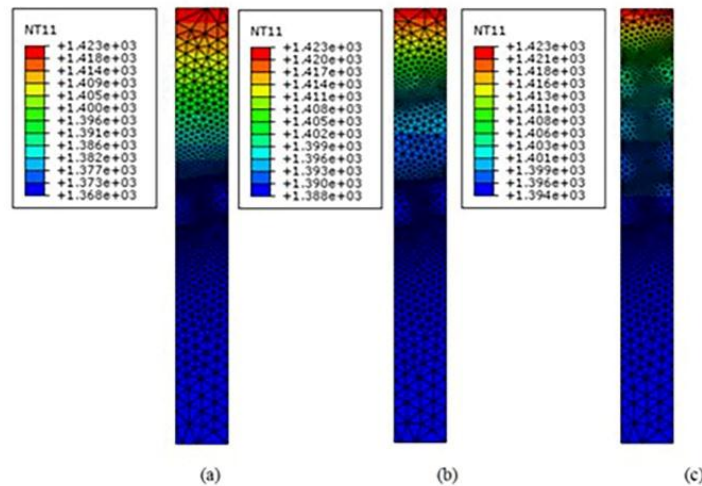


Figure 13. Temperature distribution contours in Gadolinium Zirconate based: a) two layer thermal barrier coating, b) three-layer functionally graded thermal barrier coating, and c) five-layer functionally graded thermal barrier coating

temperatures, thus resulting in an improved fatigue life, increased lifetime, and lower maintenance costs.

A comparison of Figures 13 and 14 revealed that the YSZ system exhibited better thermal insulation ability than GZ system. In addition, GZ had lower thermal conductivity (1.3 W/mK^{-1} at $1100 \text{ }^\circ\text{C}$) than that of YSZ (1.8 W/mK^{-1} at $1100 \text{ }^\circ\text{C}$). Consequently, it can be anticipated that GZ can provide better thermal insulation to the metallic substrate than YSZ. However, temperature reduction in the GZ system was even lower than that in the YSZ system. At $1500 \text{ }^\circ\text{C}$, the YSZ system outperformed the GZ system approximately 39%. According to the reports, the YSZ layer is characterized by more porosity than the GZ layer. YSZ also contains higher porosity content than that of GZ that can be

justified by the lower melting temperature of GZ ($2570 \text{ }^\circ\text{C}$) than that of YSZ ($2700 \text{ }^\circ\text{C}$). Therefore, the GZ splats undergo a greater degree of melting temperature than that of YSZ, thus resulting in a relatively denser coating for GZ than that for YSZ. The dependence of the porosity of heat conductivity of coatings was taken into account to explain the lower thermal reduction of Gadolinium Zirconate-base TBC than that of the YSZ system [36,37].

Through an indentation fracture mechanics approach, the micro hardness, fracture toughness, and residual stress of the multiple-shocked TBC were evaluated. Figure 15 illustrates the load-displacement curve for the maximum force of $9000 \text{ } \mu\text{N}$.

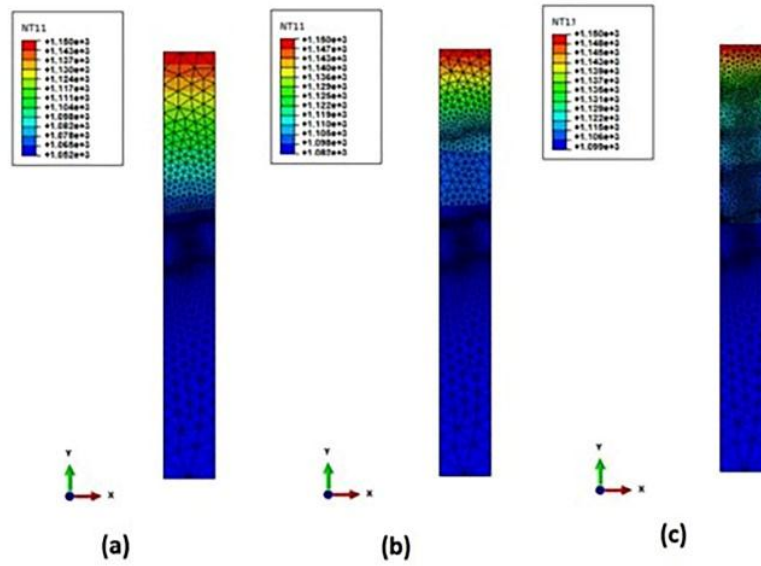


Figure 14. Temperature distribution contours in Yttria stabilized Zirconia based a) two layer thermal barrier coating, b) three-layer functionally graded thermal barrier coating, and c) five-layer functionally graded thermal barrier coating

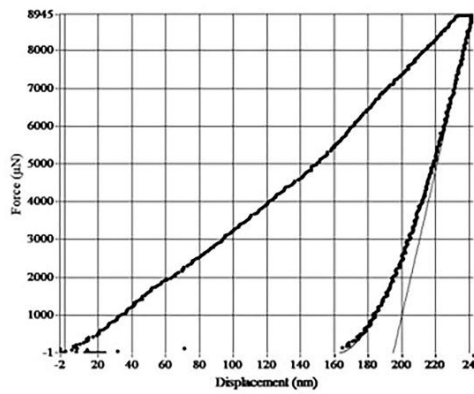


Figure 15. Load–displacement curve of the stressed three-layer YSZ-based FG-TBC under the maximum load of 9000 μN in the direction perpendicular to the cross-sectional area of the top coat

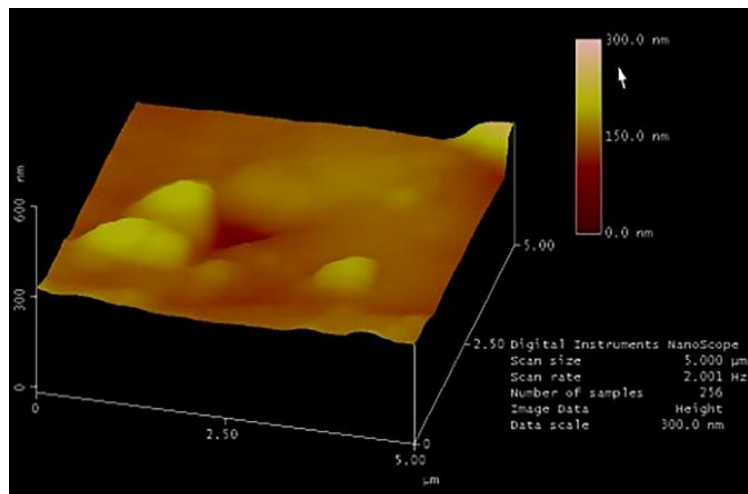


Figure 16. AFM images of impression by Berkovich indenter on the cross-section of the top coat layer of the stressed 3-layer YSZ-based FG-TBC under the maximum load of 8000 μN

Figure 16 depicts the AFM images of a Berkovich indenter impression on a stressed FG-TBC under the maximum load of 8000 N.

The relationship between the load and displacement from the initial unloading was used to calculate the Young's modulus, as shown in Equations (1)-(3). The values of the calculated hardness and Young's modulus in the TC are reported in Table 4. The size of the radial cracks was determined using image processing software.

Two parameters P/C^2 and $C^{0.5}$ were then calculated using the mean length of radial cracks. The results are reported in Table 5 according to which, the diagram of $P/C^{1.5}$ was plotted in terms of $C^{0.5}$ (Figure 17). As mentioned earlier in Figure 17, $(-\frac{2\sigma}{\sqrt{\pi}\chi_i})$ and $(\frac{K_{Ic}}{\chi_i})$ denote the slope and intercept of Equation (6), respectively. The calculation results of the χ_i , K_{Ic} , and residual stress are reported in Table 6, Table 7, and Table 8, respectively.

TABLE 4. Hardness and Young's modulus values for the top coat of stressed 3-layer YSZ- based FG-TBC

P	E_r	E_i	ν_i	Y	E	H
5000	178.6	1141	0.07	0.25	195.35	12.65
6000	185.8	1141	0.07	0.25	204.6	13.93
7000	211.6	1141	0.07	0.25	238.8	18.38
7500	190.5	1141	0.07	0.25	210.71	15.85
8000	111.5	1141	0.07	0.25	114.77	10.48
9000	211.7	1141	0.07	0.25	238.93	15.22

TABLE 5. The results of the calculation of the $P/C^{1.5}$ and $C^{0.5}$ and the mean length of the radial cracks

P(μ N)	$C_1(\mu$ m)	$C_2(\mu$ m)	$C_3(\mu$ m)	$C_{avg}(\mu$ m)	$C_{avg}(m)$	$P/C^{1.5}(N/m^{1.5})*10^6$	$C^{0.5}(m^{0.5})$
5000	0.33	0.33	0.29	0.32	3.16E-07	28.15	0.00056
6000	0.38	0.38	0.42	0.39	3.93E-07	24.35	0.00063
7000	0.46	0.44	0.43	0.44	4.43E-07	23.74	0.00067
7500	0.54	0.53	0.55	0.54	5.40E-07	18.90	0.00073
8000	0.55	0.55	0.63	0.58	5.76E-07	18.30	0.00075
9000	0.54	0.58	0.62	0.58	5.80E-07	20.38	0.00076

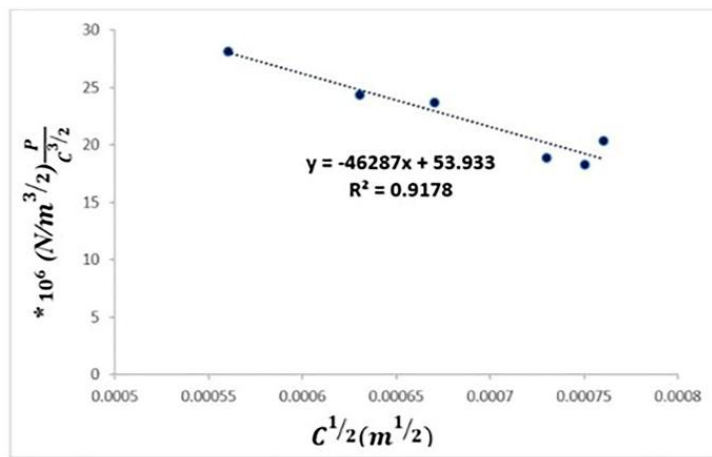


Figure 17. Relationships of $P/C^{1.5}$ versus $C^{0.5}$ when indented on the top coating surface

TABLE 6. Results of the calculation of the χ_i

α	$E_{avg}(GPa)$	$H_{avg}(GPa)$	E/H	χ_i
0.016	200.53	14.42	13.91	0.059

TABLE 7. Results of the calculation of the residual stress of stressed 3-layer YSZ- based FG-TBC

Slope	$\sigma (Pa)$	$\sigma (MPa)$
46287	100861-	0.100861-

TABLE 8. Results of the calculation of the fracture toughness of the stressed three-layer YSZ- based FG-TBC

α	E_{avg} (GPa)	H_{avg} (GPa)	E/H	X	Intercept	K_{Ic} (MPa.m ^{1/2})
0.016	200.53	14.42	13.91	0.059	53.933	3.18

As validation or model evaluation, the stresses obtained from the nanoindentation method and simulation are presented in Table 9. The presented simulation is acceptable based on the low difference in the obtained results. The results from the stress measurement through nanoindentation method indicated that the designed method could measure the stress along the coating depth without damaging the sample.

TABLE 9. Comparison of the nanoindentation and simulation results of the stressed three-layer YSZ- based FG-TBC

Error percent	σ_{xx} (Simulation) (MPa)	σ_{xx} (Nanoindentation) (MPa)
2.84	-0.098	-0.100861

4. CONCLUSION

The current study aimed to investigate the thermal and residual stress distribution in the duplex and functionally graded Thermal Barrier Coatings (TBCs) of yttria-stabilized zirconia (YSZ) and gadolinium zirconate (GZ) during a realistic heating regime that includes heating, operating time, and final cooling. For this purpose, a finite element model was employed to model the effects of thermal loading on the thermomechanical response and stress distribution. In addition, three different YSZ-based TBC systems, one duplex, and two FG -TBCs, were fabricated using the APS method. The residual stress, elastic modulus, microhardness, and fracture toughness of the coating were determined using the nanoindentation stress measurement method. The FGM strategy reduced the stress values in the coating more significantly than the conventional coating. Small differences in the thermal expansion would improve the adhesive bond between different ceramic/metal interfaces and reduce the risk of crack initiation and propagation. According to the findings, the level of residual stress in the functionally graded TBC was lower than that in the duplex TBC, and the stress distribution was more uniform, hence performance improvement and longevity expansion of the thermal barrier system. The results also indicated that most of the damage and heat fluxes were concentrated and accumulates in the ceramic face layers, hence less damage and shortened substrate life. Examination of the surface of the specimens after the application of thermal shock revealed that the separation

of the layers occurred more frequently in the two-layer TBCs than in the graded coatings. The results of stress measurement through the nanoindentation method showed that the developed stress measurement method could measure stress along the coating depth without damaging the specimen. It was also found that the TBC based on yttria-stabilized zirconia was slightly better than the that based on GZ in terms of thermal shock resistance and residual stress.

ACKNOWLEDGEMENTS

The authors would like to appreciate Iran University of Science and Technology and Standard Research Institute for their support.

REFERENCES

- Liu, B., Liu, Y., Zhu, C., Xiang, H., Chen, H., Sun, L., Gao, Y., Zhou, Y., "Advances on strategies for searching for next generation thermal barrier coating materials", *Journal of Materials Science & Technology*, Vol. 35, No. 5, (2019), 833-851. <https://doi.org/10.1016/j.jmst.2018.11.016>
- Fathi Dehkharghani, A. M., Rahimpour, M. R., Zakeri, M., "Crystal Structure and Lattice Parameter Investigation of La₃₊ Substituted CeO₂ in La_xCe_{1-x}O_{2.5/2} Synthesized by Solid-State Method", *Advanced Ceramics Progress*, Vol. 6, No. 1, (2020), 43-48. <https://doi.org/10.30501/acp.2020.106445>
- Clarke, D. R., Phillpot, S. R., "Thermal Barrier Coating Materials", *Materials Today*, Vol. 8, No. 6, (2005), 22-29. [https://doi.org/10.1016/S1369-7021\(05\)70934-2](https://doi.org/10.1016/S1369-7021(05)70934-2)
- Dean, J., Aldrich-Smith, G., Clyne, T. W., "Use of Nanoindentation to Measure Residual Stresses in Surface Layers", *Acta Materialia*, Vol. 59, No. 7, (2011), 2749-2761. <https://doi.org/10.1016/j.actamat.2011.01.014>
- Doleker, K. M., Ozgurluk, Y., Ahlatci, H., Karaoglanli, A. C., "Evaluation of Oxidation and Thermal Cyclic Behavior of YSZ, Gd₂Zr₂O₇ and YSZ/Gd₂Zr₂O₇ TBCs", *Surface and Coatings Technology*, Vol. 371, (2019), 262-275. <https://doi.org/10.1016/j.surfcoat.2018.11.055>
- Ge, W. A., Zhao, C. Y., Wang, B. X., "Thermal radiation and conduction in functionally graded thermal barrier coatings. part I: experimental study on radiative properties", *International Journal of Heat and Mass Transfer*, Vol. 134, (2019), 101-13. <https://doi.org/10.1016/j.ijheatmasstransfer.2019.01.018>
- Goswami, B., Ray, A. K., Sahay, S. K. "Thermal barrier coating system for gas turbine application-a review", *High Temperature Materials and Processes*, Vol. 23, No. 2, (2004), 73-92. <https://doi.org/10.1515/HTMP.2004.23.2.73>
- Karaoglanli, A. C., Altuncu, E., Ozdemir, I., Turk, A., Ustel, F., "Structure and durability evaluation of YSZ+Al₂O₃ composite TBCs with APS and HVOF bond coats under thermal cycling conditions", *Surface and Coatings Technology*, Vol. 205, (2011), S369-S373. <https://doi.org/10.1016/j.surfcoat.2011.04.081>

9. Kese, K., Rowcliffe, D. J., "Nanoindentation method for measuring residual stress in brittle materials", *Journal of the American Ceramic Society*, Vol. 86, No. 5, (2003), 811-816. <https://doi.org/10.1111/j.1151-2916.2003.tb03380.x>
10. Khoddami, A. M., Sabour, A., Hadavi, S. M. M., "Microstructure formation in thermally-sprayed duplex and functionally graded NiCrAlY/Yttria-Stabilized zirconia coatings", *Surface and Coatings Technology*, Vol. 201, No. 12, (2007), 6019-6024. <https://doi.org/10.1016/j.surfcoat.2006.11.020>
11. Kokini, K., DeJonge, J., Rangaraj, S., Beardsley, B., "Thermal shock of functionally graded thermal barrier coatings with similar thermal resistance", *Surface and Coatings Technology*, Vol. 154, No. 2-3, (2002), 223-231. [https://doi.org/10.1016/S0257-8972\(02\)00031-2](https://doi.org/10.1016/S0257-8972(02)00031-2)
12. Liu, B., Liu, Y., Zhu, C., Xiang, H., Chen, H., Sun, L., Gao, Y., Zhou, Y., "Advances on strategies for searching for next generation thermal barrier coating materials", *Journal of Materials Science & Technology*, Vol. 35, No. 5, (2019), 833-851. <https://doi.org/10.1016/j.jmst.2018.11.016>
13. Liu, Z. G., Ouyang, J. H., Zhou, Y., "Heat capacities and derived thermodynamic functions of neodymium-cadolinium zirconates from 298.15 to 1050 K", *Journal of Alloys and Compounds*, Vol. 475, No. 1-2, (2009), 21-24. <https://doi.org/10.1016/j.jallcom.2008.07.089>
14. Mahade, S., Curry, N., Björklund, S., Markocsan, N., Joshi, S., "Durability of gadolinium zirconate/YSZ double-layered thermal barrier coatings under different thermal cyclic test conditions", *Materials*, Vol. 12, No. 14, (2019), 2238. <https://doi.org/10.3390/ma12142238>
15. Nayeypashae, N., Seyedein, S. H., Aboutalebi, M. R., Sarpoolaky, H., Hadavi, M. M., "Modeling the effect of interface characteristics and layer compositional parameters on the residual stress distribution in FG-TBC system: FEM and FIS approach", *Journal of Ceramic Processing Research*, Vol. 17, No. 8, (2016), 803-814. <http://www.jcpr.or.kr/journal/archive/view/1933#>
16. Nayeypashae, N., Seyedein, S. H., Aboutalebi, M. R., Sarpoolaky, H., Hadavi, S. M. M., "Finite element simulation of residual stress and failure mechanism in plasma sprayed thermal barrier coatings using actual microstructure as the representative volume", *Surface and Coatings Technology*, Vol. 291 (2016), 103-114. <https://doi.org/10.1016/j.surfcoat.2016.02.028>
17. Nayeypashae, N., Aboutalebi, M. R., Seyedein, S. H., Sarpoolaky, H., Hadavi, M. M., "Simulation of the effect of sub-micron interface roughness on the stress distribution in functionally graded thermal barrier coatings (FG-TBC)", *Advanced Ceramics Progress*, Vol. 1, No. 1, (2015), 40-47. <https://doi.org/10.30501/acp.2015.69999>
18. Nayeypashae, N., Vafaenezhad, H., Hadavi, S. M. M., Seyedein, S. H., Aboutalebi, M. R., Sarpoolaky, H., "A study on the numerical simulation of thermo-mechanical behavior of the novel functionally graded thermal barrier coating under thermal shock", *ADMT Journal*, Vol. 8, No. 2, (2015), 29-36. http://admt.iaumajlesi.ac.ir/article_534924_6096e9df4f341acab0b97c321312d785.pdf
19. Olikier, V. E., Gridasova, T. Y., Pritulyak, A. A., "Effect of the porous structure of thermal-barrier coatings on their heat conductivity", *Powder Metallurgy and Metal Ceramics*, Vol. 47, No. 11, (2008), 717-722. <https://doi.org/10.1007/s11106-009-9066-2>
20. Ranjbar-Far, M., Absi, J., Mariaux, G., "Finite element modeling of the different failure mechanisms of a plasma sprayed thermal barrier coatings system", *Journal of Thermal Spray Technology*, Vol. 21, No. 6, (2012), 1234-1244. <https://doi.org/10.1007/s11666-012-9814-6>
21. Ranjbar-Far, M., Absi, J., Shahidi, S., Mariaux, G., "Impact of the non-homogenous temperature distribution and the coatings process modeling on the thermal barrier coatings system", *Materials & Design*, Vol. 32, No. 2, (2011), 728-735. <https://doi.org/10.1016/j.matdes.2010.07.034>
22. Song, J., Qi, H., Shi, D., Yang, X., Li, S., "Effect of non-uniform growth of TGO layer on cracking behaviors in thermal barrier coatings: A numerical study", *Surface and Coatings Technology*, Vol. 370, (2019), 113-124. <https://doi.org/10.1016/j.surfcoat.2019.04.069>
23. Mao, W. G., Wan, J., Dai, C. Y., Ding, J., Zhang, Y., Zhou, Y. C., Lu, C., "Evaluation of microhardness, fracture toughness and residual stress in a thermal barrier coating system: A modified vickers indentation technique", *Surface and Coatings Technology*, Vol. 206, No. 21, (2012), 4455-4461. <https://doi.org/10.1016/j.surfcoat.2012.02.060>
24. Thakare, J. G., Pandey, C., Mahapatra, M. M., Mulik, R. S., "Thermal barrier coatings—a state of the art review", *Metals and Materials International*, Vol. 27, No. 7, (2021), 1947-1968. <https://doi.org/10.1007/s12540-020-00705-w>
25. Vaßen, R., Jarligo, M. O., Steinke, T., Mack, D. E., Stöver, D., "Overview on advanced thermal barrier coatings", *Surface and Coatings Technology*, Vol. 205, No. 4, (2010), 938-942. <https://doi.org/10.1016/j.surfcoat.2010.08.151>
26. Yang, F., Li, J. C. M., *Micro and Nano Mechanical Testing of Materials and Devices*, New York: Springer, (2008). <https://doi.org/10.1007/978-0-387-78701-5>
27. Johari, A. D., Yunus, S. M., Husin, S., "Comparison on thermal resistance performance of YSZ and rare-earth GZ multilayer thermal barrier coating at 1250°C gas turbine combustor liner", *Journal of Advanced Research in Fluid Mechanics and Thermal Sciences*, Vol. 52, No. 2, (2018), 123-128. <https://www.akademiarbaru.com/submit/index.php/arfmts/article/download/2383/1344>
28. Zhang, P., Feng, Y., Li, Y., Pan, W., Zong, P. A., Huang, M., Han, Y., Yang, Z., Chen, H., Gong, Q., Wan, C., "Thermal and mechanical properties of ferroelastic RENbO₄ (RE = Nd, Sm, Gd, Dy, Er, Yb) for thermal barrier coatings", *Scripta Materialia*, Vol. 180 (2020), 51-56. <https://doi.org/10.1016/j.scriptamat.2020.01.026>
29. Lima, R. S., Marple, B. R., "Thermal spray coatings engineered from nanostructured ceramic agglomerated powders for structural, thermal barrier and biomedical applications: a review", *Journal of Thermal Spray Technology*, Vol. 16, No. 1, (2007), 40-63. <https://doi.org/10.1007/s11666-006-9010-7>
30. Ilavsky, J., Stalick, J. K., "Phase composition and its changes during annealing of plasma-sprayed YSZ", *Surface and Coatings Technology*, Vol. 127, No. 2-3 (2000), 120-129. [https://doi.org/10.1016/S0257-8972\(00\)00562-4](https://doi.org/10.1016/S0257-8972(00)00562-4)
31. Di Girolamo, G., Blasi, C., Pagnotta, L., Schioppa, M., "Phase evolution and thermophysical properties of plasma sprayed thick zirconia coatings after annealing", *Ceramics International*, Vol. 36, No. 8, (2010), 2273-2280. <https://doi.org/10.1016/j.ceramint.2010.07.035>
32. Osorio, J. D., Lopera-Valle, A., Toro, A., Hernández-Ortiz, J. P., "Phase transformations in air plasma-sprayed yttria-stabilized zirconia thermal barrier coatings", *Dyna*, Vol. 81, No. 185, (2014), 13-18. <https://doi.org/10.15446/dyna.v81n185.33409>
33. Zhao, X., Xiao, P., "Residual stresses in thermal barrier coatings measured by photoluminescence piezospectroscopy and indentation technique", *Surface and Coatings Technology*, Vol. 201, No. 3-4, (2006), 1124-1131. <https://doi.org/10.1016/j.surfcoat.2006.01.035>
34. Zhu, J., Xie, H., Hu, Z., Chen, P., Zhang, Q., "Cross-sectional residual stresses in thermal spray coatings measured by moiré interferometry and nanoindentation technique", *Journal of Thermal Spray Technology*, Vol. 21, No. 5, (2012), 810-817. <https://doi.org/10.1007/s11666-012-9732-7>
35. Zhu, L. N., Xu, B. S., Wang, H. D., Wang, C. B., "Measurement of residual stresses using nanoindentation method", *Critical Reviews in Solid State and Materials Sciences*, Vol. 40, No. 2 (2015), 77-89. <https://doi.org/10.1080/10408436.2014.940442>

36. Mahade, S., Curry, N., Björklund, S., Markocsan, N., Joshi, S., “Durability of gadolinium zirconate/YSZ double-layered thermal barrier coatings under different thermal cyclic test conditions”, *Materials*, Vol. 12, No. 14, (2019), 2238. <https://doi.org/10.3390/ma12142238>
37. Mahade, S., Curry, N., Jonnalagadda, K. P., Peng, R. L., Markocsan, N., Nylén, P., “Influence of YSZ layer thickness on the durability of gadolinium zirconate/YSZ double-layered thermal barrier coatings produced by suspension plasma spray”, *Surface and Coatings Technology*, Vol. 357, (2019), 456-465. <https://doi.org/10.1016/j.surfcoat.2018.10.046>



Materials and Energy Research Center

MERC

Contents lists available at [ACERP](#)

Advanced Ceramics Progress

Journal Homepage: www.acerp.ir

Advanced Ceramics Progress

Original Research Article

Microstructure and Mechanical Properties of Spark Plasma Sintered Amorphous AlPO₄ CeramicsF. S. Sayyedani ^{a,*}, M. H. Enayati ^b, M. R. Rahimpour ^c^a PhD, Department of Materials Engineering, Isfahan University of Technology (IUT), Isfahan, Isfahan, Iran^b Professor, Department of Materials Engineering, Isfahan University of Technology, Isfahan (IUT), Isfahan, Isfahan, Iran^c Professor, Department of Ceramics, Materials and Energy Research Center (MERC), Meshkindasht, Alborz, Iran* Corresponding Author Email: fs.sayyedani@alumni.iut.ac.ir (F. S. Sayyedani)URL: https://www.acerp.ir/article_145869.html

ARTICLE INFO

ABSTRACT

Article History:

Received 28 January 2022
Received in revised form 26 February 2022
Accepted 05 March 2022

Keywords:

Amorphous AlPO₄
Spark Plasma Sintering
Mechanical Properties
Fracture Toughness

The main objective of this study is to assess the structure and mechanical properties of amorphous aluminum phosphate (AlPO₄) ceramic specimens prepared through Spark Plasma Sintering (SPS) method. To this end, AlPO₄ powder was synthesized through sol-gel process and consolidated by SPS at the sintering temperature range of 800-1300 °C. Ceramic specimens were characterized by X-Ray Diffraction (XRD) and Scanning Electron Microscopy (SEM) analyses. Bulk density of the samples was measured using Archimedes' principle. In addition, hardness and indentation fracture toughness of the samples were determined to identify the mechanical properties. The results from XRD analysis, SEM images, and density measurement revealed that the sintered sample was characterized by an amorphous structure with the porosity of ~ 3 % and relative density of 97 % after SPS at 1000 °C for 15 min. Increasing the temperature to 1300 °C made the amorphous AlPO₄ crystallized. The fracture toughness was obtained to be 5.75 MPa.m^{1/2} under this sintering condition. Crack deflection around porosities was identified as the main toughening mechanism involved.

<https://doi.org/10.30501/ACP.2022.326779.1081>**1. INTRODUCTION**

High-Temperature Ceramic (HTC) materials mainly including high melting metal oxides, carbides, nitrides, and their composites are commonly used in a wide range of industrial applications such as metallurgy, cement, glass, aerospace, and energy [1]. HTCs are primarily applied owing to their thermal and thermo-mechanical properties. A number of studies have been and are still being conducted worldwide to find a novel class of HTCs characterized by preferential properties and develop the next generation of such materials. Some of their unique properties such as lightweight and low thermal

conductivity make them excellent candidates to be applied in aerospace industries that are also highly demanded, thus yielding many superior and promising results [2].

Aluminum phosphate (AlPO₄) is a well-known ceramic material for its high melting point (1800 °C), high hardness (~ 1000 HV), low density (2.1-2.6 g.cm⁻³), low electrical and thermal conductivities, and good corrosion and oxidation resistance at high-temperatures. This ceramic material can be widely used in the form of thin films, thick coatings, or bulk specimens in many applications, namely composites, catalysts, refractories, waterproof concrete, and phosphate-bonded ceramic

Please cite this article as: Sayyedani, F. S., Enayati, M. H., Rahimpour, M. R., "Microstructure and Mechanical Properties of Spark Plasma Sintered Amorphous AlPO₄ Ceramics", *Advanced Ceramics Progress*, Vol. 7, No. 4, (2021), 52-58. <https://doi.org/10.30501/ACP.2022.326779.1081>

2423-7485/© 2021 The Author(s). Published by MERC.

This is an open access article under the CC BY license (<https://creativecommons.org/licenses/by/4.0/>).

refractories, hence it can be regarded as one of the promising HTC materials [3].

Spark Plasma Sintering (SPS), also known as a rapid sintering method as well as a novel technique for synthesizing high-quality ceramic specimens, makes it feasible to maintain the intrinsic properties of powders in their fully dense products. Compared to conventional sintering methods such as Hot Pressing (HP) and Hot Isostatic Pressing (HIP), SPS process offers many advantages including easy operation, accurate control of sintering energy, high sintering speed followed by low grain growth, high reproducibility, safety, and reliability to name a few [4,5]. However, given the limitations of phase transformation, there are some restrictions in sintering the amorphous phases. Given that long sintering processes and high sintering temperatures may encourage crystallization, SPS process could be the right choice. Moreover, SPS makes it possible to obtain the maximum density at temperatures of at least 200 °C lower than those of HP or HIP [6]. For instance, Zhang et al. [7] fabricated transparent SiO₂ glass based on SPS at 900–1400 °C and reported the value of 98.5 % for the relative density of SiO₂ bodies at 1100 °C. They also employed Pressureless Sintering (PS) method to fabricate SiO₂ bodies for comparison and concluded that SPS was more effective than PS in terms of the depression of crystallization. SPS has also been used as a promising method to control the alumina microstructure by preventing the excessive grain growth during sintering due to the short holding times of only a few minutes. The main advantage of SPS was its ability to achieve densification without allowing excessive grain growth [8]. It can be used for sintering transparent ceramics, as discussed in a study by Apak et al. on the transparent polycrystalline alumina with optical properties identical to that of sapphire and Kanbur for transparent Aluminum OxyNitride (AlON) [9].

To the best of the authors' knowledge, no studies have been conducted on the fabrication of amorphous aluminum phosphate specimens using the SPS technique. In this regard, the present study primarily attempted to synthesize an amorphous AlPO₄ ceramic body based on SPS method and consider different process parameters to access desirable mechanical properties while preserving the initial amorphous structure.

2. MATERIALS AND METHODS

2.1. Amorphous AlPO₄ Powder Synthesis

Amorphous aluminum phosphate powder was synthesized through the sol-gel method, as explained in our previous report [10]. Table 1 gives the detailed characteristics of the precursors used to synthesize the starting powder. Aluminum nitrate nonahydrate and phosphorus pentoxide were separately dissolved in ethanol to achieve a clear solution with the molar ratio of

Al/P:1.75/1. These two solutions were mixed together under agitation condition for two hours and let age at ambient temperature for 24 h. The prepared gel was dried in an oven at 150 °C in air to complete the dehydration process and get a voluminous and fluffy gel. The dried gel was calcined in an electrical furnace (Nobertherm N7/H, Germany) in air at 500 °C for 30 min to strengthen the gel structure and obtain the final powder product.

TABLE 1. Precursors used for synthesizing amorphous AlPO₄ powder

Composition	Chemical formula	Company	Purity (%)
Aluminum Nitrate Nonahydrate	Al(NO ₃) ₃ .9H ₂ O	PENTA	98.5
Phosphorus Pentoxide	P ₂ O ₅	PENTA	99.5
Ethanol	C ₂ H ₅ OH	PENTA	99.9

2.2. Spark Plasma Sintering

The prepared powder was sintered using SPS apparatus (SPS-20T-10, Easy Fashion, China) in a vacuum atmosphere considering the parameters listed in Table 2. The powder was poured into a die with the inner diameter of 15 mm and covered with graphite paper. The heating and cooling rate of 100 °C.min⁻¹ and DC current pulse of 200/40:ms on/ms off were used for all samples. The graphite contaminations remaining from graphite foils on the sintered samples were eliminated using SiC sandpaper grinding wheel and polished using alumina slurry to 0.50 μm. In addition, X-Ray Diffractometer (XRD, Philips X'pert) was employed to carry out phase composition analysis of both starting powders and sintered specimens based on Cu Kα radiation (λ=1.54 Å, 40 kV, 30 mA) over the 2θ range of 10°–80°. Microstructural characterization was carried out on the polished surfaces of the sintered samples using Scanning Electron Microscopy (SEM, Philips XL30). The porosity of the specimens was assessed by ImageJ software.

TABLE 2. Parameters for sintering of amorphous AlPO₄ powder by SPS

Sample Number	Temperature (°C)	Holding Time (min)	Pressure (MPa)
1	800	30	50
2	900	20	50
3	1000	15	50
4	1300	10	50

2.3. Bulk and Relative Density Measurement

Bulk density (ρ_b, g.cm⁻³) was measured in distilled water based on the ASTM B962-17 standard test method using Archimedes' principle and Equation (1) [11]:

$$\rho_b = \frac{A \times \rho_w}{B - C} \quad (1)$$

where A is the mass of the test piece in air (g), ρ_w the density of water ($\text{g}\cdot\text{cm}^{-3}$), B the mass of the oil-impregnated test piece (g), and C the mass of the oil-impregnated test specimen in water with the mass of the specimen support tared (g). Finally, the relative density was measured using the ratio of the bulk density to the theoretical density.

2.4. Hardness and Fracture Toughness Evaluation

Hardness was also measured using a hardness testing machine (OTTO WOLPERT-WERKE GMBH, Germany) by Vickers indenter under a static load of 15 kg and at a dwell time of 10 s. The measurement was repeated five times to calculate the average value of the Vickers hardness (H_V) through Equation (2):

$$H_V = 1.85 \frac{f}{d^2} \quad (2)$$

where f is the load (kg), and d the average value of the two diagonals (mm).

Indentation fracture toughness was calculated from the length of the crack formed around the corners of indentations using the same hardness testing machine at a load of 20 kg. Fracture toughness (K_{IC} , $\text{MPa}\cdot\text{m}^{1/2}$) was then calculated using both Equation (3) and Figure 1 [12]:

$$K_{IC} = 0.203 H_V a^{1/2} \left(\frac{c}{a}\right)^{-3/2} \quad (3)$$

where H_V is the Vickers hardness (MPa), c the half length of the crack (m), and a the half length of the impression diagonal (m), as shown in Figure 1.

3. RESULTS AND DISCUSSION

The XRD patterns of aluminum phosphate powder calcined at 500 °C for 30 min accompanied with the spark plasma sintered specimens at different temperatures are illustrated in Figure 2. The results of the phase analysis of the powder confirmed the amorphous structure of AlPO_4 synthesized by the sol-gel process. The specimen sintered at 1000 °C for 15 min mainly preserved its

amorphous structure. Sintering at 1300 °C for 10 min clearly transformed the structure from amorphous to crystalline by appearance of Al_2O_3 and AlPO_4 peaks.

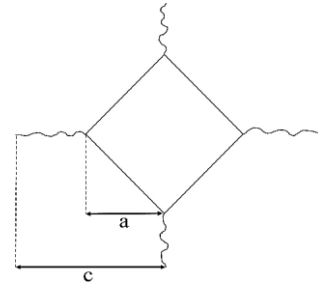


Figure 1. Schematic representation of crack generated by Vickers indenter

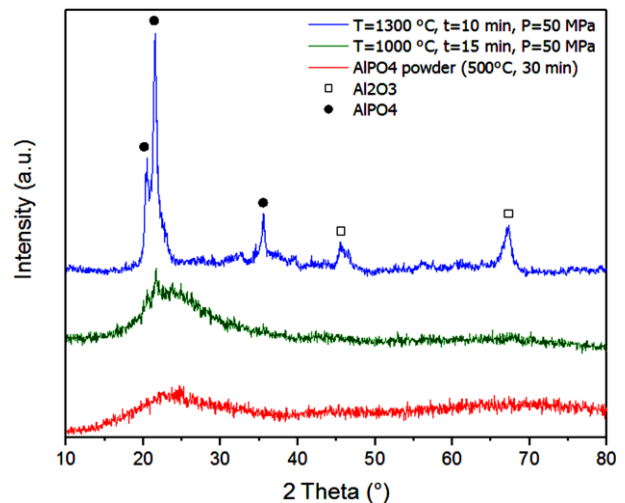


Figure 2. XRD patterns of AlPO_4 powder and spark plasma sintered specimens at different temperatures

Figure 3 depicts the SEM image and EDS analysis of AlPO_4 powder after annealing at 500 °C for 30 min. As observed in this figure, the average particle size of the powder used for the SPS process was less than 10 μm . Furthermore, the EDS analysis of AlPO_4 powder confirmed the presence of Al, P, and O elements in the powder structure.

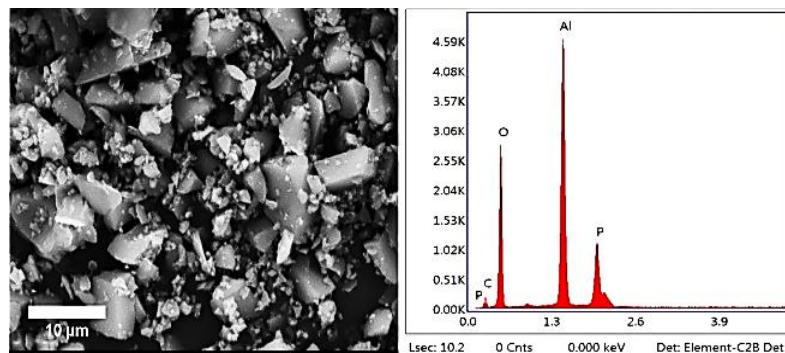


Figure 3. SEM image and EDS analysis of AlPO_4 powder after annealing at 500 °C for 30 min

Figure 4 shows the SEM images of the spark plasma sintered specimens processed under pressure of 50 MPa at different temperatures and different holding times. As shown in Figure 4a and Figure 4b, the temperatures of 800 °C and 900 °C were not sufficient to make dense AlPO_4 specimens. As a result, some irregular particles are observed in these images that are stuck together.

According to Figure 4c, the consolidation process was completed upon increasing the sintering temperature to 1000 °C. However, a fully dense and porosity-free specimen was not formed. As shown in Figure 4d, further increase in the temperature to 1300 °C did not help reduce porosities.

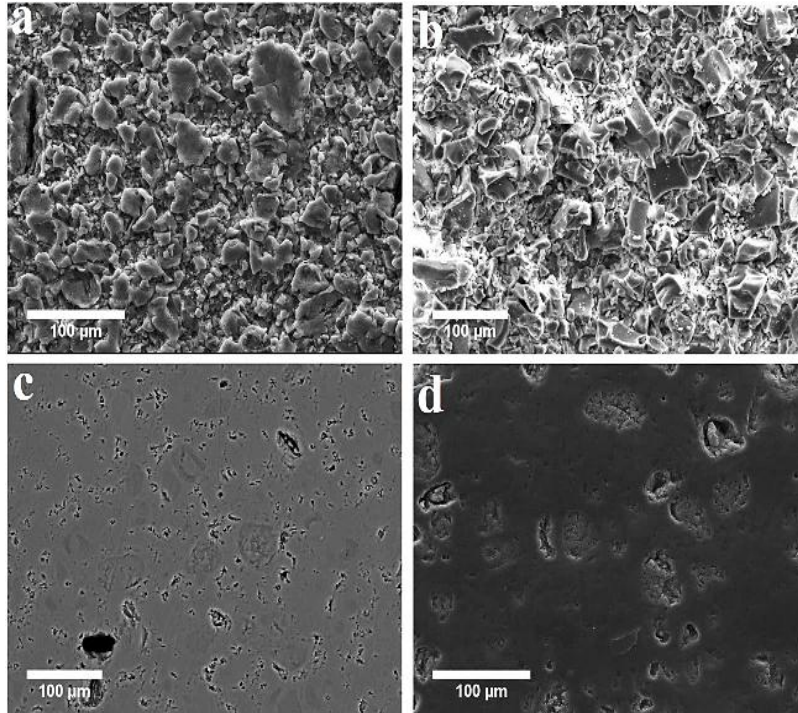


Figure 4. SEM images of spark plasma sintered specimens under pressure of 50 MPa at (a) 800 °C for 30 min, (b) 900 °C for 20 min, (c) 1000 °C for 15 min, and (d) 1300 °C for 10 min

Figure 5 presents the image analysis results using ImageJ software, and Table 3 shows the porosity values of 3 % and 1.5 % with the average porosity sizes of 3 μm and 2 μm for the samples sintered at 1000 °C for 15 min (Figures 5a and 5b) and 1300 °C for 10 min (Figures 5c and 5d), respectively. Table 3 also indicates that the values of the relative density of the samples sintered at 1000 °C for 15 min and 1300 °C for 10 min were 97 % and 98.5 %, respectively. Of note, a theoretical density of 2.2 $\text{g}\cdot\text{cm}^{-3}$ was used for calculating the relative density. While increasing the sintering temperature to 1300 °C produced a slightly more compact specimen than that produced at 1000 °C, the microstructure of the sintered sample at 1300 °C did not exhibit significant changes compared to the one sintered at 1000 °C (see Figure 5). However, the structure transition from amorphous to crystalline occurred at temperatures over 1000 °C according to the XRD patterns presented in Figure 2. In this respect, the sample sintered at 1000 °C for 15 min was selected for the next measurement mechanical properties.

Figure 6 presents the diagonal of the Vickers indentation for the sintered specimen at 1000 °C for 15 min under a load of 15 kg at the dwell time of 10 s. The value of the Vickers hardness (H_V) was calculated as 2104 MPa based on Equation (2).

Figure 7 shows the indentation crack propagation path in the specimen sintered at 1000 °C for 15 min. The fracture toughness of this sample was calculated as 5.75 $\text{MPa}\cdot\text{m}^{1/2}$ based on Equation (3) which can be a significant amount among the monolithic ceramic compacts. As observed in Figure 7b, the crack deflection around the micropores was the dominant toughening mechanism involved. Crack deflection accompanied with a significant stress relaxation at the tip of the crack near porosities suppressed the crack propagation and enhanced the fracture toughness [13]. The idea that lies behind all toughening mechanisms in monolithic ceramics is to increase the energy required for crack propagation [14]. Accordingly, four main toughening mechanisms were introduced: crack deflection [15], crack bridging [16], crack branching [17], and microcracking [18]. Porous ceramics exhibit several

advantages, in particular, lower thermal conductivity and strong thermal shock resistance, lighter weight, and

higher fracture toughness [19-21] than those of their dense counterparts.

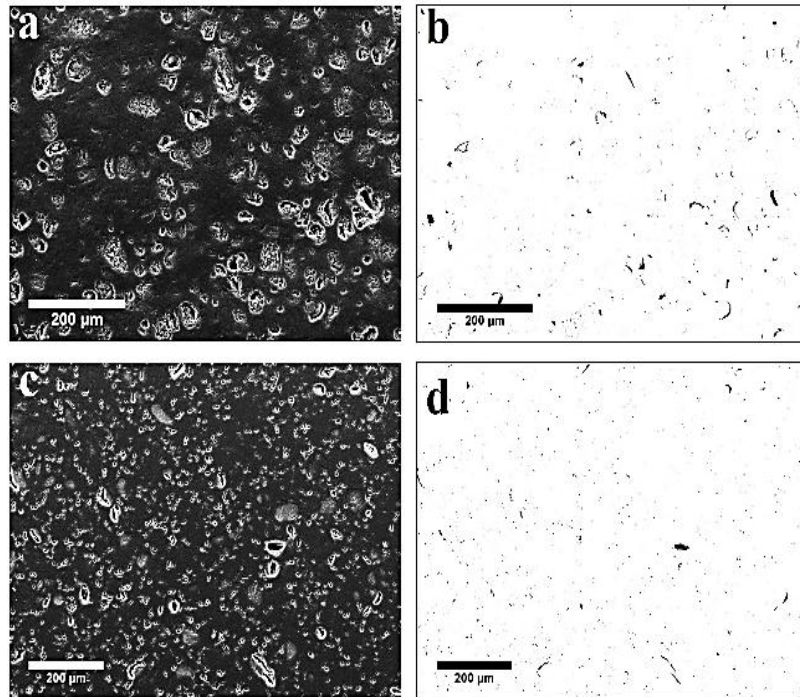


Figure 5. Porosity analysis by ImageJ software for SEM images of the spark plasma sintered specimens at the pressure of 50 MPa and (a,b) 1000 °C for 15 min and (c,d) 1300 °C for 10 min

TABLE 3. Porosity, bulk, and relative density of the sintered specimens based on the SPS process

Sample number	Porosity (%)	Porosity size (μm)	Bulk density (g.cm ⁻³)	Relative density (%)
3	3	15±3	2.1	97.0
4	1.5	12±2	2.2	98.5

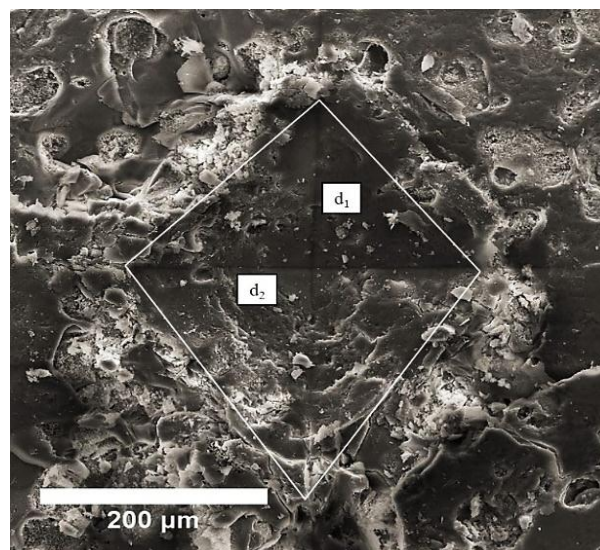


Figure 6. Vickers indentation at a load of 15 kg and a dwell time of 10 s

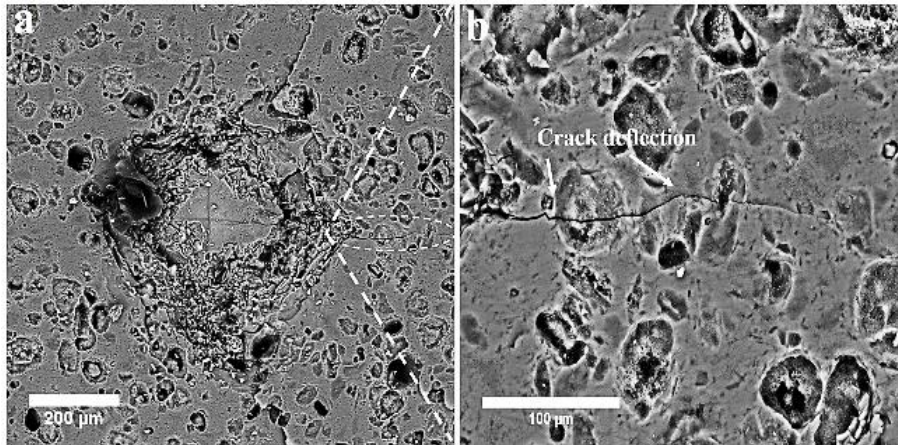


Figure 7. (a) Vickers indentation at a load of 20 kg and a dwell time of 10 s and (b) Crack propagation path demonstrating the toughening mechanism of crack deflection

Ghahremani et al. [22] evaluated the effects of the SPS parameters including the sintering temperature, applied pressure, and dwell time on the mechanical properties of the densified mullite specimens. They concluded that an increase in the applied pressure and dwell time would increase the density of the mullite. They reported the temperature of 1700 °C, dwell time of 15 min, and applied pressure of 20 MPa as the optimum parameters to obtain a relative density of 99 % and fracture toughness of 2.8 MPa.m^{1/2}. In addition, the maximum fracture toughness of 4 MPa.m^{1/2} was obtained while decreasing the relative density to 95.5 %. They declared that in fully-dense compacts, the crack was propagated in a straight-line path. On the contrary, in the case of porous compacts, the crack moved through a non-straight route due to the crack tip deflection at the pores which required more energy to propagate.

Lu et al. [23] fabricated porous Si₃N₄ ceramics by die pressing at 1800-1900 °C for four hours and subsequently, gel casting and gas-pressure sintering were performed to obtain high-porosity Si₃N₄ specimens. Their results showed that the sample with 37 % porosity was characterized by a higher fracture toughness value (3.53 MPa.m^{1/2}) than that with 32 % porosity (2.11 MPa.m^{1/2}). They attributed this behavior to the role of pores as the crack arresters and suggested a scenario to elaborate the toughening mechanism. They declared that followed by encountering a crack to a pore, the crack would be constrained to alter its path or stop at the pore. In this situation, the cracks propagated over a shorter distance, and they would be arrested by the pores, thus resulting in an increase in the crack resistance against growth in high porous ceramics.

Crack deflection and bridging could also occur around grain boundaries in polycrystalline materials and second-phase particles in composite specimens [13]. He et al. [24] studied the mechanical properties of nano-grain SiO₂ glass prepared through SPS process. A relative

density of above 90 % was obtained in the sintering temperature range of 1300–1550 °C. The SiO₂ specimen exhibited the highest hardness and fracture toughness of 14.2 GPa and 5.4 MPa.m^{1/2} at the optimum sintering temperature of 1450 °C, respectively. They concluded that the microstructure with nano-grain SiO₂ glass was responsible for crack deflection and high K_{IC} value. G. M. Asmelash et al. [25] evaluated the fracture toughness of Al₂O₃-SiO₂-ZrO₂ composite materials prepared by PS. The fracture toughness of the composite containing 75 wt. % Al₂O₃-10 wt. % SiO₂-15 wt. % ZrO₂ was reported to be 2.39 MPa.m^{1/2}. They realized that reinforcement particles (SiO₂+ZrO₂) in the alumina matrix played a key role in toughening, considering three toughening mechanisms namely crack deflection, crack bridging, and microcracks.

4. CONCLUSION

AlPO₄ ceramic specimens were fabricated through SPS process at the sintering temperature range of 800-1300 °C. In addition, the microstructure and mechanical properties including hardness and fracture toughness were characterized in this study. The obtained results revealed that the temperatures below 1000 °C were not sufficient to reach a dense specimen, while sintering at temperatures above 1000 °C clearly transformed the amorphous structure into the crystalline state. The sample sintered at 1000 °C for 15 min retained its initial amorphous structure with the relative density of 97 % and porosity of 3 %. The fracture toughness for this sample was 5.75 MPa.m^{1/2} which could be a considerable value compared to those reported for other monolithic ceramics. Microstructural examination of the cracked surface revealed that crack deflection around micropores was the main toughening mechanism involved.

ACKNOWLEDGEMENT

The authors acknowledge the support of Department of Materials Engineering, Isfahan University of Technology and Ceramics Department of Materials and Energy Research Center in this research.

REFERENCES

- Zhang, S., "High temperature ceramic materials", *Materials*, Vol. 14, No. 8, (2021), 2031. <https://doi.org/10.3390/ma14082031>
- He, J., Li, X., Su, D., Ji, H., Wang, X., "Ultra-low thermal conductivity and high strength of aerogels/fibrous ceramic composites", *Journal of the European Ceramic Society*, Vol. 36, No. 6, (2016), 1487-1493. <https://doi.org/10.1016/j.jeurceramsoc.2015.11.021>
- Sayyedani, F. S., Enayati, M. H., "On structure and oxidation behaviour of non-stoichiometric amorphous aluminium phosphate coating", *Surface Engineering*, Vol. 35, No. 8, (2019), 670-676. <https://doi.org/10.1080/02670844.2018.1560912>
- Anselmi-Tamburini, U., "Spark plasma sintering", *Encyclopedia of Materials: Technical Ceramics and Glasses*, Vol. 1, (2021), 294-310. <https://doi.org/10.1016/B978-0-12-803581-8.11730-8>
- Kermani, M., Razavi, M., Rahimpour, M. R., Zakeri, M., "The effect of temperature on the in situ synthesis-sintering and mechanical properties of MoSi₂ prepared by spark plasma sintering", *Journal of Alloys and Compounds*, Vol. 585, (2014), 229-233. <https://doi.org/10.1016/j.jallcom.2013.09.125>
- Hong, J., Gao, L., Torre, S. D. D. L., Miyamoto, H., Miyamoto, K., "Spark plasma sintering and mechanical properties of ZrO₂(Y₂O₃)-Al₂O₃ composites", *Materials Letters*, Vol. 43, No. 1-2, (2000), 27-31. [https://doi.org/10.1016/S0167-577X\(99\)00225-6](https://doi.org/10.1016/S0167-577X(99)00225-6)
- Zhang, J., Tu, R., Goto, T., "Fabrication of transparent SiO₂ glass by pressureless sintering and spark plasma sintering", *Ceramics International*, Vol. 38, No. 4, (2012), 2673-2678. <https://doi.org/10.1016/j.ceramint.2011.11.034>
- Mansoor, M., Mansoor, M., Mansoor, M., Er, Z., Çınar Şahin, F., "Ab-initio study of paramagnetic defects in Mn and Cr doped transparent polycrystalline Al₂O₃ ceramics", *Synthesis and Sintering*, Vol. 1, No. 3, (2021), 135-142. <https://doi.org/10.53063/synsint.2021.1340>
- Mansoor, M., Mansoor, M., Mansoor, M., Themelis, T., Çınar Şahin, F., "Sintered transparent polycrystalline ceramics: the next generation of fillers for clarity enhancement in corundum", *Synthesis and Sintering*, Vol. 1, No. 3, (2021), 183-188. <https://doi.org/10.53063/synsint.2021.1342>
- Sayyedani, F. S., Enayati, M. H., Hashempour, M., Vicenzo, A., Bestetti, M., "Synthesis and characterization of sol-gel derived non-stoichiometric aluminum phosphate coating", *Surface and Coatings Technology*, Vol. 351, (2018), 128-135. <https://doi.org/10.1016/j.surfcoat.2018.07.086>
- Bassett, K., Carriveau, R., Ting, D. S. K., "Underwater energy storage through application of Archimedes principle", *Journal of Energy Storage*, Vol. 8, (2016), 185-192. <https://doi.org/10.1016/j.est.2016.07.005>
- Tekeli, S., "Fracture toughness (K_{IC}), hardness, sintering and grain growth behaviour of 8YSZ/Al₂O₃ composites produced by colloidal processing", *Journal of Alloys and Compounds*, Vol. 391, No. 1-2, (2005), 217-224. <https://doi.org/10.1016/j.jallcom.2004.08.084>
- Launey, M. E., Ritchie, R. O., "On the fracture toughness of advanced materials", *Advanced Materials*, Vol. 21, No. 20, (2009), 2103-2110. <https://doi.org/10.1002/adma.200803322>
- Launey, M. E., Munch, E., Alsem, D. H., Barth, H. B., Saiz, E., Tomsia, A. P., Ritchie, R. O., "Designing highly toughened hybrid composites through nature-inspired hierarchical complexity", *Acta Materialia*, Vol. 57, No. 10, (2009), 2919-2932. <https://doi.org/10.1016/j.actamat.2009.03.003>
- Awaji, H., Ebisudani, M., Choi, S. M., Ohashi, T., "Crack Deflection Toughening mechanism in brittle materials", In *Fracture Resistance Testing of Monolithic and Composite Brittle Materials*, ASTM International, West Conshohocken, PA, USA, (2009), 137-151. <https://doi.org/10.1520/STP10476S>
- Erdogan, F., Joseph, P. F., "Toughening of ceramics through crack bridging by ductile particles", *Journal of the American Ceramic Society*, Vol. 72, No. 2, (1989), 262-270. <https://doi.org/10.1111/j.1151-2916.1989.tb06112.x>
- Bleyer, J., Roux-Langlois, C., Molinari, J. F., "Dynamic crack propagation with a variational phase-field model: limiting speed, crack branching and velocity-toughening mechanisms", *International Journal of Fracture*, Vol. 204, No. 1, (2017), 79-100. <https://doi.org/10.1007/s10704-016-0163-1>
- Ohji, T., Jeong, Y. K., Choa, Y. H., Niihara, K., "Strengthening and toughening mechanisms of ceramic nanocomposites", *Journal of the American Ceramic Society*, Vol. 81, No. 6, (1998), 1453-1460. <https://doi.org/10.1111/j.1151-2916.1998.tb02503.x>
- Chen, Y., Wang, N., Ola, O., Xia, Y., Zhu, Y., "Porous ceramics: Light in weight but heavy in energy and environment technologies", *Materials Science and Engineering: R: Reports*, Vol. 143, (2021), 100589. <https://doi.org/10.1016/j.mser.2020.100589>
- Li, Y., Wu, H., Liu, X., Huang, Z., "Microstructures and properties of porous liquid-phase-sintered SiC ceramic by hot press sintering", *Materials*, Vol. 12, No. 4, (2019), 639. <https://doi.org/10.3390/ma12040639>
- Jin, X., Dong, L., Xu, H., Liu, L., Li, N., Zhang, X., Han, J., "Effects of porosity and pore size on mechanical and thermal properties as well as thermal shock fracture resistance of porous ZrB₂-SiC ceramics", *Ceramics International*, Vol. 42, No. 7, (2016), 9051-9057. <https://doi.org/10.1016/j.ceramint.2016.02.164>
- Ghahremani, D., Ebadzadeh, T., Maghsodipour, A., "Spark plasma sintering of mullite: Relation between microstructure, properties and spark plasma sintering (SPS) parameters", *Ceramics International*, Vol. 41, No. 5, (2015), 6409-6416. <https://doi.org/10.1016/j.ceramint.2015.01.078>
- Lu, X., Wei, Y., Wang, H., Wen, J., Zhou, J., Fan, J., "Porosity and oxide layer dependence of thermal shock behavior of porous silicon nitride ceramics", *Journal of Materials Science & Technology*, Vol. 30, No. 12, (2014), 1217-1222. <https://doi.org/10.1016/j.jmst.2014.11.004>
- He, Z., Katsui, H., Goto, T., "Mechanical properties of nano-grain SiO₂ glass prepared by spark plasma sintering", *Journal of the European Ceramic Society*, Vol. 37, No. 2, (2017), 721-725. <https://doi.org/10.1016/j.jeurceramsoc.2016.09.020>
- Asmelash, G. M., Mamat, O., Ahmad, F., "Toughening mechanisms of Al₂O₃-SiO₂-ZrO₂ composite materials", *Ceramics-Silikáty*, Vol. 56, No. 4, (2012), 360-366. https://www.irsm.cas.cz/materialy/cs_content/2012/Asmelash_CS_2012_0000.pdf

AIMS AND SCOPE

Advanced Ceramics Progress (ACERP) as an ISC international journal is devoted to elucidating the fundamental aspects of chemistry and physics occurring at a wide range of oxide and nonoxide ceramics and composite materials and their processing, microstructure, properties, and applications. The journal provides a unique venue for publishing new exciting research, focusing on dynamic growth areas in this field.

INSTRUCTIONS FOR AUTHORS

Submission of manuscript represents that it has neither been published nor submitted for publication elsewhere and is result of research carried out by author(s).

Authors are required to include a list describing all the symbols and abbreviations in the manuscript. Use of the international system of measurement units is mandatory.

- On-line submission of manuscripts results in faster publication process and is recommended. Instructions are given in the ACERP web site: www.acerp.ir
- References should be numbered in brackets and appear in sequence through the text. List of references should be given at the end of the manuscript.
- Figures' captions are to be indicated under the illustrations. They should sufficiently explain the figures.
- Illustrations should appear in their appropriate places in the text.
- Tables and diagrams should be submitted in a form suitable for reproduction.
- Photographs and figures should be of high quality saved as jpg files (resolution > 600 dpi).
- Tables, illustrations, figures and diagrams will be normally printed in single column width (8 cm). Exceptionally large ones may be printed across two columns (17 cm).

PAGE CHARGES AND REPRINTS

ACERP subscribers do not need to make any payment for publication and reprints.

AUTHORS CHECKLIST

- Author(s), bio-data including academic degree, affiliation(s), ORCID(s), and e-mail addresses.
- Manuscript including title, abstract, key words, illustrations, tables with tables' captions, figures with figures' captions, acknowledgement, and list of references.
- MS Word files of the manuscript in the ACERP template and all figures (resolution > 600 dpi).
- Similarity check of the manuscript, copyright forms, and conflict of interest forms

Advanced Ceramics Progress,
P.O. Box 31787-316, Meshkin Dasht, Alborz, I. R. Iran
Materials and Energy Research Center, Imam Khomeini Blvd, Meshkin Dasht, Alborz, I. R. of Iran
P.O. Box 14155-4777, Tehran, I. R. Iran
No. 5, Ahuramazda St., Alvand Ave., Argentine Sq., Tehran, I. R. of Iran

Advanced Ceramics Progress

Volume 7, Number 4, Autumn 2021

CONTENTS

S. Ahmadi	Alkali-Activated Slag Cement and Concrete: A Review	1-9
S. Borhan M. R. Badr-Mohammadi S. Hesaraki J. Esmaeilzadeh	Fabrication and Preliminary Characterization of Tissue Engineering Scaffolds Based on Alumina/Bioactive Glass	10-19
V. Dalouji S. Goudarzi N. Rahimi A. R. Souri	Multi-Walled Carbon Nanotubes (MWCNTs) Synthesized on Ni-Cu NPs @ a-C: H Films: A Study of Cavity and Bearing Areas Percentage, ZX Topography, and the Width of the Surface Height Distribution with Different Ni Layers' Thickness	20-27
M. R. Akbarpour Arbatan F. S. Torknik	Modelling and Optimization of Densification and Hardness of Cu/SiC Nanocomposites based on Response Surface Methodology (RSM)	28-35
N. Nayebpashaei E. Etemadi B. Mohammad Sadeghi S. H. Seyedein	Experimental and Numerical Study of the Thermo-Mechanical Behavior of Plasma-Sprayed Gadolinium and Yttria Zirconate-Based Thermal Barrier Coatings	36-51
F. S. Sayyedani M. H. Enayati M. R. Rahimpour	Microstructure and Mechanical Properties of Spark Plasma Sintered Amorphous AlPO ₄ Ceramics	52-58



Journal Home Page: www.acerp.ir